AN ABSTRACT OF THE DISSERTATION OF

Jitraporn Phaksopa for the degree of Doctor of Philosophy in Civil Engineering presented on December 9, 2014.

Title: Wave-current Interaction Induced by Standing Long Waves in the Surf Zone

Abstract approved: _____

Merrick C. Haller

This dissertation has focused on the charateristics of bubbles generated by breaking waves and the feedback of wave-current interaction on the forcing mechanism of low frequency wave especially basin seiching wave. For the first study, Optical image capture observations of breaking waves in a laboratory surf zone are presented. The observations demonstrate episodic production of surface foam events as regular waves traverse the surf zone. The experimental conditions consist of regular waves in a freshwater flume and wave breaking is depth-induced over fixed, barred bathymetry. The optical image data are used to track the decay time of individual events. In addition, the frequency and spacing of discrete foam events are analyzed both in the time and wavenumber domains and the observations are compared to existing theory.

The second study examined the effects of wave-current interaction on the response and the generation of the basin standing waves in terms of water elevation and currents. We carried out coupled models between the incident waves and wave-induced currents. The incident waves and currents are coupled through the wave forcing effect (radiation stress gradient) and wave-current interaction terms. The wave fields are described by solving the wave action balance and wave number equations in terms of wavenumber, frequency, and energy with inclusion of energy dissipation due to break-

ing. We utilize the model over various beach slopes and primary wave conditions in order to discuss the responses and relationship between the responses, and primary wave field and beach slope. The results show that the basin standing wave interacts with the incident wave to produce negative feedback in terms of water elevation and current on the mild non-dimensional bed slope (β), otherwise it causes the positive feedback on the steep slope regime when wave-current interaction is considered. The cross-correlation function between the short wave and incoming basin seiching component of elevation is analyzed. The results confirm the distinctive phase relation of the short wave and incoming basin seiching between mild and steep slope regimes. Consequently, this phase shift links to an energy transfer mechanism between the short wave and the basin seiching responses. This effect also relates to the different basin standing wave mechanisms, whereas the negative response on the mild slope regime is conductive to long wave generation by bound wave releasing and the positive response on the steep slope regime leads to time-varying breakpoint forcing. These mechanisms agree well with the surf beat similarity parameter.

©Copyright by Jitraporn Phaksopa
December 9, 2014
All Rights Reserved

Wave-current Interaction Induced by Standing Long Waves in the Surf Zone

by
Jitraporn Phaksopa

A DISSERTATION

submitted to

Oregon State University

in partial fulfillment of
the requirements for the
degree of

Doctor of Philosophy

Presented December 9, 2014
Commencement June 2015

Doctor of Philosophy dissertation of Jitraporn Phaksopa presented on December 9, 2014

APPROVED:

Major Professor, representing Civil Engineering

Head of the School of Civil and Construction Engineering

Dean of the Graduate School

I understand that my dissertation will become part of the permanent collection of Oregon State University libraries. My signature below authorizes release of my dissertation to any reader upon request.

Jitraporn Phaksopa, Author

ACKNOWLEDGEMENTS

I would like to highly express my appreciations to my advisor, Dr. Merrick C. Haller for his support, encourangement and guidance throughout my graduate studies at Oregon State University. I would like to express my gratitude to Prof. Tuba Özkan-Haller for insightful comments and suggestions for my dissertation. I also appreciate the other committee members, Prof. Robert Holman, Prof. Harry Yeh, Prof. Daniel Cox and Dr. Wade Marcum.

I am thankful for The Royal Thai Government and Kasetsart University, who gave me the opportunity to study abroad and financial support. Also, I appreciate the International Student Advising and Services Scholarship (ISAS) for my financial support in Fall2004.

I would like to thank my office mates-Guillermo Diaz, Randall Pittman, David Honegger, my friends-Wenwen Li and Gabrieal Gracia for their great companionship. I would like to thank all my friends at Oregon State University for making my time in Corvallis joyful and memorable

Finally, I would like to give my special gratitude to my family for my life, their love and support. I am grateful for my dear Prapansak Srisapoome for your love, care, encouragement, and support during these years.

CONTRIBUTION OF AUTHORS

The manuscripts comprising Chapter Three this dissertation include Tuba Özkan-Haller as a co-author. Dr. Özkan-Haller 's contribution included advice on the design and writing of this manuscripts.

TABLE OF CONTENTS

Page

1. General Introduction 1

1.1 Bubbles 2

1.2 Low frequency waves 5

2. Analysis of Surface Foam Events Produced by Waves in a Laboratory Surf Zone 8

2.1 Methodology 12

2.1.1 Set up 12
2.1.1.1 Wave conditions 12
2.1.1.2 Video measurement and processing 13
2.1.2 Data Analysis 13
2.1.2.1 Galilean Transformation 15
2.1.2.2 Surface foam area 18
2.1.2.3 Surface foam length scales 20

2.2 Results and Discussion 24

2.2.1 Bubble Characteristics 24
2.2.2 Surface foam area 26
2.2.3 Surface foam length scales 35

2.3 Conclusions 42

3. Wave-current Interaction Induced by Standing Long Wavevs in the Surf Zone 44

3.1 Introduction 45

3.2 Methodology 50

3.2.1 Flow Equations 50
3.2.2 Wave Model 51
3.2.3 Model procedure and application 53

3.3 Results 56

3.3.1 Wave forced the low frequency wave motion 58
3.3.1.1 The response of low frequency basin seiching 58

TABLE OF CONTENTS (Continued)

Page

3.3.1.2 Mean Quantities 61
3.3.1.3 Frequency modulation amplitude and seiching mode profile 64
3.3.2 Breaking point excursion 65

3.4 Discussion 67

3.5 Conclusions 73

4. GENERAL CONCLUSIONS 75

5. BIBLIOGRAPHY 77

6. APPENDICES 87

A Analysis of surface foam area 88

B Analysis of surface foam length scales 94

C Wave energy equation 100

D Separation of longwaves over the horizontal bottom 103

LIST OF FIGURES

Figure Page

2.1 (top) vertical elevation of the fixed bed. Vertical dashed lines represent the domain for the intensity time stacks. Experimental conditions: (second panel) measured wave heights for six runs. (third panel) The intensity time stack from Runs 37. Waves start breaking around the location $x = 52m$ and continually breaking through the shore break. (forth) The intensity time stack from Runs 40. Wave were initially breaking around $x = 55\,m$ and stop breaking around bar through and breaking again at the shore break. 14

2.2 An example snapshot of the OSU-LWF during the experiment. (Top) It clearly shows bubble plume at the front face of the progressing wave. (Bottom) Top view of the experimental set up. It shows the wave gages locations. 16

2.3 Portion of time stack from Runs 37 (the pixel intensity:0-250). (left) the intensity time stack (middle) intensity time stack in new coordinate system (Galilean Transformation) (right) the binary mask time stack by using threshold $(\overline{I} + \sigma_I)$ 19

2.4 Example video data from Run 37 (top) timestack of the smoothed $I(x,t)$ with running average (2.5 m window) with the horizontal dash line indicating at $t = 249.5s$. (lower) Cross-shore variation of pixel intensity $I(x, t = 249.5s)$. Dashed line is the threshold value $(\overline{I} + \sigma_I)$.. 21

2.5 Example of video data from Runs 36 a) time stack $I(x,t)$ with the horizontal line indicating at time $t = 102.5, 103.5, 104.5, 105.5s$ b) pixel intensity times series for different times $I(x, t = 102.5, 103.5, 104.5, 105.5s)$ 27

2.6 An example portion of a processed time stack (Runs 37): (top) intensity time stack from $t = 100 - 150s$, (bottom) time variation of surface foam area (m^2) (D1 and d2) plot over the normalized mean intensity 28

2.7 Runs 37: Time series of area evolution of 5 individual waves (blue line and blue dots). At the beginning (wave crest) of each wave shows the maximum of area and then decay in time. The red lines are fitted exponential decay curves with diffrent decay times (τ). (Top) Area from domain $D1$ (Bottom) Area from domain $D2$ 30

LIST OF FIGURES (Continued)

Figure — Page

2.8 Runs 37: Time series of area evolution (blue dots) of 1 individual wave from two domains and fitted exponential decay curves wtih decay time (Top): $D1$ τ = 1.06 and (Bottom): $D2$ τ = 0.66. 31

2.9 Temporal evolution of surface foam area. (top) from domain ($D1$) (lower) from domain ($D2$). Different colors corrrespond to different ξ_b 32

2.10 Scatterplots of bubble decay time and wave characteristics. (top) Breaking wave height (H_b) (middle) wave slope (H_b/L_2) (bottom) Iribarren number (ξ_b) 33

2.11 A scatterplot of surface foam decay time and maximum surface foam has an offset of 1 s from wave crest from domain ($D1, D2$). We use the same symbols with figure 2.10 34

2.12 Comparison of τ from 3 different thresholds: $\overline{I} + 0.5\sigma_I$, $\overline{I} + \sigma_I$, and $\overline{I} + 1.5\sigma_I$, (left) domain $D1$ (right) domain $D2$ 35

2.13 Portion of data (Runs 37) from t =70-100 s: (top) The intensity timestack (middle) The time stack of the smoothed with running average (2.5 m window), zero-upcrossing of the threshold ($\overline{I} + \sigma_I$), and setting zero length scales around wave crest regions intensity (lower) Time variation of length scales (λ_2: lengthscale between 2 highest peaks) and (λ_{10}: mean length scales of 10 events overlay with the normalized the mean intensity 36

2.14 The relationship between the discrete length scales (λ_2, λ_{10}) and the calculated length scales (λ_{model}). The dashed black line is a 1:1 relationship. 37

2.15 Example of PSD time stack image from Run36 38

2.16 The variation of data from t = 95.0 – 110.0 s (a) time stack $I(x,t)$ (b) time series of spectral bandwidth (ν) (c) time series of spectral width (ϵ) 39

2.17 The spectral density and its mean wavenumber (k_{mean}) at time t = $102.5, 103.5, 104.5, and 105.5s$. k_{mean} is 17.39, 6.68, 7.43, 14.36, and 18.48 m^{-1}) 40

2.18 The variation of ν, λ_{mean}, k_{mean}, the vertical line represent the time when wave is breaking 41

LIST OF FIGURES (Continued)

Figure | Page

3.1 (top) Example of the first breaking point of each wave on time stack image of the intensity data from RUN37 and this breaking point represents basin seiching with period 56.1 s and (bottom) vertical elevation of the fixed bed in the experiment 49

3.2 The examples of modal profiles of η and u at the seiching frequency for two beach slopes. (Right) m = 1/10: for $case2D$ (Left) (Right) m = 1/10: $case2D$. (-, - -, and + represents while excluding wave-current, including wave-current interaction, and pure seiching respectively). In case of pure seiching, the magnitude of both parameters are multiplied by 10. 57

3.3 Time series for m=1/50 (Case1D) including wave-current interaction. Results for wave height(H), ω, and k at two locations related with breaking point at x=1.65 m (breaking point)-blue lines and 6.43 m (inner surf zone point)-red lines 60

3.4 Time series of η, and u at breaking point (x= 1.65 m-blue lines) and inner surfzone point (x = 6.45 m-red lines) for m=1/50 (Case1D) while neglecting(Left) and including (Right) wave-current interaction. 61

3.5 Time series for m=1/10 (Case2D) including wave-current interaction. Results for wave height(H), ω, and k at breaking point (x= 5.30 m-blue lines) and inner surfzone point (x = 7.30 m-red lines)..... 62

3.6 Time series of η, and u at breaking point (x= 5.30 m-blue lines) and inner surfzone point (x = 7.30 m-red lines) for m=1/10 (Case2D) while neglecting(Left) and including (Right) wave-current interaction. 63

3.7 The decay/growth rate of water surface elevation and current when when including wave-current interaction at the breaking point for all cases. The squared and x marks represent the water elevation and current, respectively. 63

3.8 Mean Quantities of momentum terms for $case1D$ (Left) and $case2D$ (Right). Mean pressure gradient, radiation stress gradient, and advection gradient neglecting (dashed lines) and including (solid lines) wave-current interaction. The vertical dashed lines represent the mean breaking point 64

LIST OF FIGURES (Continued)

Figure Page

3.9 The frequency modulation amplitude ($A*$) normalized by the mean frequency (ω_0) for **upper)** $case1D$ and **lower)** $case2D$ while including wave-current interaction 66

3.10 The normalized waveheight when wave-current is included. (Right) $case1D$: $x_b = 1.65$ m (Left) $case2D$ $x_b = 5.30$ m 66

3.11 RHS of wave energy equation (3.19) while excluding and including wave-current interaction for $case1D$ (left) and $case2D$(right) 69

3.12 Time evolution of work done excluding (blue lines) and including (black lines) wave-current interaction for $case1D$ (Left) and $case2D$ (Right) 70

3.13 Cross correlation between the short wave height and basin standing wave incoming elevation when including wave-current interaction at three locations for $case1D$ (Left) and $case2D$ (Right) 72

1.1 Define bubble area by using binary image for RUN35: D1 is surface foam area calculating from bar crest to bar trough (G3:G46), D2 is surface foam area starting from breaking point to shoreline (G3:G6).. 88

1.2 Define bubble area by using binary image for RUN40: D1 is surface foam area calculating from bar crest to bar trough (G3:G46), D2 is surface foam area starting from breaking point to shoreline (G2:G6).. 89

1.3 Define bubble area by using binary image for RUN36: D1 is surface foam area calculating from bar crest to bar trough (G3:G46), D2 is surface foam area starting from breaking point to shoreline (G2:G6).. 90

1.4 Define bubble area by using binary image for RUN37: D1 is surface foam area calculating from bar crest to bar trough (G3:G46), D2 is surface foam area starting from breaking point to shoreline (G2:G6).. 91

1.5 Define bubble area by using binary image for RUN38: D1 is surface foam area calculating from bar crest to bar trough (G3:G46), D2 is surface foam area starting from breaking point to shoreline (G2:G6).. 92

1.6 Define bubble area by using binary image for RUN33: D1 surface foam area calculating from bar crest to bar trough (G3:G46), D2 is surface foam area starting from breaking point to shoreline (G2:G6).. 93

2.1 Time variation of surface foam length scales RUN35 94

LIST OF FIGURES (Continued)

Figure		Page
2.2	Time variation of surface foam length scales RUN40	95
2.3	Time variation of surface foam length scales RUN36	96
2.4	Time variation of surface foam length scales RUN37	97
2.5	Time variation of surface foam length scales RUN38	98
2.6	Time variation of surface foam length scales RUN33	99

LIST OF TABLES

Table — Page

2.1 Wave conditions: no. of waves in the data record, wave period (T), deep water wave height (H_0), deep water steepness (H_0/L_0), Iribarren number** (ξ_b), and deep water wavelength (L_0) 15

2.2 Bubble decay time (τ_1, τ_2) from the intensity timestack from bubble area from domain $D1$, $D2$ 34

2.3 Bubble length scales from the experiment, prediction from Yeh and Mok (1990), change in energy flux at G3 ang G4, and change in energy flux at G3 ang G6. Unit of energy flux is $kg * m/s^3$ 37

2.4 Spectral parameter: ϵ, ν, k_{mean}, λ_{mean} 41

3.1 The experimental conditions for all cases: beach slope (m), wave period ($T(s)$), deep water wave height (H_0), deep water wavelength (L_0), deep water steepness ($\frac{H_0}{L_0}$), surf similarity (ξ), normalized bed slope (β), surfbeat similarity ($\xi_{surfbeat}$) 55

Wave-current Interaction Induced by Standing Long Waves in the Surf Zone

1. General Introduction

A coastal zone is dynamic because interaction between the ocean and land. This zone is significantly for human and marine wildlife.The coastal zone experiences short and long term scales of change both spatially and temporally. The coastal dynamic involves with various dominant coastal processes such as ocean current (longshore current, rip current, and undertow current), and waves. Therefore, the understanding of coastal processes can benefit for the planning, maintenance, and management of the coastal region.

Among the other coastal processes, waves are the most significant mechanism in the nearshore zone. Waves are the main forcing for the generation of nearshore current causing sediment suspension and transport. Especially, wave breaking produces turbulence, entrains air bubbles and also transfers a momentum flux into the water column. Waves shoal when traveling from deep to shallow water or toward shore, by adjusting shapes i.e. increasing wave height, decreasing wavelength and speed. As waves become unstable and break, then that energy is dissipated during the wave breaking process. Wave breaking is the principal driving mechanism for nearshore currents, mean water level changes, low frequency oscillatory motions within the surf zone, sediment transport, and exchanging mass, momentum and energy between the ocean and the atmosphere. Wave breaking is variable in both time and spatial scale. Hence, the prediction of breaking is poorly quantified. The knowledge, information, and numerical model involved with breaking wave is important to coastal engineering,

social science, and scientific community for several reasons in terms of planning and maintenance of coastal infrastructures, and protecting coastal zone.

1.1 Bubbles

After wave breaking, bubbles are generated when air is entrained into the water column by the overturning crest of a breaking wave. Some bubbles tend to rise on the surface and form the whitecap, and some bubbles are dispersed into the water column by turbulence. The evolution of bubble can be divided into two phases: acoustically active phase and quiescent plume. The first phase, bubbles are entrained, fragmented inside the breaking wave crest. These bubbles are accomapnied by a burst of noise. This phase lasts for a second or so. After that, bubbles are into the second phase involving many processes including turbulent diffusion, advection, dissolution and degrassing.

The size of bubbles varies from a few microns to a centimeter. The bubble can powerfully scatter light and sound in water because their refractive index is considerably less than that of the surrounding medium and their size is typically large compared to wavelengths of light. Stramski (1994) showed that the significance of bubbles for the scattering of light in the ocean.

Though the short lifetime, bubbles or whitecap are significant in air-sea interaction. For example, bubble patches cause energy dissipation [Iafrati (2011); Lamarre and Melville (1991)]; produce sea spray and aerosols [Cipriano and Blanchard (1981); Andreas and Monahan (2000)] which contribute to heat exchange and intensification of tropical cyclones (Andreas et al., 2008), change sound speed and ocean ambient noise [Pumphrey and Ffowcs Williams (1990); Farmer et al. (2001)] influence on the

optical properties of water (Koepke, 1986) that enhanced the significant error in ocean remote sensing data (Zhang et al., 1998), and salinity data from active and/or passive microwave measurement (Camps et al., 2005).

The study of bubbles in the vicinity of the wave crest during breaking is a challenging work because bubbles rapidly change in spatial and temporal scales. However, the bubble charateristics have been studied in the fields, laboratory measurements, and numerical models by using several techniques such as optical, photographic, and acoustic. For example, Deane and Stokes (1999) created a new optical instrument to capture the air entrainment process in breaking waves and measure bubble size distribution in the laboratory experiment. The digital images of sea surface were used to determine the whitecap decay time from the field observation (Callaghan et al., 2012) and laboratory experiment (Callaghan et al., 2013). Leifer and De Leeuw (2006) used a photographic system to study bubble plumes and individual bubbles generated by breaking waves in a wind-wave tunnel. Vagle and Farmer (1992) used a multifrequency acoustical-backscatter technique to investigate bubbles size distribution. Terrill et al. (2001) carried out an acoustic instrument mounted with the buoy at offshore Point Conception, California to measure the bubble size distribution from wave breaking. Lamarre and Melville (1992) measured void fraction in bubble plume generated by breaking waves by using the developed conductivity probe which carried out in the field observation and laboratory experiment. However, each technique has a limitation and condition. For example, the signal from conductivity probe is saturated in the vicinity of breaking wave crest, the acoustic techniques require careful calibration and/or calculation procedures to analyze the data, the photographic technique is more complicated to process automatically. Hence, all of these techniques have been continuously developed to get the more accurate results.

Using the opitical method, wave breaking is distinguishable where the incident

light is randomly scattered by bubbles and droplets present in the wave roller, a turbulent mass of air and water that is generated during the breaking process. Therefore, the breaking waves are brighter than that of non-breaking waves in the optical images. Frouin et al. (1996) reported the foam-covered areas have a large albedo and reflect about one order of magnitude more than the foam-free areas by measuring sea surface radiometric. At this point, the the observed bubbly and nonbubbly surface have been applied to investigate the breaking wave dynamics. However, this technique cannot directly identify the active foam ramnant and relict foam, and it also can only work during daylight time. Some works attempted to discriminate between active and ramnant foam using thresholds intensity (Ross and Cardone, 1974), or an approach based on wave kinematics (Mironov and Dulov, 2008). Mostly, the presence of bubbles enhance the error in the analysis of breaking wave dynamics. On the other hand, we can apparently use this opitcal images to analyze the bubble characteristics. The ARGUS video system, an example of optical method, widely used to study the surfzone dynamics [Holman and Stanley (2007); Catálan and Haller (2008); Catalán et al. (2011)]. Also, the ARGUS video system was applied to study wave rollers. Haller and Catalán (2009) analyzed the remotely sensing data (composed of optical and radar scattering images) and phase-averaging technique to determine wave roller length generated in large wave plume.

In Chapter II, we analyzed six data set or runs of the optical intensity signal from individual breaking waves from large-scale laboratory experiment. The intensity signal data from Argus video were provided by Dr. Patricio Catalán. The image processing and autocorrelation technique were developed for studying the bubble characteristics in terms of length scale and spectral width. This work will be submitted to Experiments in Fluid.

1.2 Low frequency waves

According to the analysis of bubble characteristics from the optical intensity images in the previous section, we found that the breaking point forcing was influenced by basin seiching wave. Haller and Özkan-Haller (2007) also reported that the wavefrequency was modulated by unsteady current caused by either water elevation or current. These lead us to hypothersize that There is a positive feedback between seiching effects (i.e. time varying currents, water surface elevation, and the absolute frequency) and the breaking forcing..

The influence of wave-current interaction can be essential in nearshore hydrodynamic processes, hence; it should be considered. The theory of wave-current interaction is well developed in case of depth-uniform currents, but there are few studies considering the unsteady currents and/or total water depth. For example, Tolman (1990) found that the unsteady depths and currents should account for the wave propagation in the North Sea, Jones (2000) investigated the interaction between tides and waves on the wave refraction at the coast of south-west Wales, U.K. through numerical model, Özkan-Haller and Li (2003) presented the effect of wave-current interaction in the wave-driven longshore currents model, and Yu and Slinn (2003) noted the significant feedback mechanism on the dynamics of rip currents. Nonetheless, any recent numerical models report the effect of wave-current interaction on low frequency wave or standing seiching wave.

Unsteady current can be caused by many reasons such as tide, and low frequency motions. Low frequency wave is significant for nearshore hydrodynamics because it may modify the incident wave field, water surface fluctuation, and also play essential role in sediment transport which lead to the formation of bar, and more complex morphology (O'Hare and Huntley, 1994). Surf beat, an example of low frequency wave, was originally found and named by Munk (1949). Surf beat generally has a period

within the order of minutes. A number of studies have been proposed the mechanisms for surf beat. There are two main mechanisms for surf beat generation including the release of Bound Long Wave which was firstly proposed by Longuet-Higgins and Stewart (1962), and breakingpoint forcing which was firstly proposed by Symonds et al. (1982). Laboratory experiment, field data, and numerical models have been studied to support both mechanisms [Baldock (2012); Contardo and Symonds (2013); Pomeroy et al. (2012)]. In this study, we will focus on basin seiching wave.

Seiching is the formation of standing wave in water body, due to wave formation and subsequent bounds back from the end. These waves may be incited by seismic activity (earthquake motions, tsunamis), prevailing wind over the surface, or due to wave motions entering the basin. As waves propagate toward the shore, then they refract, reflect, shoal, and break. Those wave behaviors depend on many factors such as the incidental angle of the incoming wave with the shoreline, the bottom profile, and the shoreline morphology. Therefore, if the seiching is produced, it will impact on the motion of wave, surface elevation, and currents. As in the wave basin case, they may reflect, redirecting non-dissipated wave energy back through the surf zone. Mostly, the generation of wave in the enclosed basin produces basin seiching because of wave reflection and nonlinear energy transfer.

Several recent numerical model studies widely used two different approaches including of fully coupling wave-current interaction based on Boussinesq equations model and semi-wave-current interaction model. The first approach, for example, Chen et al. (1999) utilized the extend Boussinesq equations to study rip current system from the experiments (Haller et al., 1997). This approach resolves the wave motion and the generated current simultaneously. Hence, this approach cannot emphasize the results with and without the wave-current interaction. The others approach, the coupling between wave and current appears through the radiation stress gradient term

due to waves (taken as a forcing in the momentum equation) and through wave-current interaction terms [Loguet-Higgins and Stewart (1996); Longuet-Higgins and Stewart (1962); Yu and Slinn (2003); Özkan-Haller and Li (2003)]. Nevertheless, this approach can not be justified in case of strong current. Therefore, the second approach will be chosen in this study since this approach will show the distinctive results between with and without wave-current interaction.

In Chapter III, this work is motivated by the results from large-scale laboratory experiment in Chapter II. The observations of wave frequency modulations from a large-scale laboratory experiment were presented. The numerical model based on the depth- and time-averaged Navier Stokes equation along with the wave action balance equation is utilized in this study. In particular, various monochoromatic wave conditions are simulated to generate the basin seiching waves on the closed boundary condition. The results presented in Chapter III will be submitted to Journal of Fluid Mechanics.

2. Analysis of Surface Foam Events Produced by Waves in a Laboratory Surf Zone

Jitraporn Phaksopa and Merrick C. Haller

Manuscript will be submitted to:

Experiments in Fluids

Wave breaking plays an important role in many oceanic processes. It is a primary dissipation mechanism for surface gravity waves and it is also a conduit for ocean-atmosphere interactions (e.g. Melville and Rapp (1985)). When waves break, air and water mix and create a two-phase flow and whitecaps are the surface expressions of this flow. There is an extensive body of literature devoted to relating the areal coverage of whitecapping to the winds at the ocean surface (for a review, see Goddijn-Murphy et al.. Whitecap coverage is also the basis for parameterizations for air-sea gas exchange (Woolf, 1997), marine aerosol production (Monahan et al., 1986) and the ocean albedo (Frouin et al., 1996).

Callaghan et al. (2012) noted the wide range of scatter (by a factor of 50) across lab and field observations of whitecap decay times. From their laboratory observations they concluded that varying levels of surfactants play a key role in this scatter but that, in the absence of surfactants, surface foam lifetime is indicative of subsurface bubble plume degassing time, which is in turn dependent on wave scale and breaking wave slope. Blenkinsopp and Chaplin (2011) conducted experiments using freshwater, artificial seawater, and natural seawater and found only minor differences in the observed time-dependent void fractions and the total volume of entrained air. In addition, bubble sizes produced by breaking were comparable in the three water types, but an additional population of very small bubbles was generated in the two seawater cases. With a bubble plume modeling exercise, they simulated a breaking wave height of 10 cm (lab scale) and 2m (field scale) and concluded that scale effects had the largest impact on the simulated bubble plume evolution.

With a breaking wave analog in the laboratory, Callaghan et al. (2014) investigated the effect of water temperature on the subsurface bubble plumes and surface foam decay. They found that temperature effects on whitecap coverage were less important than the previously discussed effects of water chemistry and wave field

characteristics. Their results also supported the hypothesis that the rate of change of surface foam area reflects the evolving variation of the total bubble cross-sectional area, which indicates a useful relationship between subsurface bubble population and its surface expression.

In nearshore waters, wave breaking is most often depth-induced and takes on some different characteristics then in deep water. Specifically, once a wave starts to break, it tends to continue dissipating as it propagates into decreasing water depth until it reaches the shoreline. However, the wave energy decay does not have to be monotonic, on a beach with an alongshore "bar and trough" morphology, wave breaking is initiated over the bar crest but may cease through the deeper trough and then re-initiate at the shoreline. Regardless of the nearshore morphology, in the surf zone the breaking portion of the wave is termed the "surface roller" and its characteristics are most often parameterized as propagating hydraulic jumps or bores.

Nadaoka et al. (1989) showed that surf zone waves generate "obliquely descending eddies" behind the wave crest and there have been many investigations of these eddies and associated turbulence (e.g. Ting [Coast Eng], 2008; Huang et al., 2010), their bubble production (e.g. Cox and Shin (2003)), their interaction with the bottom (e.g. Cox and Kobayashi (2000); Govender et al. (2004)), and their potential for suspending sediment (Voulgaris and Collins, 2000). There has been very few modeling studies of air bubble production by waves in the surf zone. Shi et al. (ICCE, 2008) made only a qualitative comparison between modeled and observed surface bubbles in a laboratory surf zone (same dataset analyzed herein). Shi et al. (2010) made quantitative comparisons with the void fraction and bubble size observations from the lab experiments of Rapp and Melville (1990) and Lamarre and Melville (1991). Ma et al. (2011) conducted three-dimensional modeling of bubble entrainment and void fraction evolution and compared to the laboratory surf zone measurements of Ting

and Kirby (1994) and Ting and Kirby (1996).

Most previous experimental observations, whether in deep or shallow water, have concentrated on the initial air entrainment plume and the evolution and degassing of the bubbles generated at the beginning of the breaking process. However the early experimental work of Yeh and Mok (1990), using laser-induced fluorescence, analyzed turbulence generated in shallow water bores and identified the intermittent production of turbulent patches by the surface roller. They conjectured the existence of a "generation-advection" cycle in shallow water surface rollers and presented a scaling argument for the frequency of turbulent patch production based on the Strouhal number. Watanabe and Mori (2008) analyzed the production of vortices by the surface roller using infrared observations in a laboratory surf zone along with a limited set of field measurements and numerical simulations. They analyzed the vorticity length scales in the spanwise direction; however, they did not address the length scales of turbulence in the wave propagation direction. Later, Mok et al. (2013) carried out additional experiments also confirming the generation-advection model for turbulent patches generated by surface rollers.

Previous numerical simulations have only concentrated their analysis on the initial stages of breaking and the evolution of the primary turbulent bubble plume event. For example Shi et al. (2010), models produce a continuous decay of air entrainment, not the patchiness of data. This intermittancy has not been demonstrated in most models to date (Liang et al. (2011); Ma et al. (2011)). Yet, the existence of separate bubble plumes seprated in the wave propagation direction is evident in the photographs of Rapp and Melville (1990) and Callaghan et al. (2013) and was explicitly identified by Yeh and Mok (1990), Rojas and Loewen (2010). The very recent modeling effort of Derakhti and Kirby does demonstrate the existence of a secondary bubble cloud and they present analysis of the bubble void fraction and demonstrate

that it has a peak approximately 70% of the wave phase behind the crest, which is consistent with the observations of Rojas and Loewen (2010).

Catálan and Haller (2008) analyzed breaking waves in a laboratory surf zone using optical remote sensing. Cross-shore transects of optical intensity show the surface signals of episodic bubble plume production by shallow water breaking waves. An example time-space plot of optical intensity is shown in Figure 2.1. The oblique, bright (i.e.red) linear features traversing the image represent the trajectories of the breaking wave crests. The more stationary (i.e. trending vertically in the image) features are surface foam events that are left behind the crest and they appear to occur and fairly regular intervals.

In the present work we will use these data to analyze the spacing of these episodic events in the direction of wave propagation and compare to the model of Yeh and Mok (1990). In addition, we will analyze the observed event decay times and compare to the previous work of Callaghan et al. (2013) and Callaghan et al. (2014).

2.1 Methodology

2.1.1 Set up

2.1.1.1 Wave conditions

Laboratory experiments were conducted to generate waves in the Large Wave Flume (LWF) at the O.H. Hindale Wave Research Laboratory (Oregon State University). The LWF is approximately 90 m long, 3.7 m wide, and 4.6 m deep. The LWF coordinate has the x-axis pointing onshore along the centerline with the origin at the wavemaker. The bathymetry was configured in a piecewise continuous, barred morphology (concrete slab, no sediment). The free surface elevation were recorded at sampling rate 50 Hz by resistance-type wave gauges at 6 fixed locations x= 23.45,

45.40, 52.73, 60.04, 70.79 and 81.97 m as shown in Figure 2.1. The six experimental regular wave conditions are listed in Table2.1. The further details of the experimental procedure can be found in the work by Catalán (2005) and Catalán and Haller (2005).

2.1.1.2 Video measurement and processing

Simultaneous video observations were collected using ARGUS III video station (Holman and Stanley, 2007). It composed of 3 digital cameras mounted near the laboratory ceiling at the different sections of the flume. The camera were 9.88 m above the still water level and the field of view of the cameras spanned the cross-shore from x = 41.7 m to x = 100 m (the dry beach). The sampling rate was 10 Hz for all cameras. Further details of the video data processing can be found in the work by Catalán (2005). Figure 2.2 shows an example snapshot of the OSU-LWF during the experiment.

2.1.2 Data Analysis

The remotely sensed video intensity data of six runs from the above experiment were analyzed. The data products that were used for this analysis were the pixel intensity timestacks in time-space maps. Each of pixel intensity has a vlaue in a range between 48 and 126 waves (in Table 2.1). The truncated time stacks were resampled to a uniform 10 Hz grid with a resolution of 1 cm in pixel array.

Figure 2.1 shows examples of intensity time stack from Runs37 and Runs 40 with the bathymetry and wave height from 6 guages in this experiment. Due to different offshore wave conditions, some waves were breaking all the way through the shore break point. However, some waves were not breaking around the bar crest through bar trough, and then breaking again around the shoreline.

The six experimental regular wave conditions are summarized in Table 2.1 which lists the name of each run, number of waves in data record, wave period (T), deep water wave height (H_0), deep water steepness ($\frac{H_0}{L_0}$), Iribarren number (ξ_b) at the break

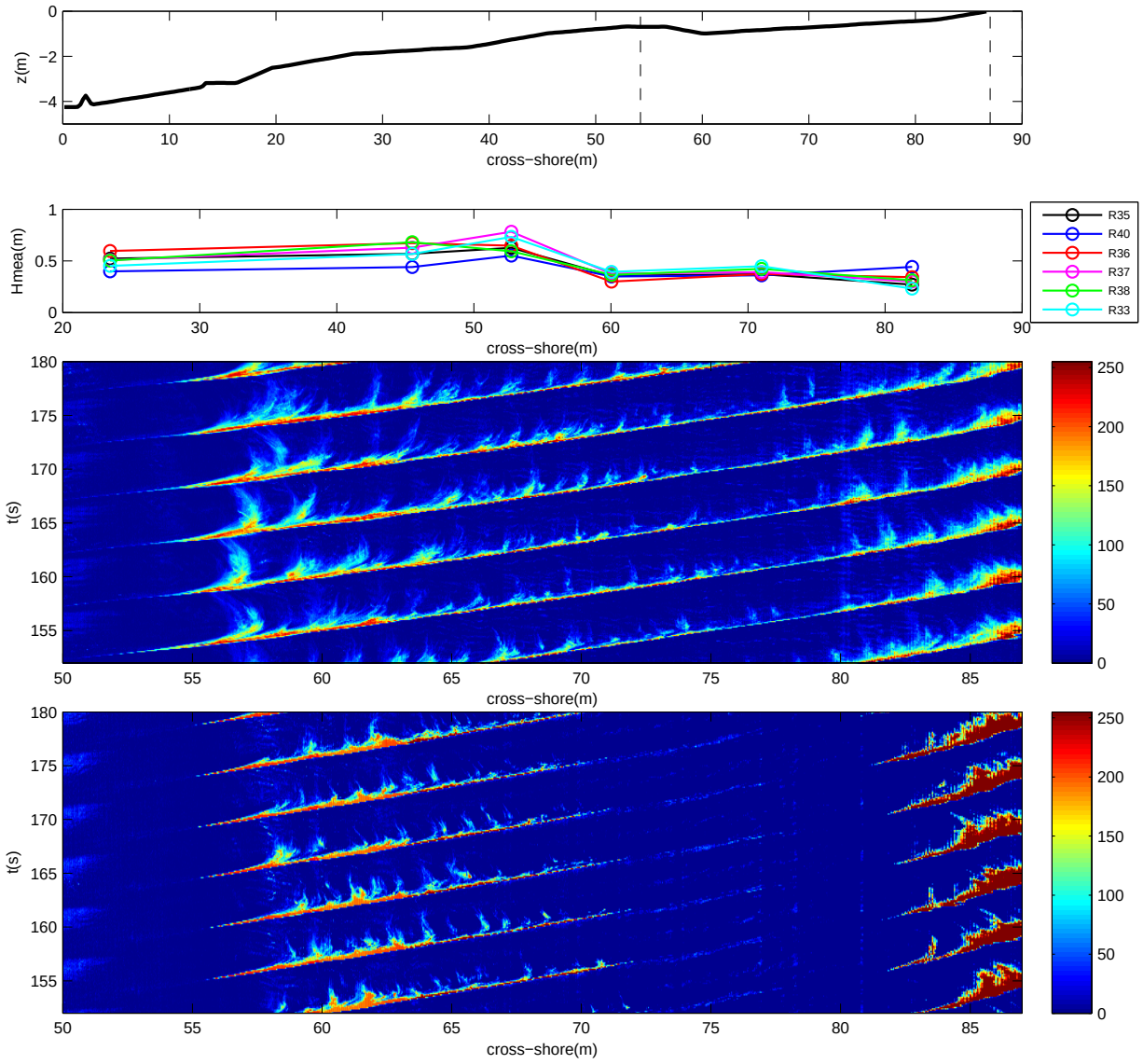

FIGURE 2.1: (top) vertical elevation of the fixed bed. Vertical dashed lines represent the domain for the intensity time stacks. Experimental conditions: (second panel) measured wave heights for six runs. (third panel) The intensity time stack from Runs 37. Waves start breaking around the location $x = 52m$ and continually breaking through the shore break. (forth) The intensity time stack from Runs 40. Wave were initially breaking around $x = 55\,m$ and stop breaking around bar through and breaking again at the shore break.

TABLE 2.1: Wave conditions: no. of waves in the data record, wave period (T), deep water wave height (H_0), deep water steepness (H_0/L_0), Iribarren number** (ξ_b), and deep water wavelength (L_0)

Run	No.	$T(s)$	$H_0(m)$	H_0/L_0	ξ_b	$L_0(m)$
35	126	2.7	0.57	0.050	0.18	11.38
40	81	4.0	0.40	0.016	0.28	24.98
36	97	4.0	0.63	0.025	0.25	24.98
37	77	5.0	0.51	0.013	0.29	39.03
38	61	6.0	0.47	0.008	0.38	56.20
33	48	8.0	0.37	0.004	0.49	99.92

** $\xi_b = \beta/\sqrt{\frac{H_b}{L_0}}$ where β is the representative slope (1/24), corresponding to the shoreward face of the bar and H_b is the waveheight at the break point.

point with a representative slope (β = 1/24), and deep water wavelength (L_o). The Iribarren numbers indicate that the breaking type was spilling ($\xi_b < 0.4$) to plunging ($0.4 < \xi_b < 2.0$). Figure 2.1 shows an example of the intensity time stack from the experiment. The oblique, bright (i.e. red) linear features transversing the image represent the trajectories of the breaking wave crest.

To analyze the surface foam areas and length scales, the first step was transformation the intensity time stacks to the new coordinate system (Galilean transformation). The procedure is described below.

2.1.2.1 Galilean Transformation

From the intensity time stacks, we transformed all data to the new coordinate system (moving coordinate frame). The new coordinate system, the observer is propagating with wave phase speed (C) and time is relative to the time at each wave crest. The first step was to identify the wave crests passage along the flume. Next, the

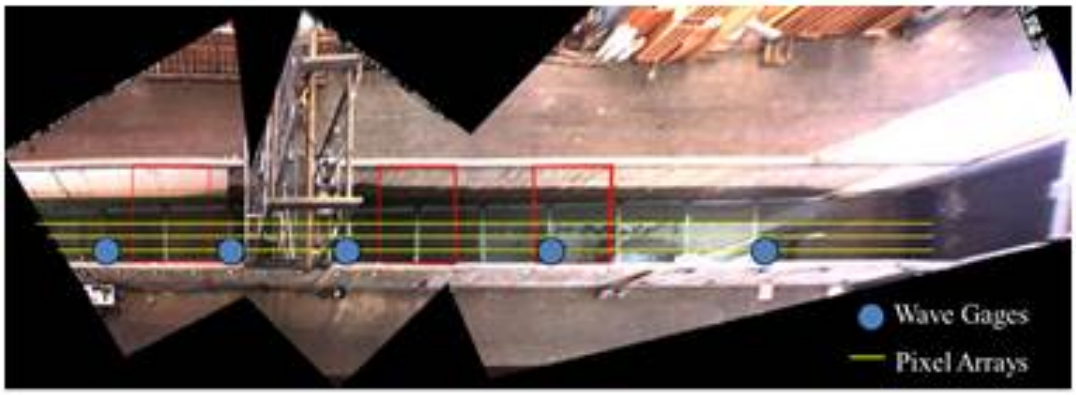

FIGURE 2.2: An example snapshot of the OSU-LWF during the experiment. (Top) It clearly shows bubble plume at the front face of the progressing wave. (Bottom) Top view of the experimental set up. It shows the wave gages locations.

averaged track was chosen to be a reference to shift in time in terms of cross-shore location for each time step.

Edge detection is a technique for detecting the edge of gray-level discontinuities by defining first and second order digital derivatives for detection the edge of edges in an image (Gonzalez and Woods, 2001). This feature aims to identify the progressive of wave passage from the optical intensity time stack that uses the threshold value to separate wave trajectories and bubble tails from the unbroken background water. First, all time stacks were converted into a grayscale intensity image of double decision. In gray-scale time stack, the pixel intensity has a value ranging between 0 (black) and 1 (white). Edge detection feature begins by reading a grayscale intensity image, defining the gradient magnitude between the connected pixels, and reimaging in grayscale image. The edge pixels with a lower (higher) gradient magnitude than the predefined threshold were kept, i.e., written out black or 'zero' (white or 'one'). All new pixels therefore have only two values- zero and one.

For tracking the trajectory of each wave, the first breaking point of each wave was identified in the first step and store in the location and time. Then we tracked the passage of wave by storing the location (space and time) if the pixel value was equal to one as well as its intensity of a given time stack $I(x,t)$, and then the next location (no time change) was continuously checked until reaching a zero-valued pixel next by next. If the next pixel value was equal to zero, this pixel location was not kept and the trajectory moved to the next pixel of the next time step (the same position). This process kept running until the last white pixel of each passage. Finally, we get the array of location and time of each wave passage for all progressive waves.

Then, for shifting in time, we chose the averaged trajectory for each run, and then subtracted each time position of this trajectory with time of the first breaking point of its trajectory (x_1, t_1). Finally, we get the subtracted data representing as the

time-shifting data for each run (t_{shift}).

$$t_{shift} = t - t_1; \tag{2.1}$$

In order to create the new array of pixel intensity, we need to create the zeros array of pixel intensity data expression as $I_2(x_{new}, t_{new})$. The new time dimension (t_{new}) is

$$t_{new} = t + \tau_t \tag{2.2}$$

where τ_t is the maximum value of t_{shift}. Next, the original pixel intensity data is shifted and replaced into the new array I_2. Mathematically, we can represent this process by the following relation

$$\begin{aligned} I_2(x_{new}, 1 : t_{new}) = I(x_{new}, (\tau_t + 1) - (\frac{1}{\Delta_t} * t_{shift}) : \\ (\tau_t + t) - (\frac{1}{\Delta_t} * t_{shift})) \end{aligned} \tag{2.3}$$

Figure 2.1 (last panel) shows the intensity timestack in the new coordinate system. The intensity timestacks in the new coordinate system are used to analyze the bubble patches characteristics including of area (decay time) and length scales.

2.1.2.2 Surface foam area

To seperate the surface foam or bubble plume from the background water, a threshold pixel intensity was applied to each intensity pixel. The threshold was determined by using $\overline{I} + \sigma_I$, where $\overline{I}$ and σ_I are the mean and standard deviation of the pixel intensity of a given timestack $I(x, t)$. This threshold was followed Catálan and Haller (2008). To determine the total area of surface foam, the pixel intensity were converted into a binary mask (a value is 0-black and 1-white). The binary intensity replaced all pixels in the original pixel intensity greater than the threshold with the value 1 (white) and replaced all other pixels with the value 0 (black) as shown in figure 2.3. The intensity magnitudes are no longer used in this analysis. We assumed

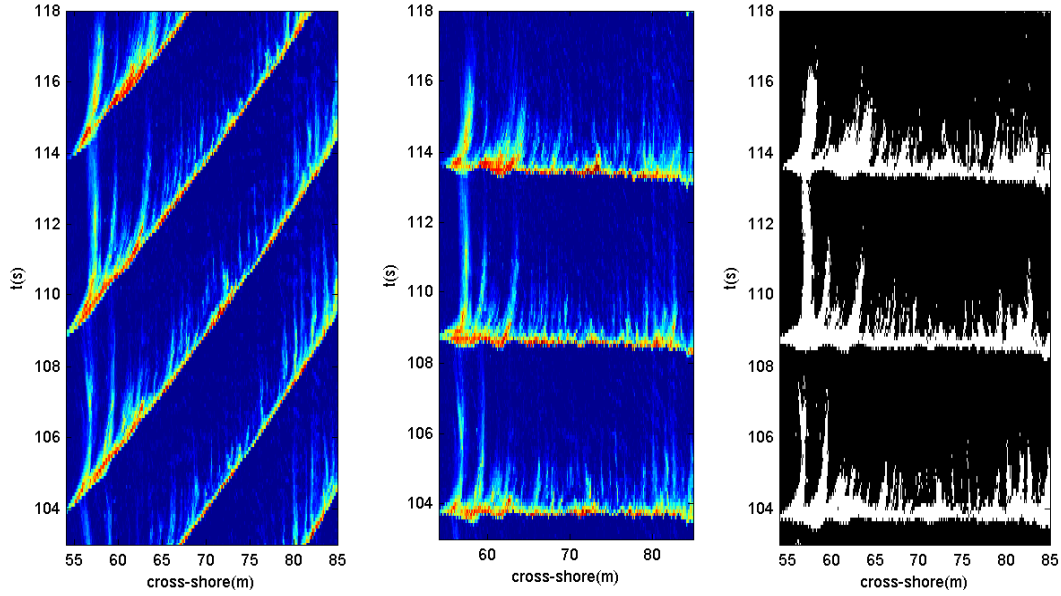

FIGURE 2.3: Portion of time stack from Runs 37 (the pixel intensity:0-250). (left) the intensity time stack (middle) intensity time stack in new co-ordinate system (Galilean Transformation) (right) the binary mask time stack by using threshold ($\overline{I} + \sigma_I$)

the pixel intensity was uniform along the width of the LWF. At times, the total area (A) was calculating by

$$A = w * (no.of white pixels) * \Delta x \tag{2.4}$$

where w is the width of the LWF. The unit of area (A) is m^2.

As mentioned in the previous section, some waves were breaking over the offshore bar through the shore break. On the other hand, some waves were breaking over the offshore bar through the trough region, and then breaking again at the shore break. Hence, the total bubble patches area was determined in two different domains ($D1$ and $D2$). The domain ($D1$) was bounded from the bar crest region $x = 52.73m$ (guages 3) through $x = 60.04\,m$ (guages 4) and the domain ($D2$) was bounded from the bar crest region $x = 52.73\,m$ (guages 3) through $x = 81.97\,m$ (guages 6).

2.1.2.3 Surface foam length scales

The length scales is defined as the distance between two adjacent bubble patches. We analyzed the length scales from this data set by two different schemes including of discrete length scales and spectral analysis length scales. There is an existing of prediction model for turbulence patches length scales by Yeh and Mok (1990).
From the description of wave roller by Duncan (1981), the wave roller propagates with wave phase speed (C). Since the wave roller is the origin of large eddies and the turbulence is created by intermittent advection of the recirculation flow of the surface roller. Therefore, the frequency of turbulence patches (f) can be determined by

$$f = \frac{C}{\lambda} \tag{2.5}$$

where λ is the distance between patches or the length scales. Yeh and Mok (1990) proposed the periodic surface-roller formation model for bores. The frequency of turbulence patches is the excursion time of a fluid parcel traveling around the surface roller as described below:

$$t = \frac{2Lr}{C} \tag{2.6}$$

$$f = \frac{C}{2L_r} \tag{2.7}$$

where L_r is the surface roller ($L_r = \eta cot\gamma$), γ is the the slope of the bore front from the horizontal. From eq (2.5) and (2.7), the length scales (λ) can be presented by

$$\lambda = 2L_r \tag{2.8}$$

In this part, we used the surface roller data determined from this data set provided by Haller and Catalán (2009). For comparison, this length scales prediction was assumed the flow in front of a bore is quiescent.

The discrete length scales is the distance between the first and second bubble events from the new coordinate system of the intensity timestacks. Those peaks can

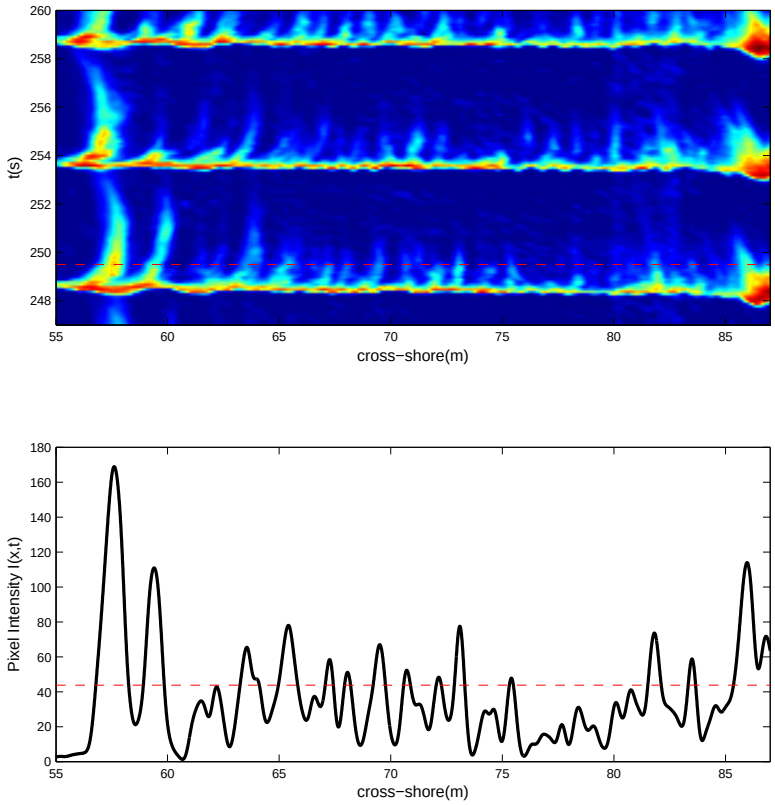

FIGURE 2.4: Example video data from Run 37 (top) timestack of the smoothed $I(x,t)$ with running average (2.5 m window) with the horizontal dash line indicating at $t = 249.5s$. (lower) Cross-shore variation of pixel intensity $I(x, t = 249.5s)$. Dashed line is the threshold value $(\overline{I} + \sigma_I)$

be identified by applying some spatial smoothing (using the running average) with 2.5 m window and zero-upcrossing of a threshold pixel intensity value chosen here as $\overline{I} + \sigma_I$ (same as the previous section) as shown in figure 2.4.

Moreover, the bubble events are sporadic as seen in figure 2.4. Whether the dominant length scales was seen in the intensity time stack or not, the best way to reveal it is by comparison of the length scales from the first two of the intensity peaks (λ_2) and the average length scales from ten bubble events (λ_{10}).

To estimate the length scales from spectrum analysis, the pixel intensity data are represented in number varying from 0-255 and are Fourier transformed in space

domain at each time step. For analyzing the intensity data, the spectral density function (PSD), and spectral bandwidth is determined for each run by the following steps. All optical intensity data are Fourier transformed in space domain with 50 m^{-1} Nyquist wavenumber for every time step (0.1 seconds). Before calculating FFT for each time step, all optical intensity data are de-trended (by subtracting the original time series with the low pass frequency (every 250 data in space domain), and tapered by using Hanning window. We choose just positive wavenumber power spectrum (1- sided PSD). Next, the 1-sided PSD are smoothed by applying band averaging procedure with 8 Degree of Freedom (DOF). Hence the new resolution of time is 0.4 second.

There are several equations for calculating the spectral bandwidth parameters for different purposes. The spectral bandwidth parameter was introduced by Cartwright and Longuet-Higgins (1956) in order to describe whether the wave energy is concentrated within a narrow wavenumber or frequency band ($\nu \to 0$) or not ($\nu \to 1$). In this study, the spectral bandwidth is calculated by using the following equations (Vandever et al., 2008)

$$\nu = \sqrt{\frac{m_0 m_2}{m_1^2} - 1} \tag{2.9}$$

$$\epsilon = \sqrt{1 - \frac{m_2^2}{m_0 m_4}} \tag{2.10}$$

where m_n is the n-th order spectral moment and is given by

$$m_n = \int k^n S(k) dk \quad \text{for all wavenumber} \tag{2.11}$$

where n is the order of the moment such as m_0, n is equal to zero.

Next, the spectral length is the width of the energetic part of the spectrum. Previously, there have been various formulae to calculate the mean wave period from frequency wave spectrum such as the spectral significant wave period ($T_{m-1,0} = m_{-1}/m_0$), and the mean wave period ($T_{m02} = \sqrt{m_0/m_2}$) (Goda, 2010). Likewise, the mean length

should be calculated in the same way for wavenumber spectrum. Therefore, the mean length was also defined as

$$L_{mean} = \frac{m_{-1}}{m_0} \tag{2.12}$$

$$k_{mean} = \frac{2\pi}{L_{mean}} \tag{2.13}$$

We choose the minus and first moment to calculate the mean length $L_{m-1,0}$ since it is not significantly affected by the high wavenumber part of the spectrum.

According to Pinkel (2008), the bandwidth pattern of the spectrum obviously showed on the normalized spectrum. The advantage of the normalized spectrum made the spectrum having the identical variance.

To illustrate the spectrum length distribution, the spectrum length pattern is more apparent when the spectrum is normalized by using this following equation

$$NormalizedPSD = \frac{S(k)}{\int S(k)dk} \quad \text{for all wavenumber } k \tag{2.14}$$

Here it was assumed that the spectrum bandwidth pattern for all run have a sinusoid shape, so the zero-upcrossing procedure was applied to determine the averaged spectrum band width for each run. The zero-upcrossing method assumes that the deviation of spectral width is the distance between when the spectrum width goes from the minimum to the maximum value. Therefore, the deviation of spectral width was determined for each wave and then averaged to get the identical value for each run.

2.2 Results and Discussion

2.2.1 Bubble Characteristics

Totally, we analyzed bubble data from 466 individual breaking waves (6 Runs) as shown in Table 2.1. For each Run, the analysis was started about the breaking point through the shore break point of each wave as shown in figure 2.1. The video intensity data captured the evolution of the wave passage coincident with bubble plumes of each wave as shown in figure 2.5a. As mentioned in the previous section, Figure 2.5a expresses the foam is released from the breaking wave (let's say crest) with about the regular space. It is spreading upward from bright region trajectories and then decaying with less than one wave period. Bubble is generated when air is entrained into the water column by the overturning crest of a breaking wave. It also shows the bubble foam was generated and released from wave crest shown in the form of bubble tails with almost regular spacing for each wave. The bubble tails imply that most bubbles did not move along with wave. Some those bubbles facing the obliquely descending eddy were trapped in the within the vortex. If the trapped bubbles had more buoyant force, these bubbles rose and disappeared. As the same time, rest of trapped bubbles remained within the part of the obliquely descending eddy. Nadaoka et al. (1989) showed that large-scale eddies generated by turbulence: "horizontal eddies" and "obliquely descending eddies". Horizontal eddies were occurred beneath the front face of wave crest (its axis parallel to the crest line) while the obliquely descending eddies consequently generated behind the wave crest. Watanabe et al. (2005) found that the obliquely descending eddies generated by eddies around the front face extended obliquely downward to inertia region at around 45° concluded that bubbles were transported to the certain depth by the horizontal eddies.

Moreover, the first breaking positions were essentially different because of the influencing of the standing wave (low frequency oscillation). The time stacks do indicate the long wave modulations, but the influence of the standing waves on breaking

and bubble events is the subject of the future work (Chapter 3). We found that the low frequency wave period about 54 s by tracking along the first bubble tail of each wave. This long wave characteristics are expected to be similar for all Runs. This is closed with the predicted frequency of the lowest seiching mode (0.0185 Hz) and the dominant peak from energy spectrum at 0.0183 Hz or 54.6 s (Haller and Özkan-Haller, 2007).

In this present work, we focus on the breaking area or surf zone, therefore all pixel intensity time stack image for all runs were cropped only around breaking area, and were also shifted in time scale to reduce tilting in time of all images. However, the new cropped and shifted in time of pixel intensity images do not impact on the accuracy of the original intensity data for all runs. In general, the bubble tails were detected by ARGUS camera as shown in the previous figures. Obviously, the first bubble tail was not produced at the breaking point but it was delayed about 5 m further way from the breaking wave (bar crest location). Likewise, they were similar results for all experimental observations. Addtionally, wave breaking turbulence was largest at this location (Scott et al., 2005). Yeh and Mok (1990) reported that when the surface-roller is created on the front surface, the elongated recirculating eddy is advected behind the front or called "generation-advection" cycle. Then, the evolution of bubble refered to as whitcap can be divided into two phases (Deane and Stokes, 2002). The first phase, the acoustically active phase, was begun when bubbles were formed by breaking waves, which took a very short time around a millisecond to a second. This phase is accompanied by a burst of noise [Loewen and Melville (1991); Loewen and Melville (1994); Deane (1997)]. The second phase of quiescent plume was begun after the generated bubbles creased until it was decayed. This phase evolves with many processes i.e. turbulent diffusion, advection, buoyant degassing, and dissolution. Next, the another wave-roller begin to form, and so on. Anyway, the timescale of bubble depends on many factors such as temperature, salinity, and

surfactant [Callaghan et al. (2013); Callaghan et al. (2014)]. Therefore, the analysis of each bubble tail is hard to analyze because the association of new bubbles from the adjacent breaking waves. However, these pixel intensity images provide a straightforward way to figure out the decay time of each bubble tail.

Figure 2.5b depicts the time series of pixel intensity along the cross shore at different times (102.5, 103.5, 104.5, and 105.5 s) which represent examples for the different wave stages. Essentially, it clearly shows the pixel intensity is very distinctive for breaking versus non-breaking. At $t = 102.5\,s$ (breaking), the pixel intensity is about in the saturation stage (the saturated value around 200-255) at gauges 2 and 3. At gauges 3 and 4, the pixel intensity dramatically decreases compared with the pixel intensity at gauges 2 and 3. At $t = 103.5\,s$, it is possible to see three obvious pixel intensity peaks. These peaks are corresponding with the foam released by breaking wave. At $t = 104.5\,s$, there are still some peaks with less magnitude comparison to the pixel intensity at $t = 103.5\,s$. It implies that the foam is about to disappear from the tank. At $t = 105.5s$ the pixel intensity is very low along the cross-shore. Almost the foam decays to the background. We noted that the age of the foam is less than wave period for all runs.

For bubble size distribution, it is generally composed of a variety size of bubble underneath the whitecap. Note that, this pixel intensity time stacks cannot describe in detail of all bubble size distribution and bubbles void fraction during the experiment for all Runs.

2.2.2 Surface foam area

The analysis produced the temporal variation of surface foam area initially produced by breaking wave, then decayed, and finally disappeared from the water surface. At times, the surface foam area is defined by summation of number of pixels above

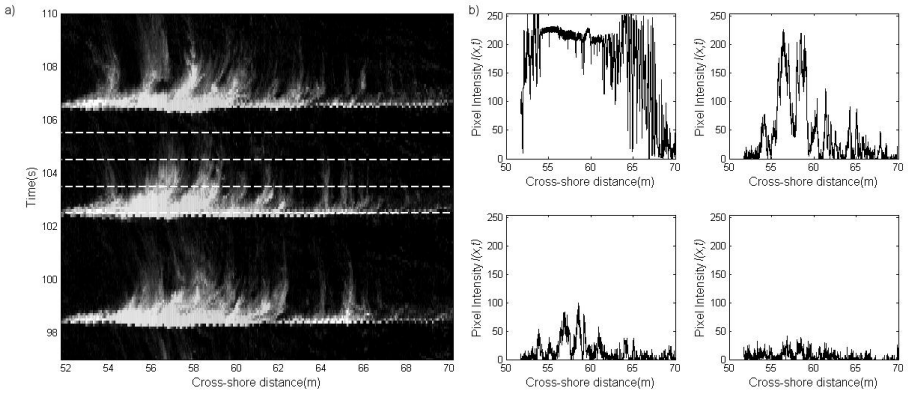

FIGURE 2.5: Example of video data from Runs 36 a) time stack $I(x,t)$ with the horizontal line indicating at time $t = 102.5, 103.5, 104.5, 105.5s$ b) pixel intensity times series for different times $I(x, t = 102.5, 103.5, 104.5, 105.5s)$

the threshold pixel intensity value $(\overline{I} + \sigma_I)$ of the pixel intensity of the given time stack $I(x,t)$ mutiplying by the LWF width. The total area is determined from two different boundarie-$D1$ and $D2$. Both surface foam areas are compared with the pixel internsity and determined the decay time.

An example portion of a processed time stack is shown in figure 1.4. Figure 1.4 shows an overlay of the the temporal patterns of the surface foam area and the normalized mean intensity. Figure 1.4(top) shows portion of binary mask time stack for Runs 37. White pixels represent the existence of bubbles produced by breaking waves. It shows that an initial rapid growth of surface foam areas around wave crests, then followed by a more gradual decay until disappeared before the next coming wave as seen in figure 1.4 (lower). We choose to model the decay of whitecap foam with a simple exponential model as described by

$$A = A_0 exp(-t/\tau) \tag{2.15}$$

where $A(t)$ is the time variation of bubble area during the decay period, A_0 is the bubble area at the beginning of each wave (maximum area) and τ is a constant called

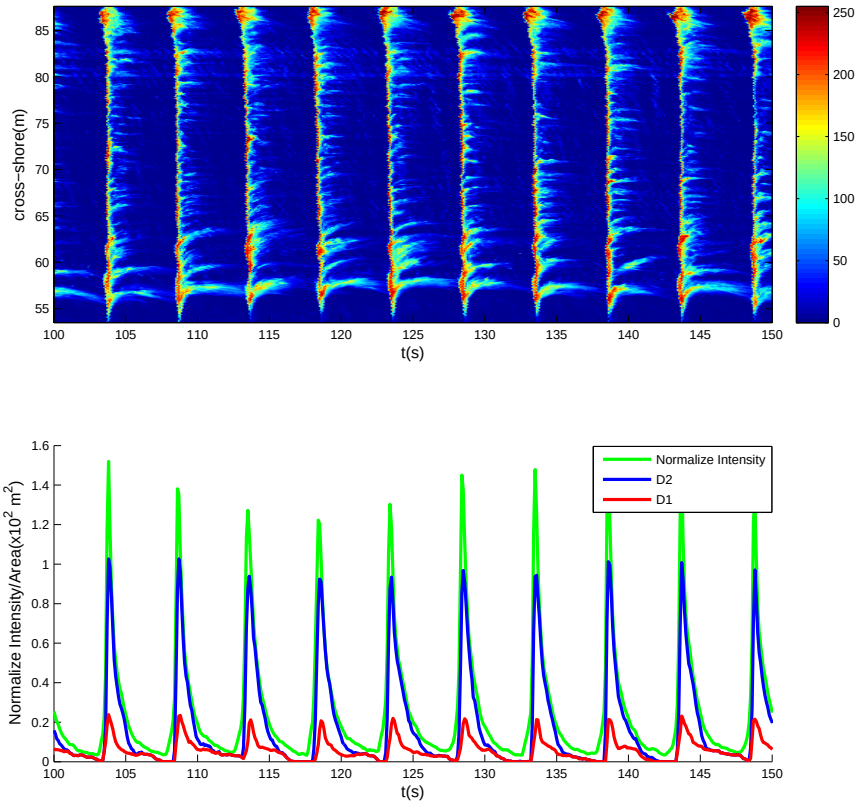

FIGURE 2.6: An example portion of a processed time stack (Runs 37): (top) intensity time stack from $t = 100 - 150s$, (bottom) time variation of surface foam area (m^2) (D1 and d2) plot over the normalized mean intensity

'decay time'.

Figure 2.7 shows the time evolution of bubble areas of five waves from Runs 37 and the fitted exponential decay curves with different decay times (τ). Figure 2.8 shows the evolution of bubble areas from $D1$ and $D2$ from the same breaking wave of Runs 37. This bubble event decays with different decay times 1.06 and 0.66, respectively. The surface foam areas from $D1$ in figure 2.8 (top) originally decay more faster than the exponential model but figure 2.8 (lower) closely follow an exponential decay. The surface foam area abruptly increase before the end of the decay curve. This variation is typically seen in each wave. These due to some bubbles were brought

back to the surface by turbulence and buoyancy.

Time series of surface foam area for 6 Runs are shown in figure 2.9. In general, the maximum foam area increases with increasing ξ_b for both domains. However, there are some exceptions in Runs40 with ξ_b = 0.28. Neverthless, the total surface foam area is highly related with ξ_b. Comparison with results from Callaghan et al. (2013), they found that the correlation between the surface foam area with increasing wave slope. This is because our data set are surface foam produced by shallow water breaking waves.

Figure 2.10 depicts the relationship between bubble decay times and some wave characteristics. The decay time τ_1 is larger than τ_2 except Runs 35 and 40 as shown in figure 2.10 because the surface foam areas from both domains are comparable for Runs 35 and 40. The decay time decreases whith the increasing of wave slope at the breaking point. On the other hand, the surface foam decay time increases with the increasing breaking wave height and Iribarren number (ξ_b). This implies that the decay time depends on the Iribarren number (ξ_b) for shallow water breaking waves, but decay time highly relates with the wave slope for whitcapping (Callaghan et al., 2013).

The correlation between τ and A', where A' is the surface foam area with offset 1 s since the wave crest is shown in figure 2.11. There are some variabilities of the surface foam area around wave crests, hence we consider the area after 1 s. This finding indicates that the decay time relates with the maximum surface foam area and also agrees with Callaghan et al. (2012) and Callaghan et al. (2013) (focus on whitecapping).

Additionally, there is a sensitivity of the threshold value as shown in figure 2.12. We analyzed the decay time from three different threshold by varying the standard

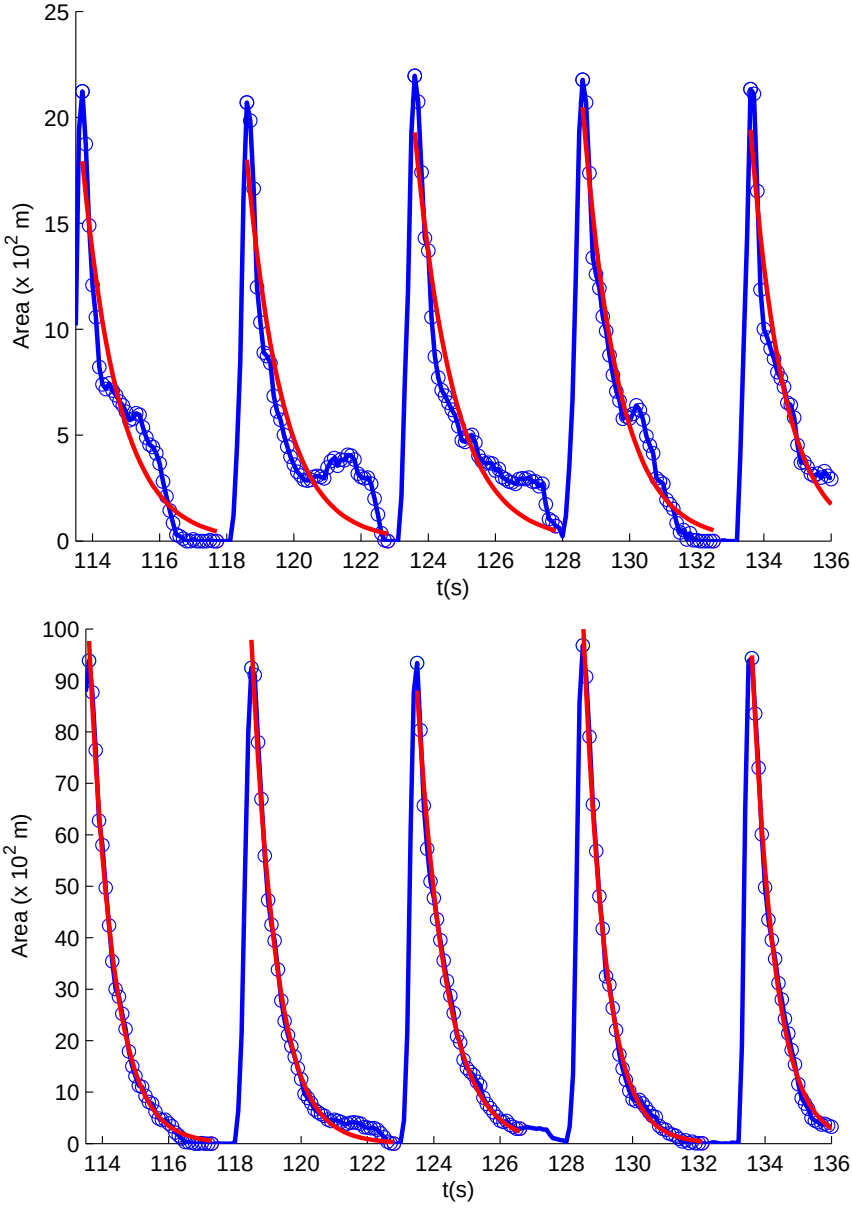

FIGURE 2.7: Runs 37: Time series of area evolution of 5 individual waves (blue line and blue dots). At the beginning (wave crest) of each wave shows the maximum of area and then decay in time. The red lines are fitted exponential decay curves with diffrent decay times (τ). (Top) Area from domain $D1$ (Bottom) Area from domain $D2$

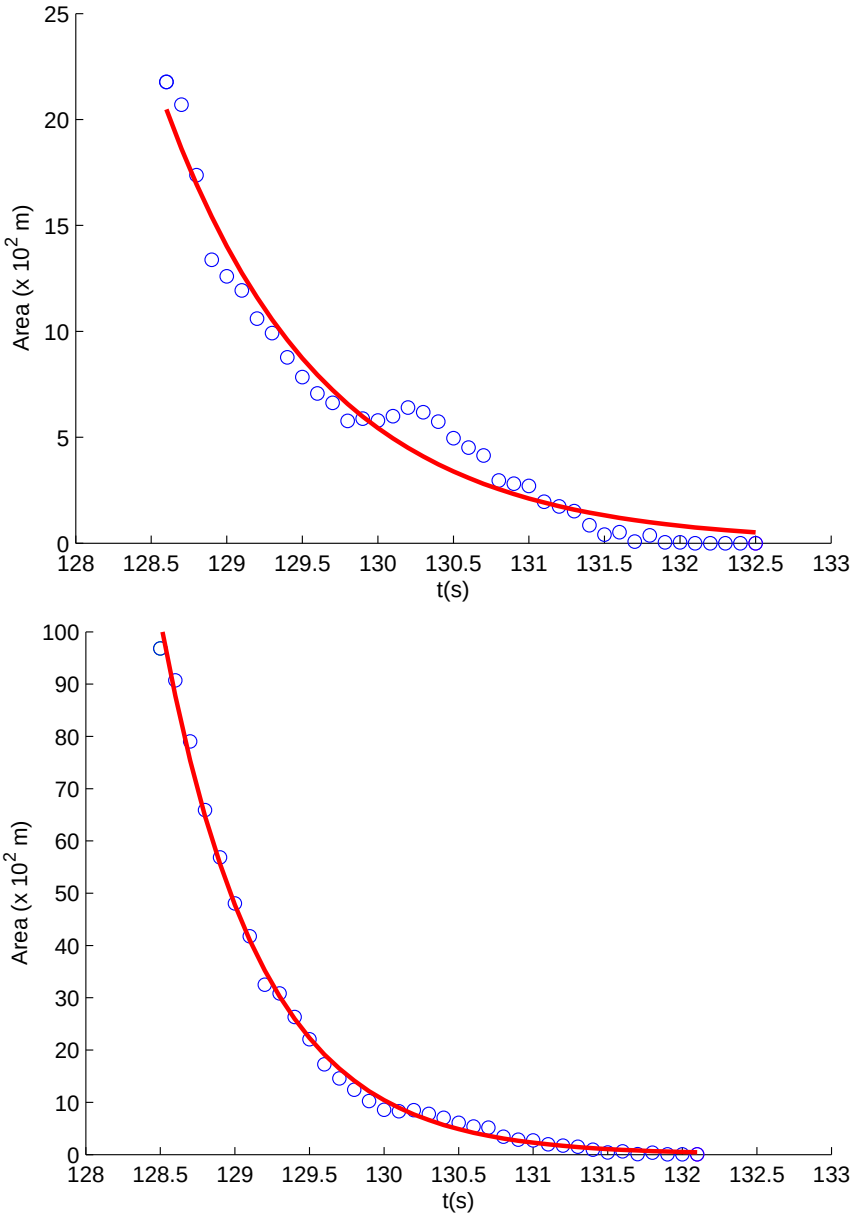

FIGURE 2.8: Runs 37: Time series of area evolution (blue dots) of 1 individual wave from two domains and fitted exponential decay curves wtih decay time (Top): $D1$ τ = 1.06 and (Bottom): $D2$ τ = 0.66.

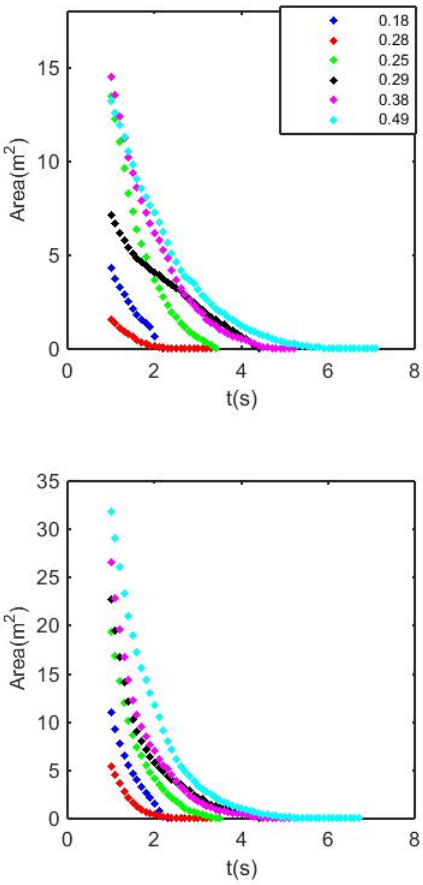

FIGURE 2.9: Temporal evolution of surface foam area. (top) from domain ($D1$) (lower) from domain ($D2$). Different colors corrrespond to different ξ_b

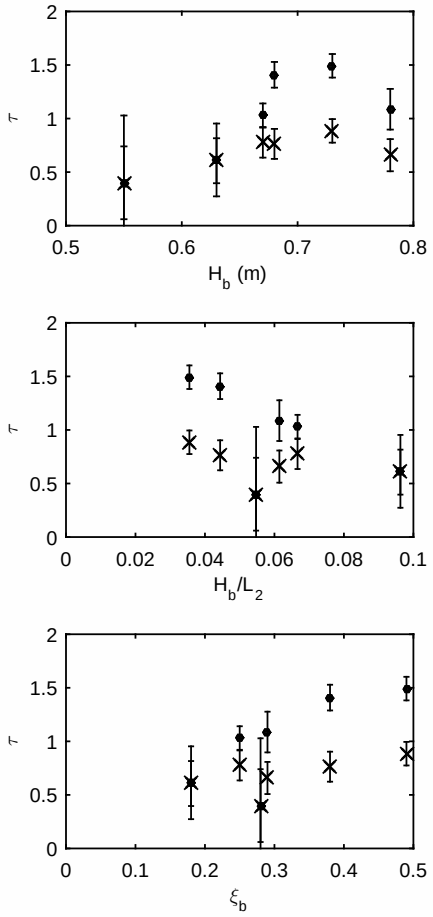

FIGURE 2.10: Scatterplots of bubble decay time and wave characteristics. (top) Breaking wave height (H_b) (middle) wave slope (H_b/L_2) (bottom) Iribarren number (ξ_b)

TABLE 2.2: Bubble decay time (τ_1, τ_2) from the intensity timestack from bubble area from domain $D1$, $D2$

Run	τ_1	std(τ_1)	τ_2	std(τ_2)	ξ_b	H_b L_2
35	0.61	0.34	0.61	0.21	0.18	0.09
40	0.39	0.63	0.40	0.34	0.28	0.05
36	1.03	0.11	0.77	0.15	0.25	0.07
37	1.09	0.19	0.66	0.15	0.29	0.06
38	1.41	0.12	0.76	0.14	0.38	0.04
33	1.49	0.11	0.89	0.11	0.49	0.03

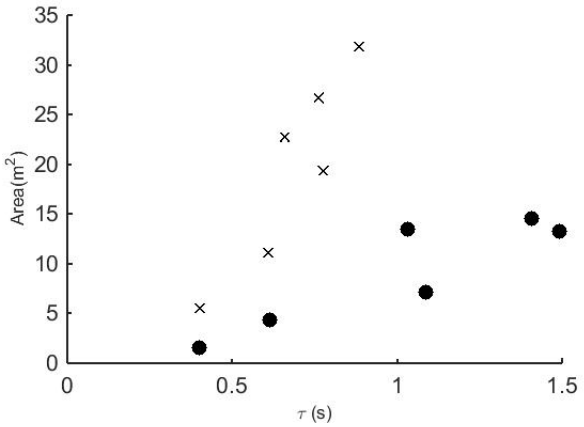

FIGURE 2.11: A scatterplot of surface foam decay time and maximum surface foam has an offset of 1 s from wave crest from domain $(D1, D2)$. We use the same symbols with figure 2.10

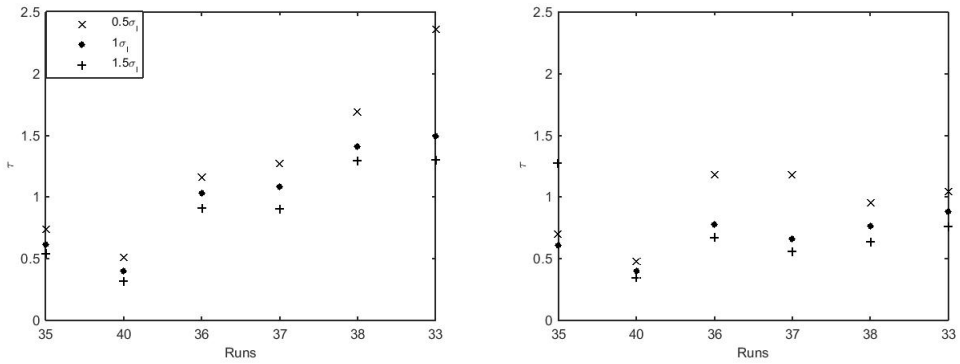

FIGURE 2.12: Comparison of τ from 3 different thresholds: $\overline{I} + 0.5\sigma_I$, $\overline{I} + \sigma_I$, and $\overline{I} + 1.5\sigma_I$, (left) domain $D1$ (right) domain $D2$

deviation of the intensity which are $\overline{I} + 0.5\sigma_I$, $\overline{I} + \sigma_I$, and $\overline{I}1.5\sigma_I$ The decay time is smaller with the increasing threshold. However, the decay times from all thresholds are in the same trends.

2.2.3 Surface foam length scales

Time series of surface foam length scales (λ_2 and $\lambda_1 0$) for Runs 37 comparison with the normalized intensity is shown in figure 2.13. At times, we are not interested in the length scales around wave crests, therefore the length scales around wave crests are defined to be zero as seen in figure 2.13(lower). The surface foam length scales of each run are shown in Table 2.3. The length scales (λ_2) are close to the length scale (λ_{10}) for all runs. This finding indicates that there is no dominant length scales of each run.

Figure 2.14 shows the relationship between λ_2, λ_{10}, and λ_{model} from Yeh and Mok (1990) shown in Table 2.3. Both discrete length scales (λ_2, λ_{10}) are close to λ_{model} except Runs 37. The discrete length scales compare favorably with model of Yeh and Mok (1990). This result demonstates that the discrete length scales from the laboratory experiment are physically reasonable.

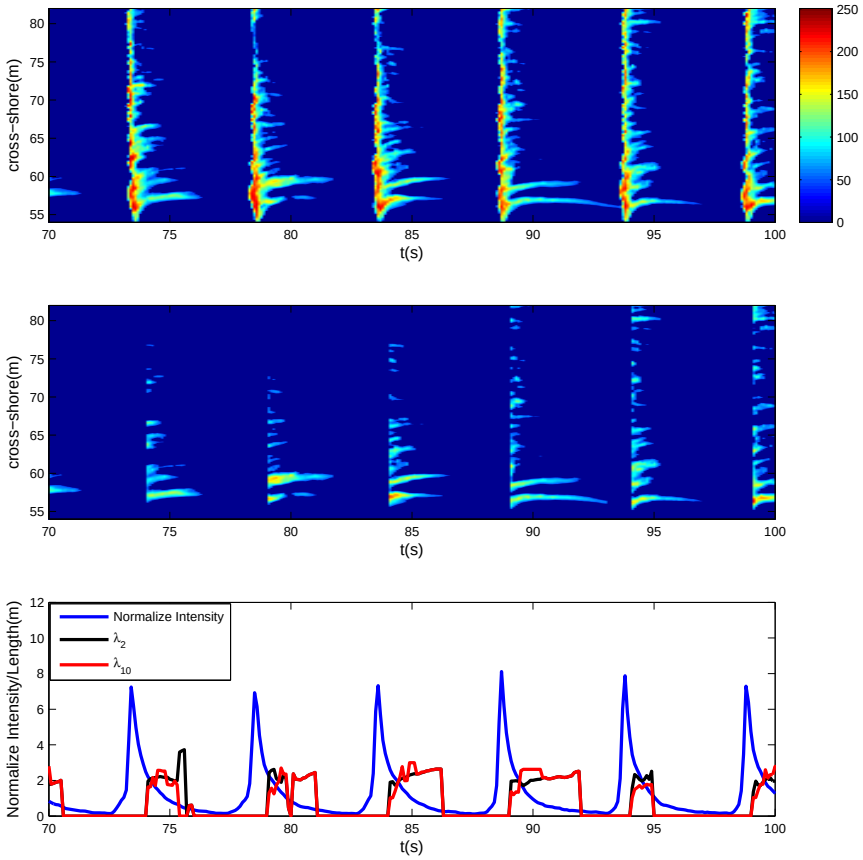

FIGURE 2.13: Portion of data (Runs 37) from t =70-100 s: (top) The intensity timestack (middle) The time stack of the smoothed with running average (2.5 m window), zero-upcrossing of the threshold ($\overline{I} + \sigma_I$), and setting zero length scales around wave crest regions intensity (lower) Time variation of length scales (λ_2: lengthscale between 2 highest peaks) and (λ_{10}: mean length scales of 10 events overlay with the normalized the mean intensity

TABLE 2.3: Bubble length scales from the experiment, prediction from Yeh and Mok (1990), change in energy flux at G3 ang G4, and change in energy flux at G3 ang G6. Unit of energy flux is $kg * m/s^3$

Run	λ_2 (m)	std (λ_2)	$\lambda_{10}(m)$	std (λ_{10})	$\lambda_{model}(m)$	$Ef_{G3,G4}$	$Ef_{G3,G6}$
35	1.62	0.64	1.54	0.57	-	1023	1282
40	1.96	1.18	2.02	1.09	-	-	-
36	1.69	0.86	1.70	0.76	1.77	919	959
37	1.91	0.72	1.92	0.58	1.05	1343	1634
38	1.60	0.80	1.76	0.76	1.66	595	850
33	1.75	0.87	1.81	0.78	1.67	1087	1538

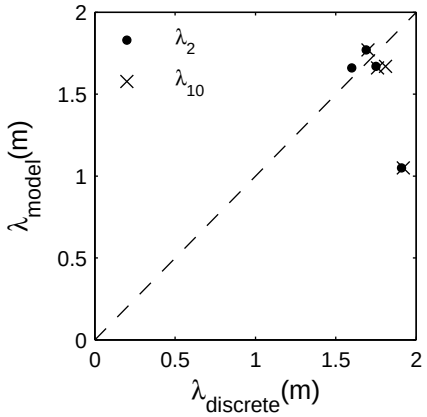

FIGURE 2.14: The relationship between the discrete length scales (λ_2, λ_{10}) and the calculated length scales (λ_{model}). The dashed black line is a 1:1 relationship.

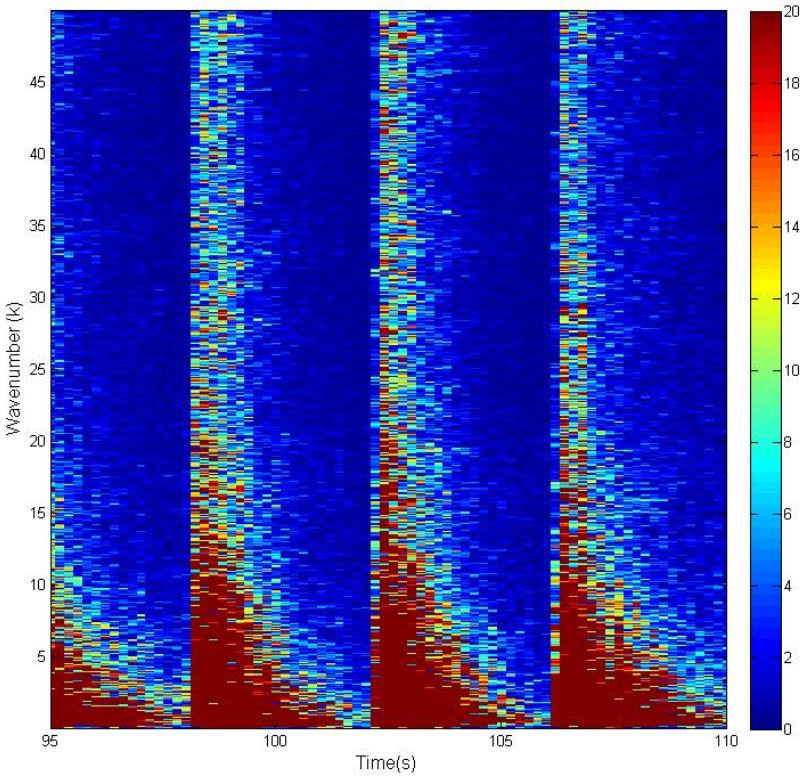

FIGURE 2.15: Example of PSD time stack image from Run36

Next, the length scales were determined by using spectrum analysis. The undirectional spectrum $S(k)$ measures the distribution of wave energy in wavenumber, k, (or frequency, f). In this study, we choose the wave spectrum in term of wavenumber (k) spectrum. Figure 2.15 shows some example of time stack image of PSD (Runs 36). It shows the high energy around the low wavenumber region and it decreases toward high wavenumber for all waves.

According to eq.(2.9) and eq.(2.10) for calculating the spectral bandwidth parameter, both parameters clarify that these data consistently generate the wide spectra for all runs as shown in Table 2.4. The larger value of ϵ and ν associates with the wide spectra. This calculation implies that the energy is broadly distributed among

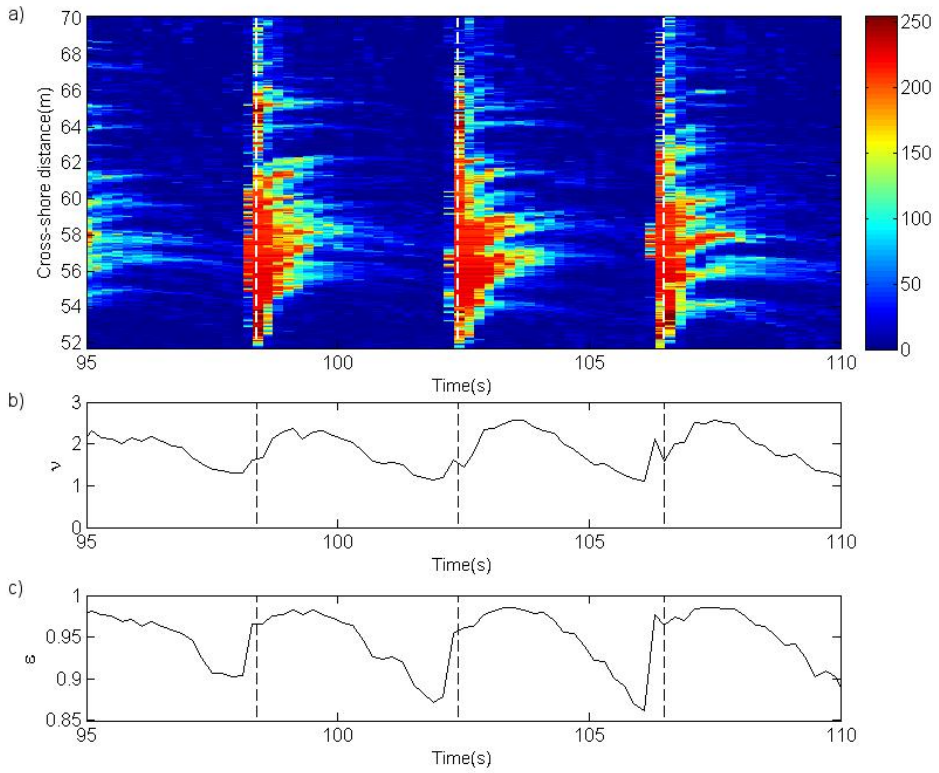

FIGURE 2.16: The variation of data from $t = 95.0 - 110.0\,s$ (a) time stack $I(x,t)$ (b) time series of spectral bandwidth (ν) (c) time series of spectral width (ϵ)

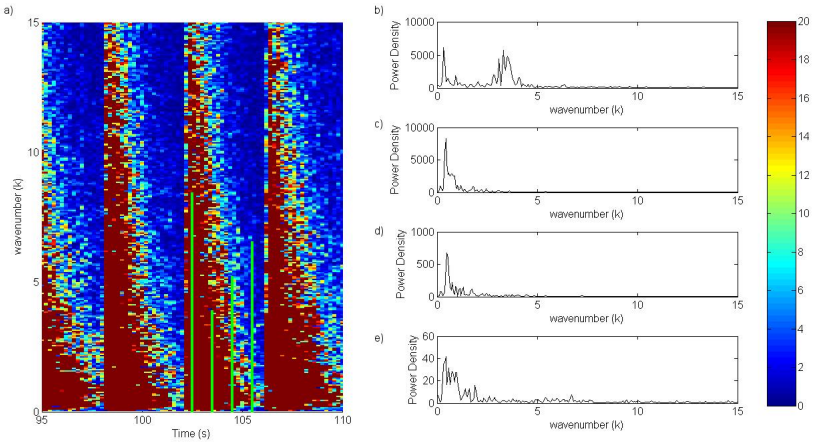

FIGURE 2.17: The spectral density and its mean wavenumber (k_{mean}) at time t = $102.5, 103.5, 104.5, and 105.5s$. k_{mean} is 17.39, 6.68, 7.43, 14.36, and 18.48 m^{-1})

many wavenumbers. ϵ and ν are high magnitude during the vigorous stage and low magnitude when bubble tails disappear as shown in figure 2.16b and figure 2.16c. In details, the spectral bandwidth parameter (ϵ) has mean value in the range of 0.902-0.958 ($\epsilon \rightarrow 1$: wide spectra);therefore it tends to a Gaussian distribution. For the ocean waves and of ship motion, the value of (ϵ) raning form 0.20 to 0.68 (Cartwright and Longuet-Higgins, 1956). Figure 2.16 expresses an example of the distribution of ϵ and ν for Runs 36. ϵ is about 0.95 at t = $102.4s$ (breaking stage), next gradually increases to the maximum peak (ϵ is about 0.98) at t = $103.4s$, then dramatically declines to the lowest point (ϵ is about 0.853), and finally ramps up again right before the next breaking wave. For the spectrum bandwidth parameter (ν), its magnitude has a mean value in range of 1.79-2.16.

And then, the mean wave length and wavenumber was calculated by eq.(2.12) and eq.(2.13), respectively. The mean wavenumber does not depend on the magnitude of the spectral density, but it measures how wide of the spectral density for each time series. For instance, the mean wavenumber at 105.5 seconds is broader than the mean

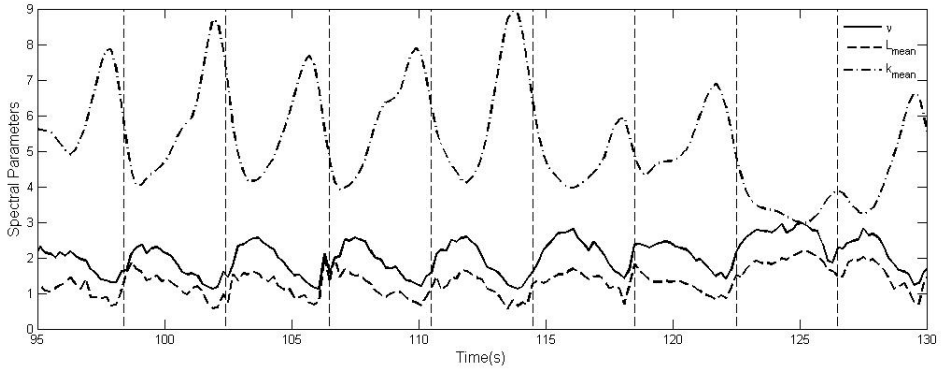

FIGURE 2.18: The variation of ν, λ_{mean}, k_{mean}, the vertical line represent the time when wave is breaking

TABLE 2.4: Spectral parameter: ϵ, ν, k_{mean}, λ_{mean}

	ϵ			ν			k_{mean}			
Run	min	max	mean	min	max	mean	min	max	mean	λ_{mean}
35	0.88	0.99	0.93	1.21	2.99	2.10	4.73	5.59	4.98	1.26
40	0.81	0.99	0.90	0.88	2.70	1.79	6.25	10.43	8.34	0.75
36	0.93	0.98	0.95	1.60	2.43	2.01	6.36	4.27	5.32	1.18
37	0.86	0.99	0.92	1.10	3.22	2.16	3.54	5.10	4.32	1.45
38	0.83	0.99	0.91	0.96	3.27	2.12	7.24	4.38	5.81	1.08
33	0.81	0.99	0.90	0.90	3.01	1.95	4.02	9.98	7.00	0.89

wavenumber at 102.5 seconds as shown in figure 2.17. For the mean length, it is found that its magnitude varies with wave conditions range from 0.75-1.45 m and is related to the waveheight. Additionally, the corresponding wavenumber from power density function vary in the range of 4.33 - 8.34 m^{-1}. Noted that the bubble wavenumbers are mostly higher than the wavenumbers calculated from the linear wave theory between 0.04L-0.19L (where L is wave length). In other words, the bubble plume length does not exceed the progressive wavelength. In order to study the variation of k_{mean} and spectral width, the scatter plot is presented (figure 2.18) and found that k_{mean} were associated with the opposite spectral width.

2.3 Conclusions

We analyzed the optical intensity signal from individual breaking waves over a fixed bed bar/trough bathymetry. These surface foams were generated by freshwater, shallow water breaking waves, and comparable scales with the field. The bubble plumes form, grow, and decay less than about a wave period. The range of decay time varies from 0.39-1.49 seconds and 0.40-0.88 seconds from domain D_1 and D_2, respectively. The decay time (τ) is similar to whitecap (deep water breaking) but freshwater bubble decay times are faster. Furthermore, the decay time still correlates with increasing ξ_b because this surface foam produced by shallow water breaking waves, and the maximum foam area also relates with ξ_b.

For the length scales, we analyzed the length scales by three different methods which are discrete, model, and spectral analysis. The length scales are in the range between 1.60-1.96 m, and 1.54-2.02 m for λ_2 and $\lambda_1 0$, respectively. Both length scales are similar. For spectral analysis, these data display the wide band spectra and the event spacing wavenumbers are less than the wavenumber calculated from the linear wave theory for all runs. From the Probability Density Functions (PDFs), the bubble

plume length veries between 0.04L-0.19L. For comparison, the length scale from these data compares favorably with model of Yeh and Mok (1990). However, this model was proposed for uniform bores, nevertheless, there were incoming waves generated in the plume for this laboratory.

In the present work, we take a unique approach to analyzing bubble plumes. Also, we pioneer analyze the relationship between the Remotely sensed video intensity data of the individual breaking waves in a different regime from previous experiments (i.e. shallow water, freshwater, and scales) and surface foam. Consequently, it will be a useful data set for model/data comparison.

3. Wave-current Interaction Induced by Standing Long Wavevs in the Surf Zone

Jitraporn Phaksopa, Merrick C. Haller, and Tuba Özkan-Haller

Manuscript will be submitted to:

Journal of Fluid Mechanics

3.1 Introduction

Wave breaking is a natural process in the nearshore region. The breaking wave process generates turbulence, entrainment of air bubbles, and also transfers momentum from the surface into the water column. As waves approach the breaking point, then that energy is dissipated during the wave breaking process. Wave breaking is the principal driving mechanism for nearshore currents, mean water level changes, low frequency oscillatory motions within the surf zone, and sediment transports. Wave breaking is variant in both time and spatial scale. Therefore, wave breaking in the surfzone is of great importance to the study of nearshore hydrodynamics. However, wave-current interaction has also affected on the wavenumber and phase speed in the coastal and nearshore region.

Some previous studies suggested that wave-current interaction should be considered in the study of the nearshore hydrodynamic processes such as Tolman (1990) found that the unsteady depth and current should account for the wave propagation in hte North Sea. Jones (2000) investigated the interaction between tides and waves on the wave refraction at the coast of south-west Wales, U.K. through numerical model. However, the wave-current interaction theory has not been validated by comparison with observation data in various natural situations, such as tidal inlet and nearshore standing long waves (i.e. surfbeat).

Unsteady current can caused by many reasons such as tide, and low frequency motion. The existence of low frequency motion is significant to nearshore process because it modulates in the water surface fluctuations or water depth especially harbors and large-vessel mooring system. Hence, the low frequency wave is one of the keys to design the coastal structure and the evolution of coastal morphology. Surf beat, which is one type of low frequency wave, was originally found and named by Munk (1949). This low frequency wave has a period within the order of minutes. Tucker (1950)

found that the cross-correlation between the low frequency wave and the incoming wave found that there was a negative peak at the lag approximately corresponding to the time required for the short wave to travel to the shore and the low frequency waves back to the breaking point. Also, the phase relationship between the different wave systems (incident bound long wave and the outgoing breakpoint forced wave) are important for the response of long wave and the short wave. There are a numbers of field observations, laboratory experiments, and numerical models proposed to explain the mechanism of low frequency wave motion in nearshore [Longuet-Higgins and Stewart (1962); Symonds et al. (1982); Janssen et al. (2003)]. However, the mechanism of the generation of the low frequency wave is still unclear. One, the mechanism is breakpoint forced long waves (BFLW) and the other is the release of bound long waves (BLW). For the first mechanism, it is assumed that the incident bound long waves are released during the incoming short wave breaking, then travel toward the shore as the free wave, and consequently reflect back at the shoreline producing the standing wave in the inner surf zone (Symonds et al., 1982; Baldock et al., 2000). Symonds et al. (1982) proposed two dimensional model for low frequency wave generated by time varying breaking point. This model allowed the energy radiated both shoreward and seaward. They found that the response of low frequency wave relatively depended on the incident wave field. Another possible mechanism stated that the bound long wave would be released when the short waves are in the shallow water (Longuet-Higgins and Stewart, 1962; Baldock, 2012). As Longuet-Higgins and Stewart (1962) suggested the forced long wave dissipated toward the shoreline. This dissipation is not caused by the friction, but it might be caused by the non-linear interaction which transferred energy back to short wave. This assumption is consistent with the laboratory experiment [Baldock and O'Hare (2004); Van Dongeren et al. (2007)] and field data (Henderson and Bowen, 2002).

Baldock (2012) proposed a surf beat similarity parameter ($\xi_{surfbeat}$) to dis-

tinguish between different long wave mechanism in the surf zone. This parameter represent that the response of long wave depends on two parameters which are the normalized beach slope and the wave steepness. If $\xi_{surfbeat}$ is large, the breakpoint forcing is expected to be dominant and if $\xi_{surfbeat}$ is small, the bound wave release mechanism should dominate in the surf zone. Subsequently, Contardo and Symonds (2013) analyzed the field observation data of sea surface elevation during swell and storm. They found that long wave mechanism agreed with the surfbeat similarity parameter ($\xi_{surfbeat}$). Mostly, the previous results have studied the response and mechanism of long wave in the open boundary at the off-shore. However, the enclosed boundary i.e. basin, lake, and harbour also experience the resonance in the low wave or seiching.

We analyzed the laboratory data of Catálan and Haller (2008). These data composed of the video observation of monochromatic waves over a fixed barred beach. Essentially, it clearly showed the occurrence of basin seiching or low frequency waves during the experiments as shown in Figure 3.1. Figure 3.1 showed an example of time stack intensity image from the experiment in the Large Wave Flume(LWF) in 2005. It captured the evolution of the wave roller over a fixed bed arranged in a bar-trough morphology. Bright regions represent the moving path or trajectory coincides with bubble plume of each wave. It shows a maximum intensity at the wave crest. The irregularity in bubble tails or bubble remnants pattern periodically occurred although may not be repeated at exactly the same position from one wave to the next wave. The oscillation of breaking point strongly corresponded to the basin seiching wave observed during the experiments. Moreover, Haller and Özkan-Haller (2007) found that the existing of low-frequency standing waves during in this experiment modulated in the wave frequency/wavenumber and wave height. Motivated by these results, seiching basin or low frequency waves should be accounted in nearshore hydrodynamics study. The wave-current interaction is important for the understanding of the ocean

such as the propagation of incoming waves through the tidal inlet, or the interactions of the incoming wave and nearshore standing long wave. There are various reasons to cause the unsteady current and total water depth fluctuation such as tide, surf beat, or seiching.

Several recent numerical model studies suggested that such a feedback mechanism is significant for the dynamics of nearshore hydrodynamics such as rip current [Haas et al. (1999) and Yu and Slinn (2003)], and longshore current instabilities (Özkan-Haller and Li, 2003) but the effect on standing seiching wave is unknown. Recently, the feedback between the wave field and the generated current have been reported by two different approaches including of fully coupling wave-current interaction based on Boussinesq equations model and semi-wave-current interaction model. The first approach, for example, Chen et al. (1999) utilized the extend Boussinesq equations to study rip current system from the experiments (Haller et al., 1997). This approach resolves the wave motion and the generated current simultaneously. Hence, this approach cannot emphasize the results with and without the wave-current interaction. The others approach, the coupling between wave and current appears through the radiation stress gradient term due to waves (taken as a forcing in the momentum equation) and through wave-current interaction terms. Nevertheless, this approach can not be justified in case of strong current.

This paper is aimed to understanding of the physical processes involved in the wave-current interaction as it affects on the subsequent of the kinematic and dynamics of the incident wave field and the low frequency wave in the closed basin seiching containing a plane beach. The hydrodynamic of this study is based on the depth-and time-averaged Navier Stokes equations flow equations coupling with the simplified wave equation proposed by Özkan-Haller and Li (2003) described in section 2. This paper is limit to the study of an idealized system which isolates the main physical

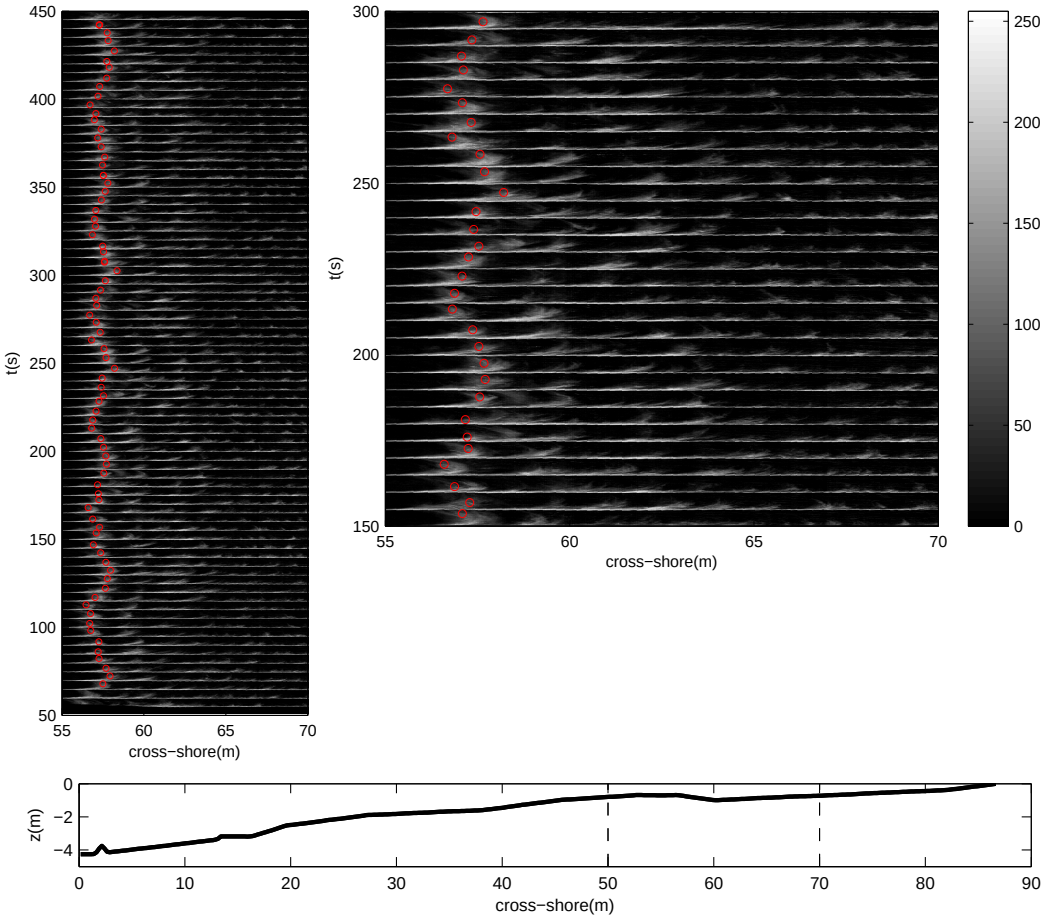

FIGURE 3.1: (top) Example of the first breaking point of each wave on time stack image of the intensity data from RUN37 and this breaking point represents basin seiching with period 56.1 s and (bottom) vertical elevation of the fixed bed in the experiment

features, therefore we will carefully discuss the results with out the comparison with observation data which is beyond the scope of this study. The results from the numerical experiment with exclude and include the wave-current interaction to compare the significant difference on the low frequency wave response and the incident wave field modulation, also the breakpoint initiation are discussed in section 3. Then, these responses in the access of the wave-current interaction will conduct to identify the long wave mechanism. Discussion and conclusion are presented in section 4 and section5.

3.2 Methodology

3.2.1 Flow Equations

The vertically integrated time-averaged Navier Stokes equations dictate the time-varying behavior of water surface elevation and flow velocities. These equations include the effect of the unsteady from the radiation stress gradient caused by the incident short wave. The cross-shore continuity equation for one dimension is given by

$$\frac{\partial \eta}{\partial t} + \frac{\partial}{\partial x}[(h+\eta)u] = 0 \tag{3.1}$$

where η is the total surface elevation. The cross-shore momentum equation is

$$\frac{\partial u}{\partial t} + u\frac{\partial u}{\partial x} = -F_x - g\frac{\partial \eta}{\partial x} + \tau_x - \tau_{bx} \tag{3.2}$$

where the first term of the RHS represents the wave-induced forcing, the second term is the cross-shore pressure gradient, the third term is the turbulent lateral mixing and τ_{bx} is the bottom shear stress. This term represents the combined short-wave and (Eulerian) current bottom shear stress in the crossshore direction. It is neglected in this study because the magnitude is small from the previous study from Dally and Brown (1995). The wave-induced forcing (F_x) is defined as

$$F_x = \frac{1}{\rho d}\Big[\frac{\partial S_{xx}}{\partial x}\Big]; \tag{3.3}$$

where S_{ij} represent the wave radiation stress tensor, and the subscripts refer to the direction in which the forces act, and $d = h+\eta$ is the total water depth. In this study, we consider only x-direction. The radiation stress is computed by using the linear wave theory is given by

$$S_{xx} = E\left(\frac{2kh}{sinh\,2kh} - \frac{1}{2}\right) \tag{3.4}$$

where E is the wave energy ($E = (1/8)\rho g H^2$) and k is the wavenumber.

The turbulent lateral mixing term (τ_x) is given below:

$$\tau_x = \nu_t \frac{\partial^2}{\partial x^2} u \tag{3.5}$$

here, the parameter ν_t represents the turbulent eddy viscosity coefficient which is assumed to be related with wave breaking (Battjes, 1975) but this horizontal mixing term is not the main concern for this study so that we parameterize the magnitude of this coefficient getting the correct order of magnitude. Therefore, the turbulent eddy viscosity coefficient is reduced into the following equation:

$$\nu_t = Md\left(\frac{D}{\rho}\right)^{1/3} \tag{3.6}$$

where M is the constant mixing coefficient. This horizontal mixing term is not the main concern for this study so that we parameterize the magnitude of this coefficient getting the correct order of magnitude. Therefore, we will discuss the simulations with using the turbulent eddy viscosity coefficient reduced into the following equation:

$$\nu_t = \beta d \tag{3.7}$$

where β is the parameterization number of this term $M(\frac{D}{\rho})^{1/3}$. We tested β in the range of 0-1.0. Then, we chose β = 0.5 for this study because this number is in the correct order of magnitude.

3.2.2 Wave Model

Here, we focus on the feedback between the incident wave field and the unsteady current. The forcing by the incident wave field are included in the flow equations in the momentum equation 3.2. Then we need to account for the effect of current on the incident wave field. In this study, we consider the monochronomatic wave (no wave groups) propagating over the unsteady current $u(x,t)$ medium and this current represents a low frequency wave current. This situation is current varying slowly in spatial and temporal scale and the total water depth also varies slowly. Therefore, the wave energy should varies in time as well. The predicted wave energy variaion are

analyzed by using the time dependent wave action balance equation:

$$\frac{\partial}{\partial t}(\frac{E}{\sigma_r}) + \frac{\partial}{\partial x}((U + C_{gr})\frac{E}{\sigma_r}) = \frac{D}{\sigma_r} \tag{3.8}$$

where E/σ_r is the wave action density in terms of energy spectrum and intrinsic frequency, σ_r is the intrinsic frequency and is equal to $(\omega - kU)$, ω is the absolute frequency and k is the wave number. C_{gr} is defined as the relative group velocity which is the speed of wave energy propagation in a frame moving with the local current velocity.

$$C_{gr} = \frac{1}{2}(1 + \frac{2kd}{sinh\ 2kd})\frac{\omega - kU}{k} \tag{3.9}$$

The presence of the unsteady current and the total water surface elevation, the kinematics of the incident wave field are also changed in time especially the absolute wave frequency (Haller and Özkan-Haller, 2007). Hence, the dispersion relation for the incident gravity wave propagating over the unsteady medium is given by:

$$(\omega - kU)^2 = gktanh(kd) \tag{3.10}$$

Continuing from 3.10, we utilize the time-varying wavenumber(k) by using the conservation of wave equations in cross-shore direction as described below:

$$\frac{\partial k}{\partial t} = -\frac{\partial \omega}{\partial x} \tag{3.11}$$

And then differentiating 3.10 with respect to time, this gives the governing equation as follow

$$\frac{\partial}{\partial t}\omega + (U + C_{gr})\frac{\partial}{\partial x}\omega = k\frac{\partial}{\partial t}U + q\frac{\partial}{\partial t}\eta - p\frac{\partial}{\partial t}\eta \tag{3.12}$$

The parameters p and q are defined as

$$q = \frac{\omega k}{sinh\ 2kd} \qquad and \qquad p = \frac{k^2 U}{sinh\ 2kd} \tag{3.13}$$

The parameter D represents the wave breaking dissipation. In general, waves start breaking when the wave front become too steep i.e. the ratio of height and water depth is over the given value named γ. There are several formulas to calculate the

wave breaking dissipation parameter i.e Battjes and Janssen (1978), Thornton and Guza (1983), and Roelvink (1993). This parameter essentially described how fast that the energy is dissipated and transferred to the low frequency wave. In this study, the time varying dissipation parameter is calculated from the dissipation function for the random wave from Roelvink (1993) and Reniers et al. (2004), as the following equation

$$D = P_b D_b \tag{3.14}$$

where P_b is the probability that wave is breaking and D_b is the expected dissipation value in a breaking wave. P_b and D_b are given below

$$P_b = \left[1 - exp\left[-\left(\frac{E}{\gamma^2 E_{ref}}\right)^{\frac{n}{2}}\right]\right] \tag{3.15}$$

where E_{ref} is $(1/8)\rho g d^2$ and d is the total water depth.

$$D_b = 2\alpha f_p E \tag{3.16}$$

where f_p is the the peak frequency of the short wave. The probability will go towards 1 when the wave energy is increasing or water depth is decreasing.

$$D = \left[1 - exp\left[-\left(\frac{E}{\gamma^2 E_{ref}}\right)^{\frac{n}{2}}\right]\right] 2\alpha f_p E \tag{3.17}$$

where γ is the ratio between the waveheight and water depth. In this study, we use $\gamma = 0.98,\ n = 10$ and $\alpha = 0.5$

3.2.3 Model procedure and application

The simulations are carried out the unsteady current from the low frequency wave in the closed basin length ($L = 8\,m$) containing the planar beach with x point onshore direction. The given water depth is $h = h_0 - mx$, where m is the beach slope. These simulations cover for two slope regimes which are mild ($m = 1/50$) and steep ($m = 1/10$). The domain is bounded with the vertical wall at $x = 0$ and $x = L$ with

the boundary condition as described below:

Boundary conditions

From the above equation 3.1 and 3.2, we need a boundary condition at the two ends of the tank. We use the fixed boundary condition which is stating that the wave must be fully reflected at the both sides of the tank at $x = 0$ and $x = L$. Boundary conditions were zero mass flux through the boundaries hence:

$$\frac{\partial \eta}{\partial x} = 0 \quad and\ u = 0 \quad at\ x = 0\ and\ x = L \tag{3.18}$$

The offshore boundary waveheight and wave period conditions for two cases with 4 subcases for each case considered here, are listed in Table 3.1.

The governing nonlinear equations for solving the low frequency wave with wave-current interaction with the boundary conditions (3.18) are solved by means of an explicit finite difference scheme which is the second order central differental scheme in space, and the second-order AdamsBashforth in time. This method is used to update time-dependent variables in the governing equations at each mesh point in turn at each time step. The wave action balance is solved by applying the first-order Euler method in time and space. The numerical parameters $(\Delta x, \Delta t)$ are chosen under the critical criteria (The Courant number) which are $\Delta x = 0.05\,m$ and $\Delta t = 0.02\,s$. For the numerical instability, the required time step $(\Delta t = 0.02\,s)$ is small comparing with the physical current and wave in the nature. Initially, we set the basin to rest at the beginning, so that the current starts from rest in each experiment. The monochromatic incident wave is started from rest and then ramped up about 5 wave periods to the steady state solution. The ramping up period is short to prevent any instabilities. Simultaneously, the perturbation from the incident wave field is inserted to the velocity field from the beginning too. At the shoreline boundary where the total water depth is zero, so the governing equations are singular. Therefore, the wavenumber is an infinite. To avoid the infinite wavenumber, the small water depth (about 0.06 m)

TABLE 3.1: The experimental conditions for all cases: beach slope (m), wave period ($T(s)$), deep water wave height (H_0), deep water wavelength (L_0), deep water steepness ($\frac{H_0}{L_0}$), surf similarity (ξ), normalized bed slope (β), surfbeat similarity ($\xi_{surfbeat}$)

CASE	m	$T(s)$	$H_0(m)$	L_0	H_0/L_0	ξ	β	$\xi_{surfbeat}$
1A	1/50	2.0	0.08	6.24	0.013	0.177	0.33	0.037
1B			0.10	6.24	0.016	0.158	0.29	0.037
1C			0.12	6.24	0.019	0.144	0.26	0.036
1D			0.14	6.24	0.022	0.134	0.25	0.038
2A	1/10	1.0	0.10	1.56	0.064	0.395	0.93	0.235
2B			0.15	1.56	0.096	0.322	0.86	0.266
2C			0.20	1.56	0.128	0.279	0.75	0.267
2D			0.22	1.56	0.141	0.266	0.68	0.254

is defined at this location.

In this study, we perform the model for two different approaches, the first ignores wave-current interaction (1-way coupling) and the second includes wave-current interaction (2-way coupling). We solve the full system of equations given by equations (3.1, 3.2, 3.8, 3.10) which are totally five unknowns (η, u, E, k, ω) in 2-way coupling approach. For 1-way coupling, we begin the simulation ignoring the wave-current interaction term in the wave action balance equation (3.8) and the dispersion relationsip equation (3.10), although still remaining the wave-induced forcing term in the momentum equation (3.2). This part is aimed to study the nature of wave height decay and the set-up induced by the incident wave field.

3.3 Results

In the experiments described below, the closed basin with the planar beach domain with $m = 1/50$ and $m = 1/10$ with the varying incident wave fields in period and waveheight as detailed in table 3.1 are simulated. The example of cross-shore domain is 8 m in length pointing shoreward. We begin the simulations with pure low frequency basin seiching in horizontal bottom and planar slope bottom. We initially carry out simulations for first mode of pure seiching (no forced wave) of different bottom profiles which are the horizontal bottom (constant depth $h = 1\,m$) and plane beach slope ($m = 1/50, 1/10$). For the horizontal bottom, the fluid in the tank is at rest ($u = 0\,m/s$) but displaced so that the free surface profile is a cosine wave in x-coordinate direction ($\eta_0 = Acos(\pi x/L)$). The initial amplitude ($A = 10^{-4}\,m$) is small comparable to the water depth. Considering this motion is frictionless, hence the pure seiching continues undamped forever (the energy is conserved). The resulting water surface elevation displays the nodal point at the center of the tank. The given seiching period from the simulations is same as the theoretical calculation ($T_s = 10.22\,s$). For sloping bottom, the initiated displacement is $\eta = -iAJ_0(2C\psi)$ where J_0 is the zeroth order of Bessel function and ψ is $\sqrt{1 - x/L}$. The shoreward currents are stronger than the seaward currents for both slopes compared with the horizontal bottom as shown in figure 3.2. The cross-shore current profiles do not have a perfect sinusoid shape comparing with the cross-shore current profiles in the horizontal bottom. Also, the nodal point are not located at the center of the tank, it slightly shift further shoreward when the beach slope is steeper. It should be noted here, there is the envelope modulation in η and u for the steep slope that it is not caused by the non-linearity of the hydrodynamic equations.

Next, we carry out simulations with the varying incident wave fields in the same domain while excluding and including wave-current interaction.

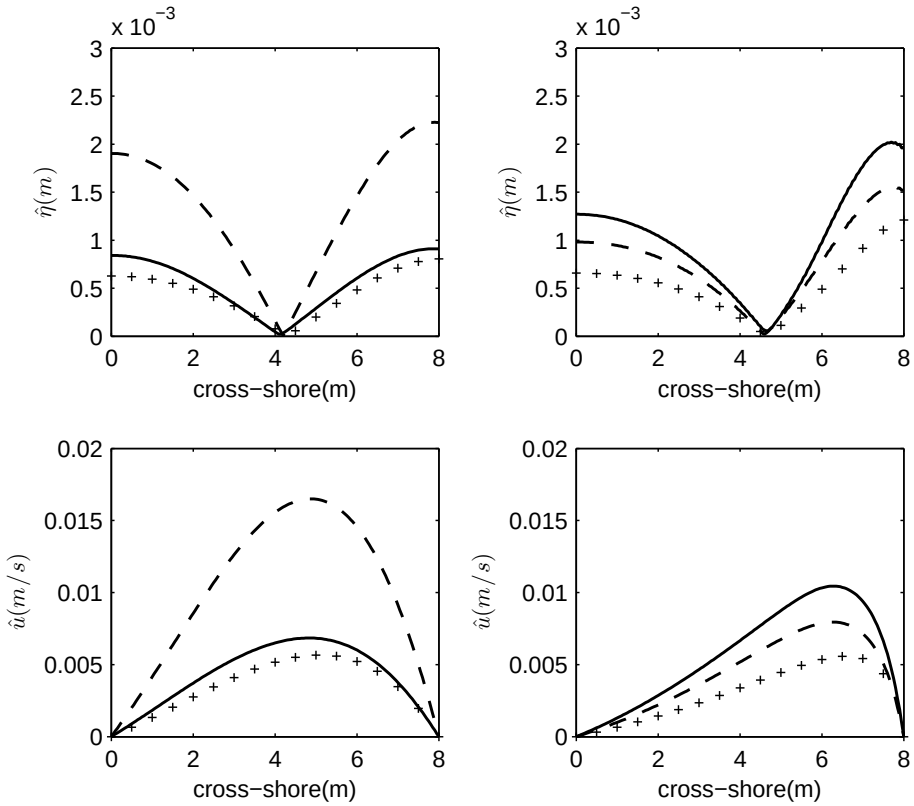

FIGURE 3.2: The examples of modal profiles of η and u at the seiching frequency for two beach slopes. (Right) m = 1/10: for $case2D$ (Left) (Right) m = 1/10: $case2D$. (-, - -, and + represents while excluding wave-current, including wave-current interaction, and pure seiching respectively). In case of pure seiching, the magnitude of both parameters are multiplied by 10.

3.3.1 Wave forced the low frequency wave motion

We focus on the response of the forced short wave on the unsteady current and also the impact of the unsteady current on the incident wave field. Hence, it is essential to first look at the case of the excluding wave-current interaction case (1-way coupling) using it as a basis for comparison with the including wave-current interaction case (2-way coupling). For 1-way coupling, we let the forced wave propagate shoreward over the plane beach, meanwhile the basin seiching is generated. The radiation stress from wave motion is added into the momentum equation (3.2) to compute η and u. For 2-way coupling, we let the forced wave propagate shoreward over the plane beach with the seiching basin. The radiation stress from wave motion is added into the momentum equation (3.2) to compute η and u, and then those computed data are iterated to compute the waveheight in the next time step. We utilize the closed tank 8 m in length on two different planar slope m = 1/50 and m = 1/10 with different offshore conditions shown in table 3.1 while including and excluding wave current interaction. We will analyze the temporal and spatial of the motion as described below.

3.3.1.1 The response of low frequency basin seiching

For mild slope (m = 1/50), the 250 second time series at two locations where are x_b and $0.75w_{surfzone}$ where x_b is the breaking point and $w_{surfzone}$ is the surf zone width of each parameter were figure 3.3 and figure 3.4. Figure 3.3 shows the variation of wave height H, absolute frequency ω, and wavenumber k when the wave-current interaction is included at two locations. At the first 100 s, the wave height fluctuates about $0.138 - 0.141\,m$ and then it damps out. Figure 3.4 shows the results for η, and u in 1-way and 2-way coupling simulations. While excluding wave-current interaction (figure 3.4(left), the surface elevation and current profiles oscillate with the averaged period which is 12.54 s (seiching period) and both are gradually declined by the advanced time. Noted for $case1D$, that there are two harmonics at both locations

and we will discuss about this in further section. When wave-current interaction is included (figure 3.4:right), the magnitude of the water surface elevation is essentially decreased by time. Also, the time series for both water surface elevation and current are no longer show the higher harmonic character. The time series of wavenumber and wave frequency are constant (ω = 3.1426 rad/s and k_1 = 2.2360, k_2 = 2.9449 rad/m) in the absence of wave-current interaction. The fluctuation of wavenumber and wave-frequency become time dependent and regular with a period of standing basin wave about 12.54 s and damp out with time as seen in figure 3.3. Both oscillations are large at the beginning and become smaller fluctuations at further times. Therefore, both oscillations are in response to the fluctuation in η. The oscillation of wavenumber and wavefrequency are highly correlated with η but with the phase shift.

Three hundred-seconds time series of each parameter for case2D are shown in figure 3.5 and figure 3.6. The representative time series were collected at two locations where proportional to the breaking point of each subcase (x = 5.30 and 7.30 m). The wave height is significantly increased and fluctuated with the period of seiching (about 8.42 s) as seen in figure 3.5. Figure 3.6(left) show the surface elevation and curent profiles in the absence of wave-current interaction. The responses in term of the amplitude in η and u are smaller by comparing with the milder slope (Case1) and both profiles are gradually decreased by time. When wave-current interaction is included (figure 3.6:Right), the water surface elevation and current are obviously amplified. Once again, the time series of wavenumber and wave frequency are constant as we expected (ω = 6.28 rad/s and k_1= 4.506, k_2= rad/m) but both parameters become time dependent and both are in the response of η when wave-current interaction is included. The variation of wavenumber and wave frequency are highly correlated with current signal but with phase shift, nevertheless both are 180 degree out of phase in η.

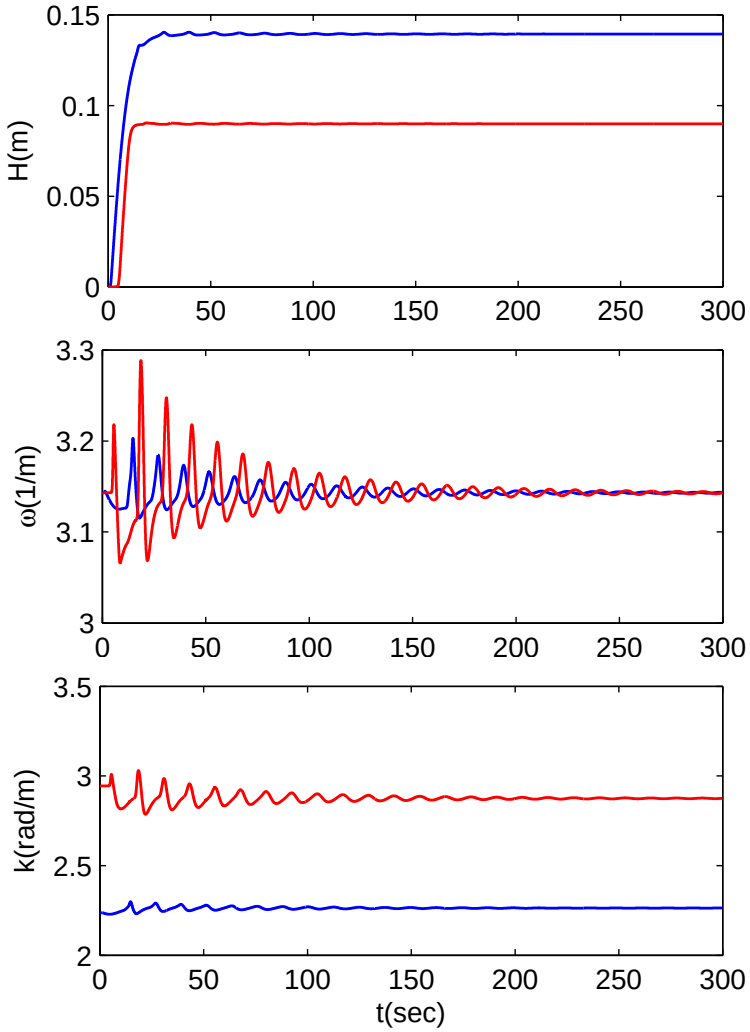

FIGURE 3.3: Time series for m=1/50 (Case1D) including wave-current interaction. Results for wave height(H), ω, and k at two locations related with breaking point at x=1.65 m (breaking point)-blue lines and 6.43 m (inner surf zone point)-red lines

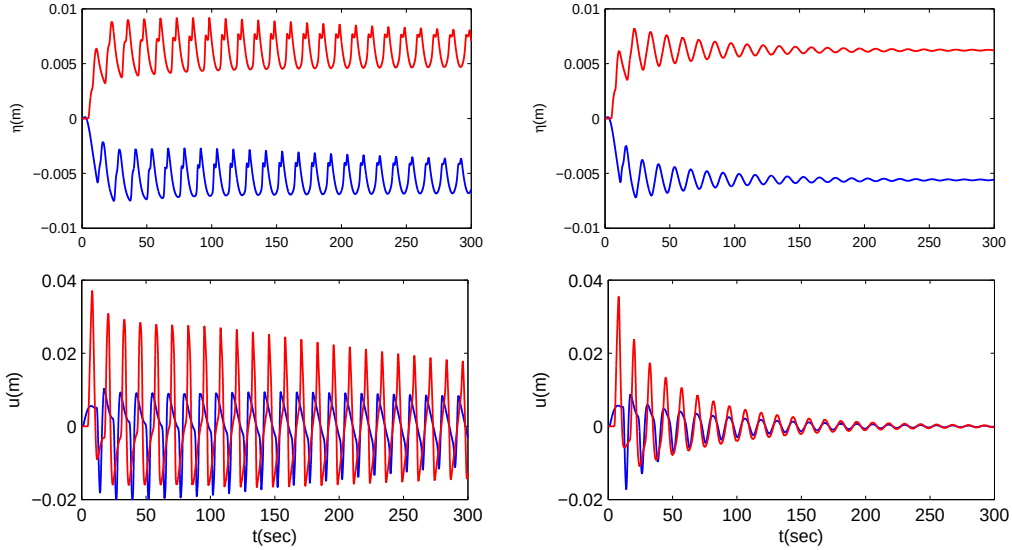

FIGURE 3.4: Time series of η, and u at breaking point (x= 1.65 m-blue lines) and inner surfzone point (x = 6.45 m-red lines) for m=1/50 (Case1D) while neglecting(Left) and including (Right) wave-current interaction.

The relationship between the decay/growth rate of the surface elevation and current and the normalized bed slope at the breaking point for all cases are shown in figure 3.7. For case1, the half-life of surface elevation and current are defined, otherwise the 10 percent growth rate of surface elevation and current are defined for case2. The results shows that decay rate of both parameters are inversely proportional to the normalized bed slope. For case2, the growth rate is faster when the normalized bed slope is decreased. In case2A and 2B, we cannot define the growth rate of water surface elevation and current because both parameter are gently increase (longer than 300s).

3.3.1.2 Mean Quantities

In order to understand the response of the low frequency motion, the mean quantities of each term in the momemtum balance given by equation(3.2) are shown in figure 3.8. Basically, we observe that pressure and radiation stress gradient are dominant in the momemtum balance equation. We also find that the wave-current in-

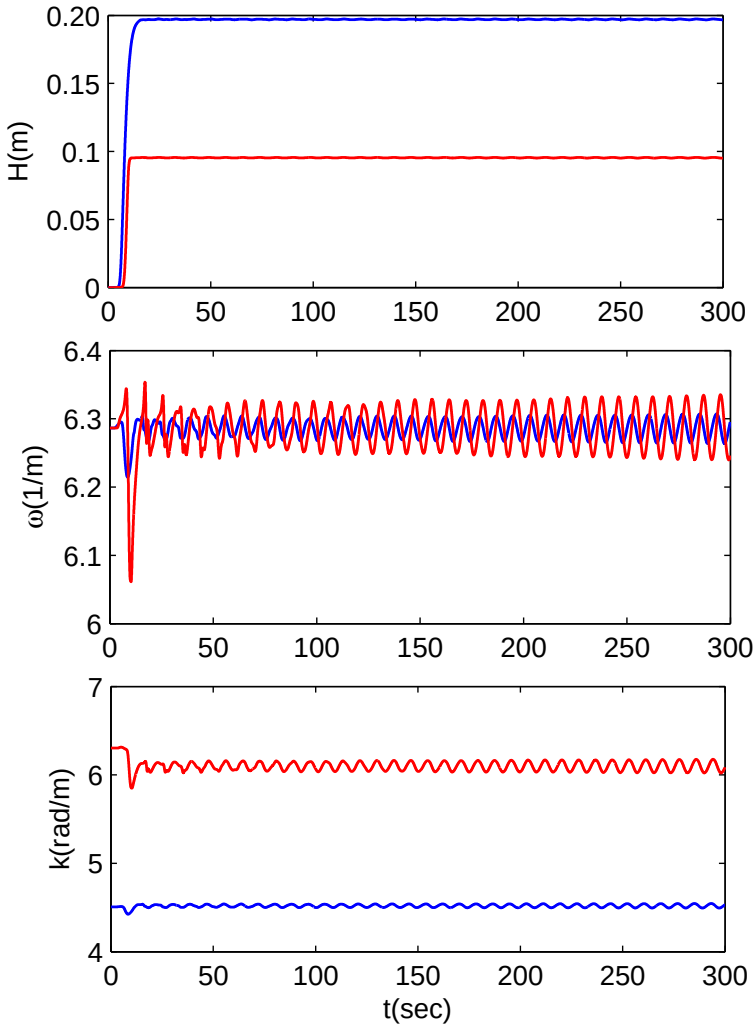

FIGURE 3.5: Time series for m=1/10 (Case2D) including wave-current interaction. Results for wave height(H), ω, and k at breaking point (x= 5.30 m-blue lines) and inner surfzone point (x = 7.30 m-red lines)

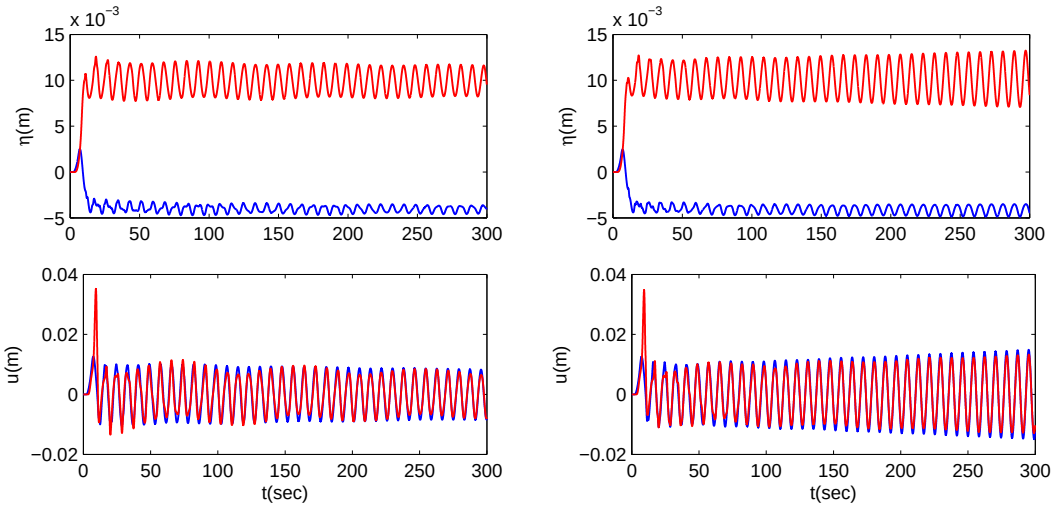

FIGURE 3.6: Time series of η, and u at breaking point (x= 5.30 m-blue lines) and inner surfzone point (x = 7.30 m-red lines) for m=1/10 (Case2D) while neglecting(Left) and including (Right) wave-current interaction.

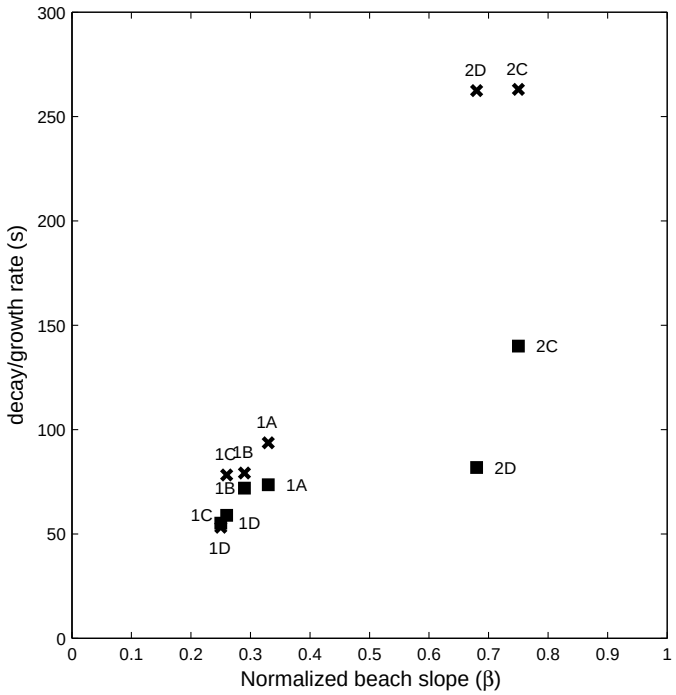

FIGURE 3.7: The decay/growth rate of water surface elevation and current when when including wave-current interaction at the breaking point for all cases. The squared and x marks represent the water elevation and current, respectively.

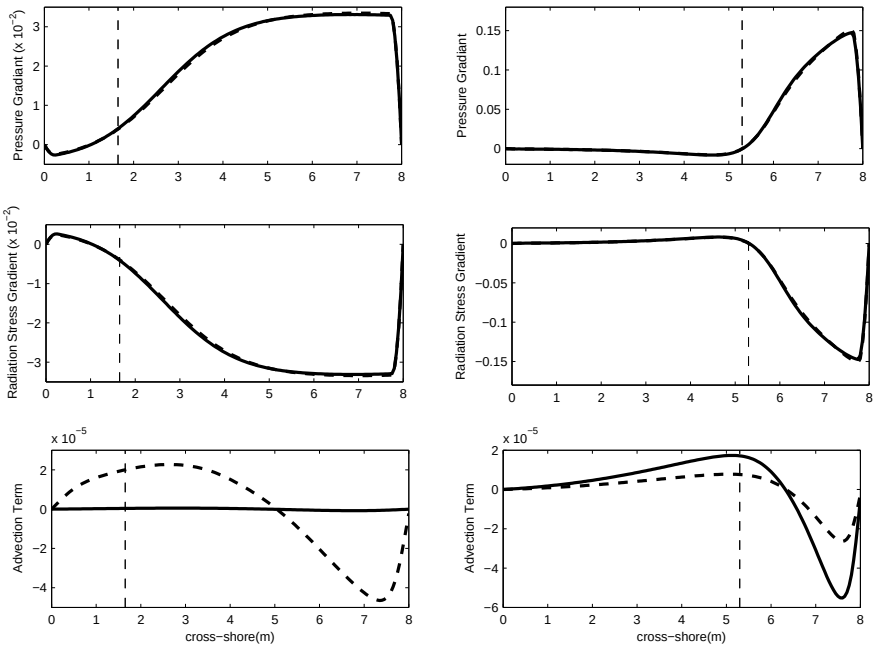

FIGURE 3.8: Mean Quantities of momentum terms for $case1D$ (Left) and $case2D$ (Right). Mean pressure gradient, radiation stress gradient, and advection gradient neglecting (dashed lines) and including (solid lines) wave-current interaction. The vertical dashed lines represent the mean breaking point

teraction plays a role along the crossshore for both cases by amplifying the magnitude of both terms. The advection term is appreciably increased when the wave-current is considered for $case1D$ that is in opposite to $case2D$. However, it is much more pronounce in $case1$ while wave-current interaction is included.

3.3.1.3 Frequency modulation amplitude and seiching mode profile

To quantify the frequency modulation amplitude ($A*$), we followed the method by Haller and Özkan-Haller (2007). The amplitude ($A*$) is defined $\sqrt{2}$ times the standard deviation of the demeaned wavefequency $\omega * (x,t) = \omega(x,t) - \omega_0$. Figure 3.9 shows the cross-shore variation of ($A*$) normalized by the mean frequency (ω_0) for $case1$ and $case2$ while excluding and including the wave-current interaction. The figure shows that $A*$ is increased along the cross shore direction pointing shoreward. The maximum $A*$ ranges from 0.5-0.7 % and 1.0-1.1 % of the mean frequency for

*case*1 and *case*2, respectively. When wave-current interaction is considered, $A*$ is amplified for both cases, but it is much more pronounced in *case*2. The maximum $A*$ ranges from 0.9-1.2 % and 1.4-2.1 % of the mean frequency for *case*1 and *case*2, respectively. We also observe that the maximum of $A*$ relates with the maximum value of $\hat{\eta}$ where $\hat{\eta}$ is the model profile of the seiching as illustrated in figure 3.9. Our results agree well with Haller and Özkan-Haller (2007). From the numerical results, we estimate the modal profiles $\hat{\eta}(x)$ and $\hat{u}(x)$ by using $\hat{\eta} = 2\hat{F}_s$ and $\hat{u} = 2\hat{F}_s$ where $\hat{F}_s$ is the spectrally averaged Fourier coefficient at each location and seiching frequency. The cross-shore variation of $\hat{\eta}$ in figure 3.2 shows a nodal point near the center of the tank and large amplitude at both boundaries and the velocities $\hat{u}$ are zero at the two ends of the tanks. While excluding the wave-current interaction, the amplitude of the cross-shore variation of $\hat{\eta}$ and $\hat{u}$ in *case*1 is larger than *case*2 which explains the higher response of low frequency motion in *case*1. When we include the wave-current interaction, the amplitude of $\hat{\eta}$ and $\hat{u}$ are reduced about 50% and the nodal point is slightly shift offshore about 20 cm in *case*1. On the other hand, the amplitude of $\hat{\eta}$ and $\hat{u}$ are increased about 5-40% and the nodal point is slightly moved onshore about 5 cm in *case*1*C* and *case*1*D* with non-zero amplitude. This might be caused by a small propagating component at this frequency. All of these profiles demonstrate the lowest seiching mode. However, we observe higher seiching amplitude at the higher frequency near the offshore boundary and the nodal point as shown in figure 3.2. This is likely from the non-linear nature of the governing equation.

3.3.2 Breaking point excursion

When wave-current interaction is considered, it directly dominates on the wave-height for all cases. The 2-way coupling simulations provide time-dependent breaking point or moving breaking point for both cases, although the breaking excursion is distinctive. 3.10 is an example of the waveheight variation for case1D and case2D. For case1D, the mean breaking point is about 1.65m, and the breaking excursion is

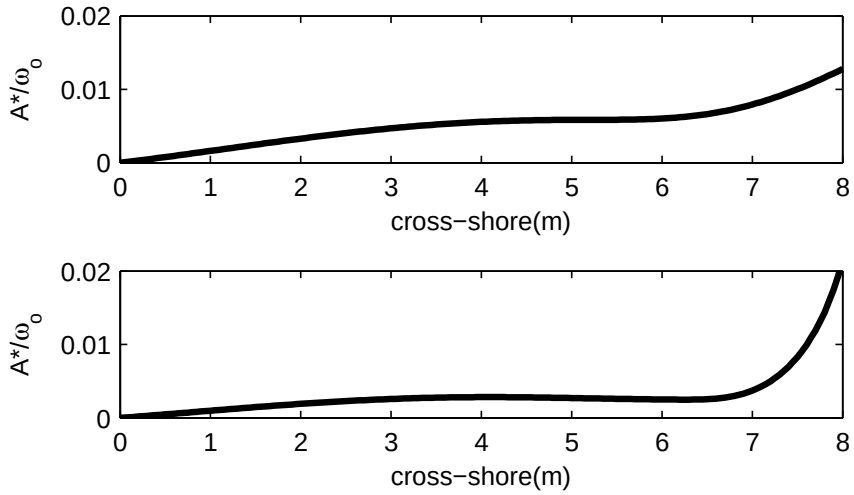

FIGURE 3.9: The frequency modulation amplitude ($A*$) normalized by the mean frequency (ω_0) for **upper)** $case1D$ and **lower)** $case2D$ while including wave-current interaction

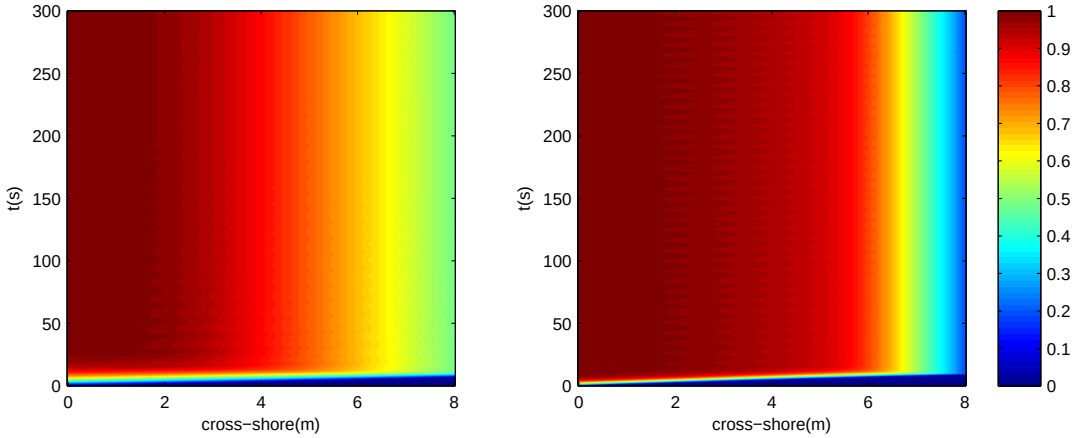

FIGURE 3.10: The normalized waveheight when wave-current is included. (Right) $case1D$: $x_b = 1.65$ m (Left) $case2D$ $x_b = 5.30$ m

large at the beginning and then it is decreased further in time. If the beach slope is steep (case2D), the mean breaking point is around 5.3 m, the breaking excursion is getting larger with increasing time. The breaking point excursion in steep slope is small compared with the mild slope.

3.4 Discussion

The analysis has focused on the basin standing wave reponses on various beach slopes and forcing from the short waves when wave-current is considered. From the simulation results, we find that the basin standing wave responses differently when wave-current interaction is considered for two cases. This might be caused by the transfering energy between the short wave and basin standing wave. As figure 3.4 and figure 3.6 show the variation of η and u in both spatial and temporal scales while neglecting and including the wave-current interaction terms for two different slopes and forcing funcings. The wave-current interaction acts on two cases differently, one depressing the low frequency motion and the other amplifying the low frequency motion. The rate of response is also different for two cases.

These effects involve with the energy exchange between the incoming wave field and the low frequency wave. From wave energy equation (Yu and Slinn, 2003), we rearrange this equation and isolate the wave-current interaction terms on the right-hand side (RHS):

$$\frac{\partial}{\partial t}E + \frac{\partial}{\partial x}(ECg) + D = -\frac{\partial}{\partial x}(Eu) - S_{xx}\frac{\partial}{\partial x}u \tag{3.19}$$

where $S_{xx}\frac{\partial}{\partial x}u$ is the rate which the flow does work againt the radiation stress (S_{xx}). If the RHS of equation (3.19) is positive, the wave field gains energy from the work done. We observe the sign of the RHS in spatial and temporal scale in figure3.11 and figure 3.12 for $case1$ and $case2$ while excluding and including wave-current interaction. This figure shows that RHS correlates well with the cross-shore gradient of u, so the the work done term ($-S_{xx}\frac{\partial}{\partial x}u$) is the dominant term for the RHS of wave energy equation. The positive sign area specify the wave field gain energy at the expense of the low frequency motion, and the negative sign specify opposit. For better demonstrating the energy transfer, we look at times series of work done term $S_{xx}\frac{\partial}{\partial x}u$ of each

case while excluding and including wave-current interaction at three locations (figure 3.12). Considering wave-current interaction, work done is significantly decreased in $case1$ while it is slighlty increased in $case2$. Therefore, this energy exchange identifies the distinctive response between the cases.

The energy transfering between the short wave and low frequency wave has been discussed by considering two terms which are $S_{xx}\frac{\partial U}{\partial x}$ (Loguet-Higgins and Stewart, 1996) and $U\frac{\partial S_{xx}}{\partial x}$ [Van Dongeren et al. (1996) and Battjes et al. (2004)]. The first one is what we use to discuss. This term is that the rate at which the flow $\frac{\partial U}{\partial x}$ does work against the radiation stress ∂S_{xx}. The second one represents the work done on the forced or free long wave by the shorter period waves. However, the energy exchange mechnism is still unclear (Baldock, 2012).

Then, a cross-correlation analysis is conducted here to find out the the relationship between the short wave and incoming basin standing wave in the component of elevation. We also calculate the corresponding 95% confidence limit for the cross-correlations as $\frac{1.96}{\sqrt{N}}$, where N is the number of points. Next, the basin standing wave is seperated into incoming (η_{in}) and outgoing (η_{out}) components by using the method described by Guza et al. (1984)

$$\eta_{in} = \frac{\eta + U\sqrt{\frac{h}{g}}}{2} \quad \eta_{out} = \frac{\eta - U\sqrt{\frac{h}{g}}}{2} \tag{3.20}$$

$$u_{in} = \frac{c\eta_{in}}{h} \quad u_{out} = -\frac{c\eta_{out}}{h} \tag{3.21}$$

where $c = \sqrt{gh}$ and U is the basin standing wave velocity. This method assumes that wave is shore normal and neglecting the water depth variation. Figure 3.13 illustrates the cross-correlation between the short wave and incoming elevation for $case1D$ and $case2D$ at three locations where are the same locations of the previous section. For case1D, a negative correlation is found out, with close to zero time lag at all three locations. This implies that there is the presence of Bound Long Wave (BLW),

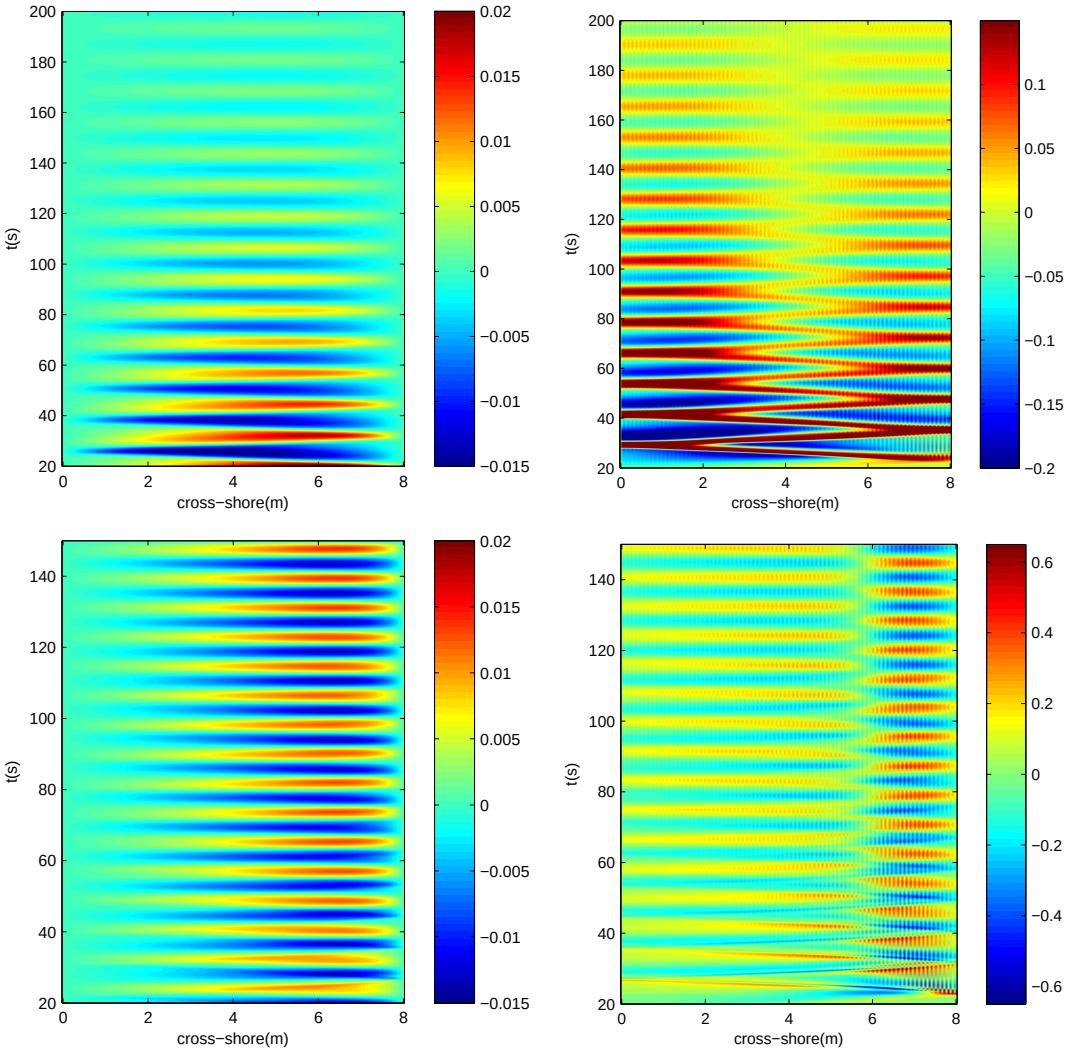

FIGURE 3.11: RHS of wave energy equation (3.19) while excluding and including wave-current interaction for $case1D$ (left) and $case2D$(right)

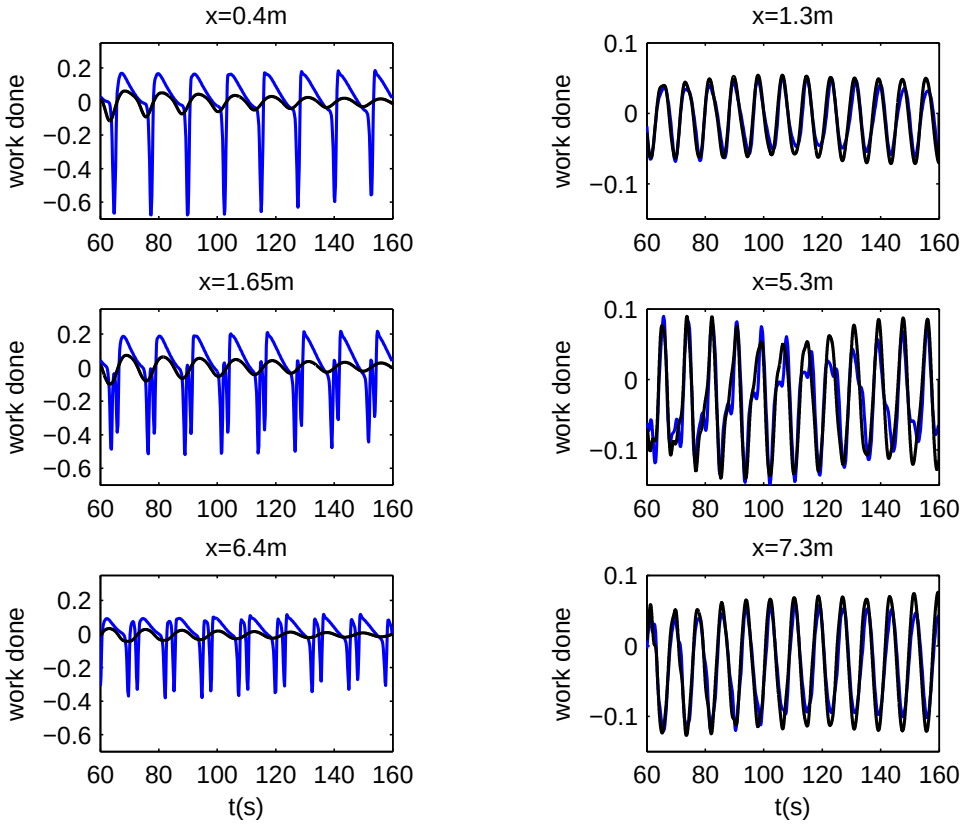

FIGURE 3.12: Time evolution of work done excluding (blue lines) and including (black lines) wave-current interaction for $case1D$ (Left) and $case2D$ (Right)

consistent with results reported by Contardo and Symonds (2013). Therefore, the short wave and incoming elevation is about 180° out of phase. Conversely, we observe the positive correlation at all three locations with close to zero time lag for $case2$. This indicates the short wave and incoming elevation are in phase. The positive correlation conducts to the presence of breakpoint forcing mechanism. The cross-correlation analysis results confirm the different basin standing wave mechanisms for both cases. Then we compute the surfbeat similarity ($\xi_{surfbeat}$) proposed by Baldock (2012) to identify the surfbeat generation mechanism. The surfbeat similarity combined the normalized bed slope (β) (Battjes et al., 2004) and the square root of wave steepness (H_0/L_0) is given below.

$$\beta_s = \frac{m}{\omega_{low}}\sqrt{\frac{g}{h_s}} \tag{3.22}$$

$$\xi_{surfbeat} = \beta_s\sqrt{\frac{H_0}{L_0}} \tag{3.23}$$

where h_s is the depth in the shoaling zone, ω_{low} is the low frequency wave or seiching frequency and H_0 and L_0 refer to the short wave or offshore wave conditions. **Table 3.1** shows the calculation of $\xi_{surfbeat}$, β_s, $\frac{H_0}{L_0}$ from 2-way coupling simulations. The $\xi_{surfbeat}$ of $case1$ (in the range of 0.1-0.2) is smaller than the $\xi_{surfbeat}$ of $case2$ (in the range of 0.21-0.23). Implying that the breaking point forcing is expected to be dominant in $case2$ and the bound wave release mechanism is expected to be dominat in $caseI$. To verify the accuracy of the simulation results, we also compare the $\xi_{surfbeat}$ value ($\xi_{surfbeat}$=0.21) from Baldock (2012) with $case2A$ ($\xi_{surfbeat}$=0.21) which have similar forcing parameters and bed slope for both cases. Our results relatively close with the calculation from Baldock (2012). Therefore, we can use this parameter to identify the generation mechanism for standing basin wave.

Table 3.1 shows the calculation value of the normalized bed slope (β) defined by Battjes et al. (2004). Using this parameter, we categorize $case1$ as the mild slope regime, and $case2$ as the steep slope regime. Then, the mild waves associated with

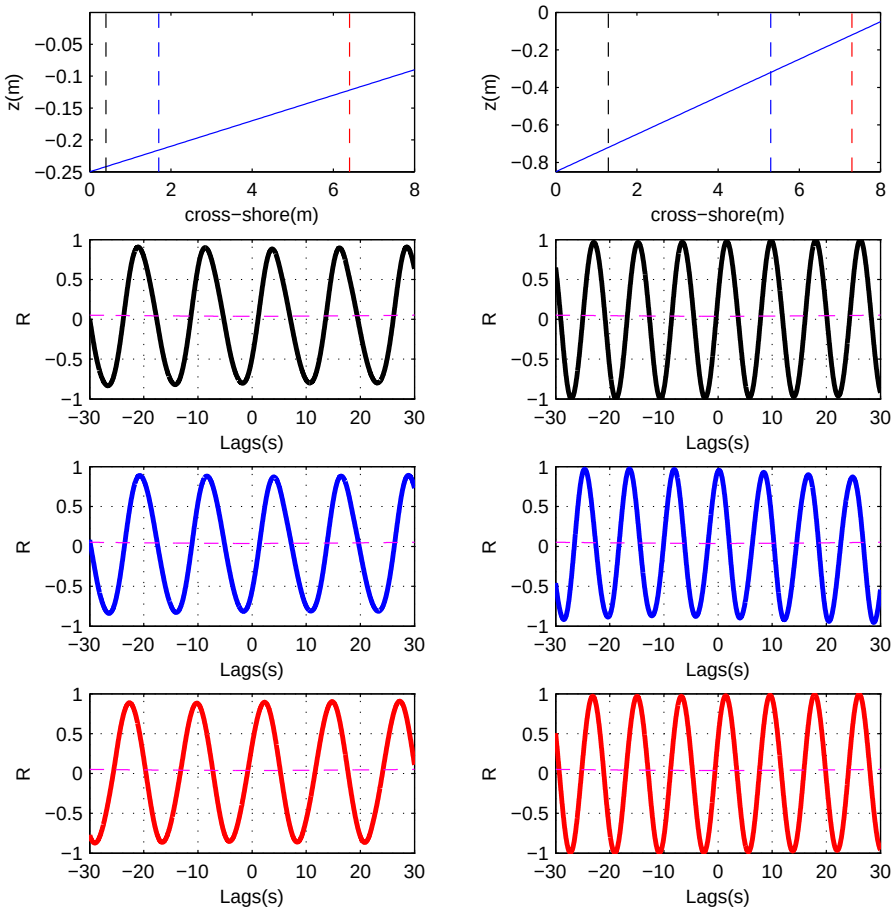

FIGURE 3.13: Cross correlation between the short wave height and basin standing wave incoming elevation when including wave-current interaction at three locations for $case1D$ (Left) and $case2D$ (Right)

the mild slope regime are favorable for bound wave releasing mechanism. In this situation, the basin standing wave is completely released before the short wave breaks. The short wave satisfies the shallow water before breaking. It also conducts to the large breakpoint excursion. For the steep waves and steep slope regime, the short wave breaks before the forced basin standing wave is completely released. Hence, the break point forcing is dominant in this case. The breakpoint excursion is smaller comparing with the case of mild wave and mild slope regime. The results agree well with the surf beat generation mechanisms by numerical simulations Van Dongeren et al. (2007), laboratory experiments [for example, Baldock et al. (2000),Baldock and Huntly (2002) and Baldock (2012)], and field observations [Contardo and Symonds (2013) and Pomeroy et al. (2012)]. As in the preceding section, the response rate of the forced basin standing wave is different in each subcase. We observe that the response relate with the incident wave and bottom slope in term of the surf similarity as shown in table 3.1. We find that the response is inversely proportional to the surf similarity.

3.5 Conclusions

In this study, the effects of wave-current interaction on basin standing waves were analyzed using numerical model involving with the time-integrated Navier-Stokes equations for currents and wave action balance equation for the incident waves. The couple of waves and currents are set pass through the radiation stress concept and wave-current interaction terms. A bottom friction is ignored in these cases. Wave breaking is utilized by using the dissipation function for the random wave.

For the basin standing waves generated on several off-shore wave conditions on two planar slopes, the effect of wave-current interaction acts differently on the two planar slopes as described below. The wave-current interaction plays the important

role on the advection term in momentum equation. It produces the negative feedback when the normalized bed slope (β) is small, hence it reduces the strength of current and the magnitude of seiching. On the other hand, it produces the positive feedback in case of the large normalized bed slope (β). Moreover, we found that wave-current interaction modulates the absolute wave frequency spatially and temporally. Its magnitude increases with distance toward the shore and can reach about 2% of the mean frequency.

The cross-correlations of the incoming basin seiching component of elevation and the short wave at the same location show the different of phase relation on two normalized bed slopes. We found the negative correlation near the zero lag in the negative response case and the positive correlation near the zero time lag in the positive response case. The surf beat similarity parameter($\xi_{surfbeat}$), introduced by Baldock (2012), for two planar slopes are about 0.04 and 0.3 respectively. These correlations and surf beat similarity parameter also conduct to distinguish the mechanisms of the basin seiching wave which are bound wave release and timevarying breakpoint forcing.

4. GENERAL CONCLUSIONS

The first topic, we analyzed the optical intensity signal from individual breaking waves over a fixed bed bar/trough bathymetry. These surface foams were generated by freshwater, shallow water breaking waves, and comparable scales with the field. The bubble plumes form, grow, and decay less than about a wave period. The range of decay time varies from 0.39-1.49 seconds and 0.40-0.88 seconds from domain D_1 and D_2, respectively. The decay time (τ) is similar to whitecap (deep water breaking) but freshwater bubble decay times are faster. Furthermore, the decay time still correlates with increasing ξ_b because this surface foam produced by shallow water breaking waves, and the maximum foam area also relates with ξ_b. For the length scales, we analyzed the length scales by three different methods which are discrete, model, and spectral analysis. The length scales are in the range between 1.60-1.96 m, and 1.54-2.02 m for λ_2 and $\lambda_1 0$, respectively. Both length scales are similar. For spectral analysis, these data display the wide band spectra and the event spacing wavenumbers are less than the wavenumber calculated from the linear wave theory for all runs. From the Probability Density Functions (PDFs), the bubble plume length veries between 0.04L-0.19L. For comparison, the length scale from these data compares favorably with model of Yeh and Mok (1990). However, this model was proposed for uniform bores, nevertheless, there were incoming waves generated in the plume for this laboratory. In the present work, we take a unique approach to analyzing bubble plumes. Also, we pioneer analyze the relationship between the Remotely sensed video intensity data of the individual breaking waves in a different regime from previous experiments (i.e. shallow water, freshwater, and scales) and surface foam. Consequently, it will be a useful data set for model/data comparison.

The second topic, from the optical intensity images from the previous chapter, we found that the breaking point forcing was influenced by basin seiching wave. Therefore, we examined the effects of wavecurrent interaction on the time evolution

of wave motions, water surface elevations and currents by using numerical modeling which involve time integration of the one dimensional Navier Stokes equations, and wave action balance equation. Waves and currents are coupled through the wave forcing effect which is modeled using the radiation stress concept. A linear bottom friction model is ignored. Waves and basin standing waves were generated by several off-shore wave conditions on two planar slopes. The effect of wave-current interaction acts differently on the two planar slopes as described below. It produces the negative feedback when the normalized bed slope (β) is small, hence it reduces the strength of current and the magnitude of seiching. On the other hand, it produces the positive feedback in case of the large normalized bed slope (β). The cross-correlations of the incoming basin seiching component of elevation and the short wave at the same location show the different of phase relation on two normalized bed slopes. It produces the negative correlation near the zero lag in the negative response case and the positive correlation near the zero time lag in the positive response case. The surf beat similarity parameter($\xi_{surfbeat}$), introduced by Baldock (2012), for two planar slopes are about 0.04 and 0.3 respectively. These correlations and surf beat similarity parameter also conduct to distinguish the mechanisms of the basin seiching wave which are bound wave release and timevarying breakpoint forcing.

5. BIBLIOGRAPHY

Andreas, E. L. and Monahan, E. C. (2000). The role of whitecap bubbles in air-sea heat and moisture exchange. *Journal of physical oceanography*, 30(2):433–442.

Andreas, E. L., Persson, P. O. G., and Hare, J. E. (2008). A bulk turbulent air-sea flux algorithm for high-wind, spray conditions. *Journal of Physical Oceanography*, 38(7):1581–1596.

Baldock, T. (2012). Dissipation of incident forced long waves in the surf zoneimplications for the concept of bound wave release at short wave breaking. *Coastal Engineering*, 60:276–285.

Baldock, T., Huntley, D., Bird, P., O'Hare, T., and Bullock, G. (2000). Breakpoint generated surf beat induced by bichromatic wave groups. *Coastal Engineering*, 39(2):213–242.

Baldock, T. and Huntly, D. (2002). Long-wave forcing by the breaking of random gravity waves on a beach. *Proc. R. Soc. London*, Ser.A 458(2025):2177–2201.

Baldock, T. and O'Hare, T. (2004). Energy transfer and dissipation during surf beat conditions. *Pro. of Coastal Processes and Climate Change*.

Battjes, J. (1975). Modeling of turbulence in the surf zone. *Modeling Techniques*, 2:1050–1061.

Battjes, J., Bakkenes, H., Janssen, T., and Van Dongeren, A. (2004). Shoaling of subharmonic gravity waves. *Journal of Geophysical Research: Oceans (1978–2012)*, 109(C2):276–285.

Battjes, J. and Janssen, J. (1978). Energy loss and set-up due to breaking of random waves. *Coastal Engineering Proceedings*, 1(16).

Blenkinsopp, C. and Chaplin, J. (2011). Void fraction measurements and scale effects in breaking waves in freshwater and seawater. *Coastal Engineering*, 58(5):417–428.

Callaghan, A., Stokes, M., and Deane, G. (2014). The effect of water temperature on air entrainment, bubble plumes, and surface foam in a laboratory breaking-wave analog. *Journal of Geophysical Research: Oceans*.

Callaghan, A. H., Deane, G. B., and Stokes, M. D. (2013). Two regimes of laboratory whitecap foam decay: Bubble-plume controlled and surfactant stabilized. *Journal of Physical Oceanography*, 43(6):1114–1126.

Callaghan, A. H., Deane, G. B., Stokes, M. D., and Ward, B. (2012). Observed variation in the decay time of oceanic whitecap foam. *Journal of Geophysical Research: Oceans (1978–2012)*, 117(C9).

Camps, A., Vall-Llossera, M., Villarino, R., Reul, N., Chapron, B., Corbella, I., Duffo, N., Torres, F., Miranda, J. J., Sabia, R., et al. (2005). The emissivity of foam-covered water surface at l-band: Theoretical modeling and experimental results from the frog 2003 field experiment. *Geoscience and Remote Sensing, IEEE Transactions on*, 43(5):925–937.

Cartwright, D. and Longuet-Higgins, M. S. (1956). The statistical distribution of the maxima of a random function. *Proceedings of the Royal Society of London. Series A. Mathematical and Physical Sciences*, 237(1209):212–232.

Catalán, P. (2005). Hybrid approach to estimating nearshore bathymetry using remote sensing. Master's thesis, Oreg. State Univ, Corvallis.

Catalán, P. and Haller, M. C. (2005). Nonlinear phase speeds and depth inversions. In *Coastal Dynamics*, volume 5.

Catálan, P. A. and Haller, M. C. (2008). Remote sensing of breaking wave phase speeds with application to non-linear depth inversions. *Coastal Engineering*, 55(1):93–111.

Catalán, P. A., Haller, M. C., Holman, R. A., and Plant, W. J. (2011). Optical and microwave detection of wave breaking in the surf zone. *Geoscience and Remote Sensing, IEEE Transactions on*, 49(6):1879–1893.

Chen, Q., Dalrymple, R. A., Kirby, J. T., Kennedy, A. B., and Haller, M. C. (1999). Boussinesq modeling of a rip current system. *Journal of Geophysical Research: Oceans (1978–2012)*, 104(C9):20,617–20,637.

Cipriano, R. J. and Blanchard, D. C. (1981). Bubble and aerosol spectra produced by a laboratory breaking wave. *Journal of Geophysical Research: Oceans (1978–2012)*, 86(C9):8085–8092.

Contardo, S. and Symonds, G. (2013). Infragravity response to variable wave forcing in the nearshore. *Journal of Geophysical Research: Oceans*, 118:7095–7106.

Cox, D. T. and Kobayashi, N. (2000). Identification of intense, intermittent coherent motions under shoaling and breaking waves. *Journal of Geophysical Research: Oceans (1978–2012)*, 105(C6):14223–14236.

Cox, D. T. and Shin, S. (2003). Laboratory measurements of void fraction and turbulence in the bore region of surf zone waves. *Journal of engineering mechanics*, 129(10):1197–1205.

Dally, W. R. and Brown, C. A. (1995). A modeling investigation of the breaking wave roller with application to cross-shore currents. *Journal of Geophysical Research: Oceans (1978–2012)*, 100(C12):24873–24883.

Deane, G. B. (1997). Sound generation and air entrainment by breaking waves in the surf zone. *The journal of the acoustical society of America*, 102(5):2671–2689.

Deane, G. B. and Stokes, M. D. (1999). Air entrainment processes and bubble size distributions in the surf zone. *Journal of Physical Oceanography*, 29(7):1393–1403.

Deane, G. B. and Stokes, M. D. (2002). Scale dependence of bubble creation mechanisms in breaking waves. *Nature*, 418(6900):839–844.

Derakhti, M. and Kirby, J. T. Energy and momentum flux under unsteady breaking waves.

Duncan, J. (1981). An experimental investigation of breaking waves produced by a towed hydrofoil. *Proceedings of the Royal Society of London. A. Mathematical and Physical Sciences*, 377(1770):331–348.

Farmer, D. M., Deane, G. B., and Vagle, S. (2001). The influence of bubble clouds on acoustic propagation in the surf zone. *Oceanic Engineering, IEEE Journal of*, 26(1):113–124.

Frouin, R., Schwindling, M., and Deschamps, P.-Y. (1996). Spectral reflectance of sea foam in the visible and near-infrared: In situ measurements and remote sensing implications. *Journal of Geophysical Research: Oceans (1978–2012)*, 101(C6):14361–14371.

Goda, Y. (2010). *Random seas and design of maritime structures*. World Scientific.

Goddijn-Murphy, L., Woolf, D. K., and Callaghan, A. H. Parameterizations and algorithms for oceanic whitecap coverage. *Journal of Physical Oceanography*, 41(4).

Gonzalez, R. and Woods, R. (2001). *Digital Image Processing*. Prentice-Hall, New Jersey, 2nd edition.

Govender, K., Mocke, G., and Alport, M. (2004). Dissipation of isotropic turbulence and length-scale measurements through the wave roller in laboratory spilling waves. *Journal of Geophysical Research: Oceans (1978–2012)*, 109(C8).

Guza, R., Thornton, E., and R.Holman (1984). Swash on steep and shallow beaches. *Coastal Engineering Proceedings*, 1(19):708–723.

Haas, K., Svenden, I., and M.C.Haller (1999). Numerical modeling of nearshore circulation on a barred beach with rip channels. *Coastal Engineering1998:Proceedings of the 26th International Conference*, 1:801–814.

Haller, M. C. and Catalán, P. (2009). Remote sensing of wave roller lengths in the laboratory. *Journal of Geophysical Research: Oceans (1978–2012)*, 114(C7).

Haller, M. C., Dalrymple, R., and Svenden, I. (1997). Experimental modeling of a rip current system. *paper presented at Ocean Wave Measurement and Analysis Am.Soc. of Civ. Eng.* Virginia Beach VA.

Haller, M. C. and Özkan-Haller, T. (2007). Waves on unsteady currents. *Physics of Fluids (1994-present)*, 19(12):126601(1)126601(12).

Henderson, S. M. and Bowen, A. (2002). Observations of surf beat forcing and dissipation. *Journal of Geophysical Research: Oceans (1978–2012)*, 107(C11):1–14.

Holman, R. A. and Stanley, J. (2007). The history and technical capabilities of argus. *Coastal Engineering*, 54(6):477 491.

Iafrati, A. (2011). Energy dissipation mechanisms in wave breaking processes: Spilling and highly aerated plunging breaking events. *Journal of Geophysical Research: Oceans (1978–2012)*, 116(C7).

Janssen, T., Battjes, J., and van Dongeren, A. (2003). Long waves induced by short-wave groups over a sloping bottom. *Journal of Geophysical Research: Oceans (1978–2012)*, 108(C8):1–14.

Jones, B. (2000). A numerical study of wave refraction in shallow tidal waters. *Estuarine, Coastal and Shelf Science*, 51:331–347.

Koepke, P. (1986). Remote sensing signatures of whitecaps. In *Oceanic whitecaps*, pages 251–260. Springer.

Lamarre, E. and Melville, W. (1991). Air entrainment and dissipation in breaking waves. *Nature*, 351(6326):469–472.

Lamarre, E. and Melville, W. K. (1992). Instrumentation for the measurement of void-fraction in breaking waves: laboratory and field results. *Oceanic Engineering, IEEE Journal of*, 17(2):204–215.

Leifer, I. and De Leeuw, G. (2006). Bubbles generated from wind-steepened breaking waves: 1. bubble plume bubbles. *Journal of Geophysical Research: Oceans (1978–2012)*, 111(C6).

Liang, J.-H., McWilliams, J. C., Sullivan, P. P., and Baschek, B. (2011). Modeling bubbles and dissolved gases in the ocean. *Journal of Geophysical Research: Oceans (1978–2012)*, 116(C3).

Loewen, M. and Melville, W. (1991). Microwave backscatter and acoustic radiation from breaking waves. *Journal of Fluid Mechanics*, 224:601–623.

Loewen, M. and Melville, W. (1994). An experimental investigation of the collective oscillations of bubble plumes entrained by breaking waves. *The Journal of the Acoustical Society of America*, 95(3):1329–1343.

Loguet-Higgins, M. and Stewart, R. (1996). Changes in the form of short gravity waves on long waves and tidal currents. *Journal of Fluid Mechanics*, 8:565–583.

Longuet-Higgins, M. and Stewart, R. (1962). Radiation stress and mass transport in gravity waves with application to surf beats. *Journal of Fluid Mechanics*, 13:485–504.

Ma, G., Shi, F., and Kirby, J. T. (2011). A polydisperse two-fluid model for surf zone bubble simulation. *Journal of Geophysical Research: Oceans (1978–2012)*, 116(C5).

Melville, W. and Rapp, R. J. (1985). Momentum flux in breaking waves. *Nature*, 317(6037):514–516.

Mironov, A. S. and Dulov, V. A. (2008). Detection of wave breaking using sea surface video records. *Measurement Science and Technology*, 19(1):015405.

Mok, K. M., Yuen, K. V., Cheong, K., and Hoi, K. I. (2013). A search for the dominant free surface-fluctuation frequency downstream of the oscillating hydraulic jump with the bayesian spectral density approach. *Physica Scripta*, 2013(T155):014007.

Monahan, E. C., Spiel, D. E., and Davidson, K. L. (1986). A model of marine aerosol generation via whitecaps and wave disruption. In *Oceanic whitecaps*, pages 167–174. Springer.

Munk, W. (1949). Surf beats. *Transactions, American Geophysical Union*, 30:849–854.

Nadaoka, K., Hino, M., and Koyano, Y. (1989). Structure of the turbulent flow field under breaking waves in the surf zone. *Journal of Fluid Mechanics*, 204:359–387.

O'Hare, T. and Huntley, D. (1994). Bar formation due to wave groups and associated long waves. *Marine Geology*, 116(3):313–325.

Özkan-Haller, H. T. and Li, Y. (2003). Effects of wave-current interaction on shear stabilities of longshore currents. *Journal of Geophysical Research: Oceans (1978–2012)*, 108(C5):1–19.

Pinkel, R. (2008). Advection, phase distortion, and the frequency spectrum of finescale fields in the sea. *J. Phys. Ocean.*, 38(2):291–313.

Pomeroy, A., R.Lowe, Symonds, G., Dongeren, A. V., and Moore, C. (2012). The dynamics of infragravity wave transformation over a fringing reef. *Journal of Geophysical Research: Oceans (1978–2012)*, 117(C11022):1–17.

Pumphrey, H. C. and Ffowcs Williams, J. (1990). Bubbles as sources of ambient noise. *Oceanic Engineering, IEEE Journal of*, 15(4):268–274.

Rapp, R. and Melville, W. (1990). Laboratory measurements of deep-water breaking waves. *Philosophical Transactions of the Royal Society of London. Series A, Mathematical and Physical Sciences*, pages 735–800.

Reniers, A. J., Roelvink, J., and Thornton, E. (2004). Morphodynamic modeling of an embayed beach under wave group forcing. *Journal of Geophysical Research: Oceans (1978–2012)*, 109(C1).

Roelvink, J. (1993). Dissipation in random wave groups incident on a beach. *Coastal Engineering*, 19:127–150.

Rojas, G. and Loewen, M. (2010). Void fraction measurements beneath plunging and spilling breaking waves. *Journal of Geophysical Research: Oceans (1978–2012)*, 115(C8).

Ross, D. B. and Cardone, V. (1974). Observations of oceanic whitecaps and their relation to remote measurements of surface wind speed. *Journal of Geophysical Research*, 79(3):444–452.

Scott, C. P., Cox, D. T., Maddux, T. B., and Long, J. W. (2005). Large-scale laboratory observations of turbulence on a fixed barred beach. *Meas. Sci. Technol.*, 16:1903–1912.

Shi, F., Kirby, J. T., and Ma, G. (2010). Modeling quiescent phase transport of air bubbles induced by breaking waves. *Ocean Modelling*, 35:105–117.

Stramski, D. (1994). Gas microbubbles: An assessment of their significance to light scattering in quiescent seas. In *Ocean Optics XII*, pages 704–710. International Society for Optics and Photonics.

Symonds, G., Huntley, D. A., and Bowen, A. J. (1982). Two-dimensional surf beat: Long wave generation by a time-varying breakpoint. *Journal of Geophysical Research: Oceans (1978–2012)*, 87(C1):492–498.

Terrill, E. J., Melville, W. K., and Stramski, D. (2001). Bubble entrainment by breaking waves and their influence on optical scattering in the upper ocean. *Journal of Geophysical Research: Oceans (1978–2012)*, 106(C8):16815–16823.

Thornton, E. and Guza, R. (1983). Transformation of wave height distribution. *J. Geo. Res.*, 88(C10):5925–5938.

Ting, F. C. and Kirby, J. T. (1994). Observation of undertow and turbulence in a laboratory surf zone. *Coastal Engineering*, 24(1):51–80.

Ting, F. C. and Kirby, J. T. (1996). Dynamics of surf-zone turbulence in a spilling breaker. *Coastal Engineering*, 27(3):131–160.

Tolman, H. L. (1990). The influence of unsteady depths and currents of tides on wind-wave progration in shelf seas. *J. of Phys. Ocean*, 20:1166–1174.

Tucker, M. (1950). Surf beats: Sea waves of 1 to 5 min. period. *Pro.R.Soc.London.*, A(202):565–573.

Vagle, S. and Farmer, D. M. (1992). The measurement of bubble-size distributions by acoustical backscatter. *Journal of Atmospheric and Oceanic Technology*, 9(5):630–644.

Van Dongeren, A., Battjes, J., Janssen, T., Van Noorloos, J., Steenhauer, K., Steenbergen, G., and Reniers, A. (2007). Shoaling and shoreline dissipation of low-frequency waves. *Journal of Geophysical Research: Oceans (1978–2012)*, 112(C02011):1–15.

Van Dongeren, A., Svendsen, I., and Sancho, F. (1996). Generation of infragravity waves. *Coastal Engineering Proceedings*, 1(25).

Vandever, J. P., Siegel, E. M., Brubaker, J. M., and Friedrichs, C. T. (2008). Influence of spectal width on wave height parameter estimates in coastal environment. *J. of Waterway, Port, Coastal and Ocean Engineering.*, 134:187–194.

Voulgaris, G. and Collins, M. (2000). Sediment resuspension on beaches: response to breaking waves. *Marine geology*, 167(1):167–187.

Watanabe, Y. and Mori, N. (2008). Infrared measurements of surface renewal and subsurface vortices in nearshore breaking waves. *Journal of Geophysical Research: Oceans (1978–2012)*, 113(C7).

Watanabe, Y., Saeki, H., and Hosking, R. J. (2005). Three-dimensional vortex structures under breaking waves. *Journal of Fluid Mechanics*, 545:291–328.

Woolf, D. K. (1997). Bubbles and their role in gas exchange. *The Sea*.

Yeh, H. H. and Mok, K.-M. (1990). On turbulence in bores. *Physics of Fluids A: Fluid Dynamics (1989-1993)*, 2(5):821–828.

Yu, L. and Slinn, D. N. (2003). Effects of wave-current interaction on rip currents. *Journal of Geophysical Research: Oceans (1978–2012)*, 108(C3):(33)1–(33)19.

Zhang, X., Lewis, M., and Johnson, B. (1998). Influence of bubbles on scattering of light in the ocean. *Applied Optics*, 37(27):6525–6536.

6. APPENDICES

A Analysis of surface foam area

The bubble areas are defined by zero-upcrossings of threshold pixel intensity value chosen here as $\overline{I} + \sigma_I$ where $\overline{I} + \sigma_I$ are the mean and standard deviation of the pixel intensity of a given time stack $I(x,t)$. And then the intensity is integrated all over cross-shore distance and active breaking zone to compare in terms of the decay time and area.

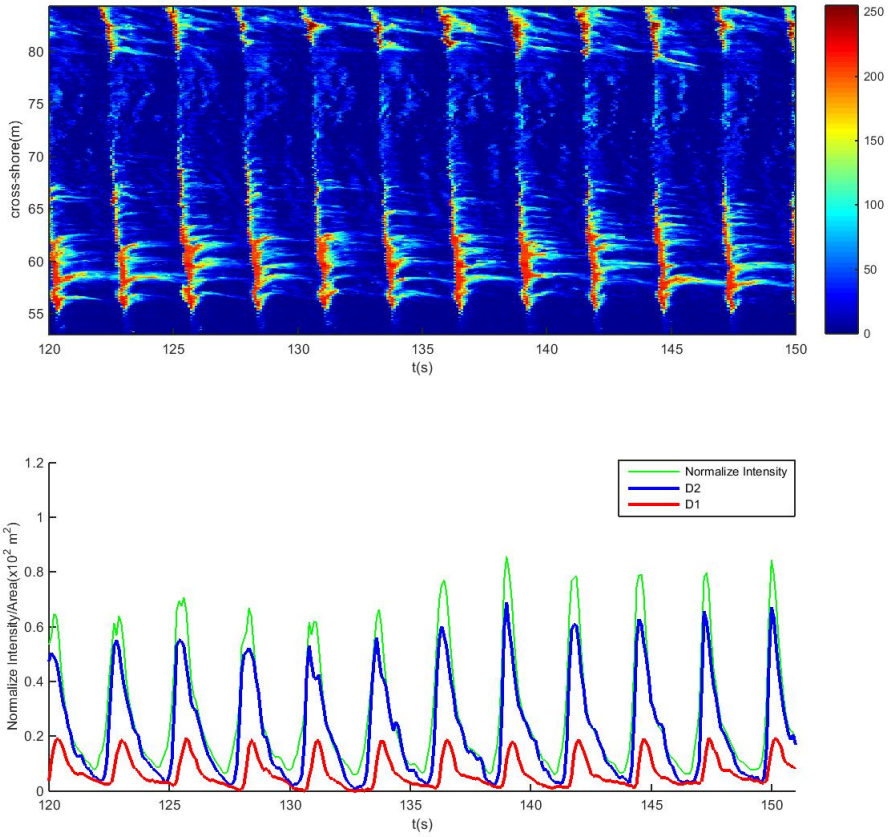

FIGURE 1.1: Define bubble area by using binary image for RUN35: D1 is surface foam area calculating from bar crest to bar trough (G3:G46), D2 is surface foam area starting from breaking point to shoreline (G3:G6)

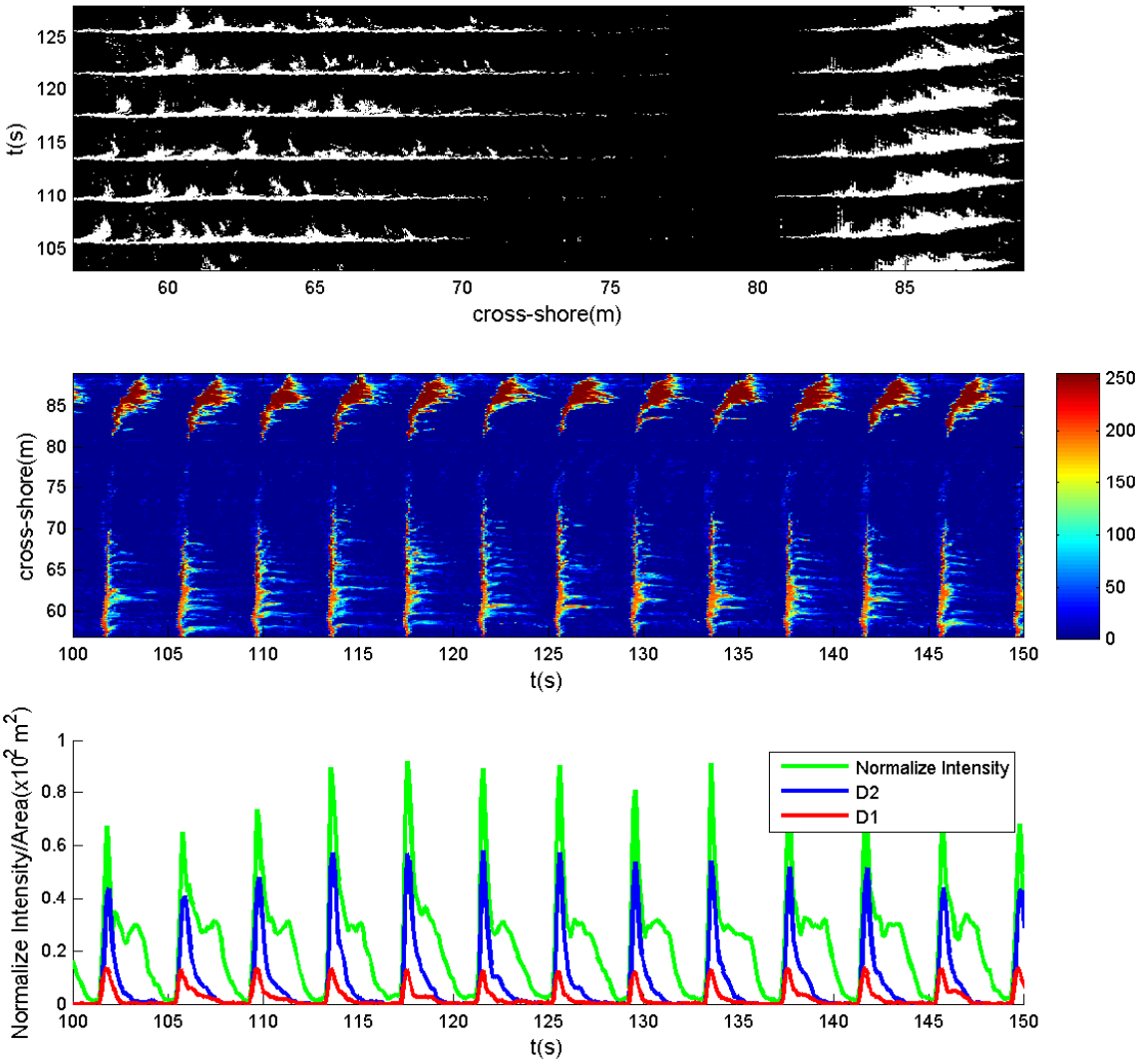

FIGURE 1.2: Define bubble area by using binary image for RUN40: D1 is surface foam area calculating from bar crest to bar trough (G3:G46), D2 is surface foam area starting from breaking point to shoreline (G2:G6)

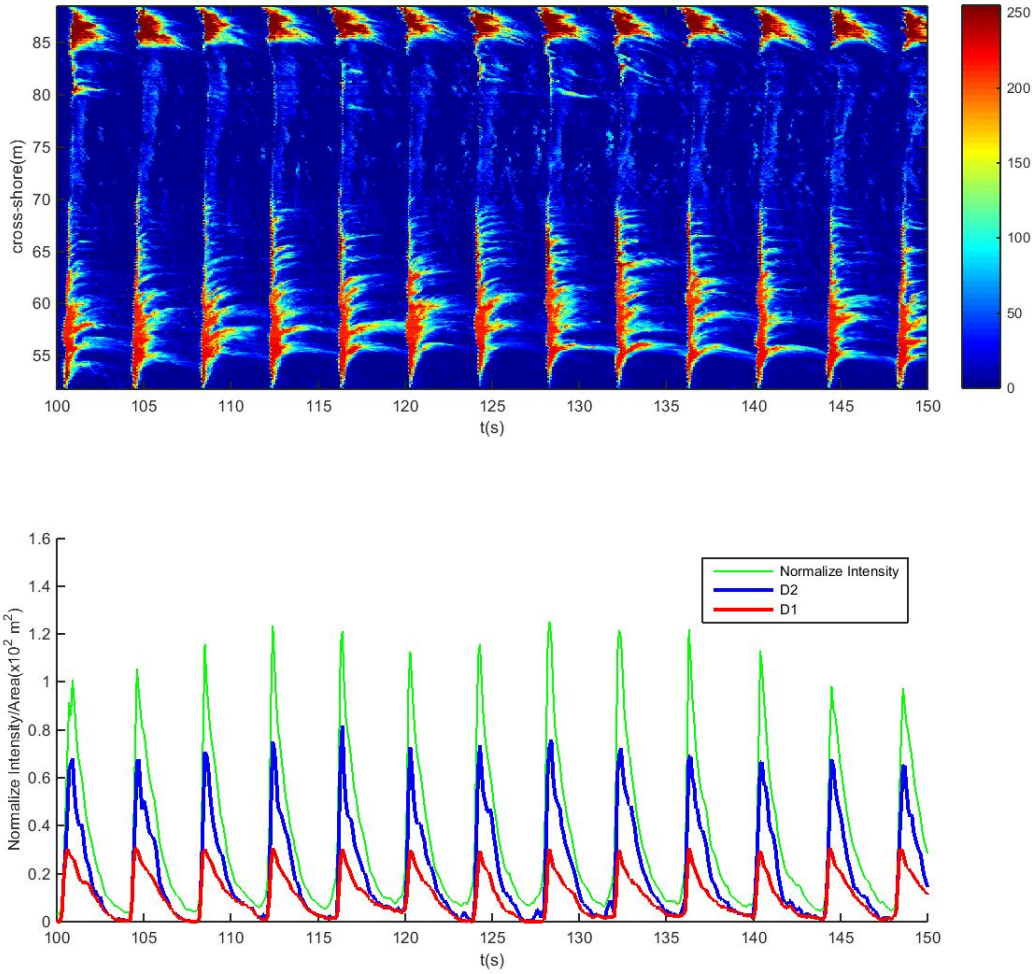

FIGURE 1.3: Define bubble area by using binary image for RUN36: D1 is surface foam area calculating from bar crest to bar trough (G3:G46), D2 is surface foam area starting from breaking point to shoreline (G2:G6)

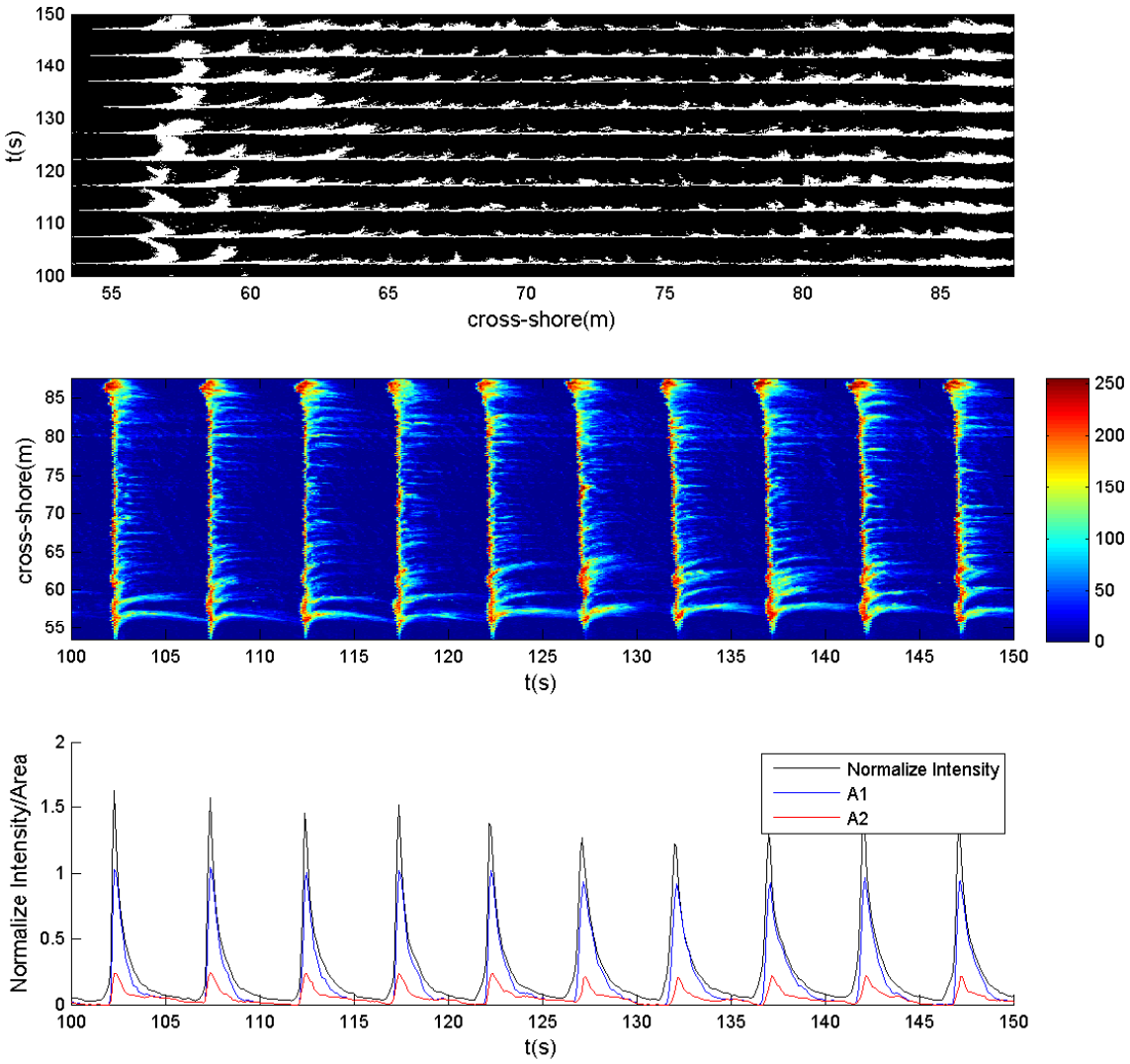

FIGURE 1.4: Define bubble area by using binary image for RUN37: D1 is surface foam area calculating from bar crest to bar trough (G3:G46), D2 is surface foam area starting from breaking point to shoreline (G2:G6)

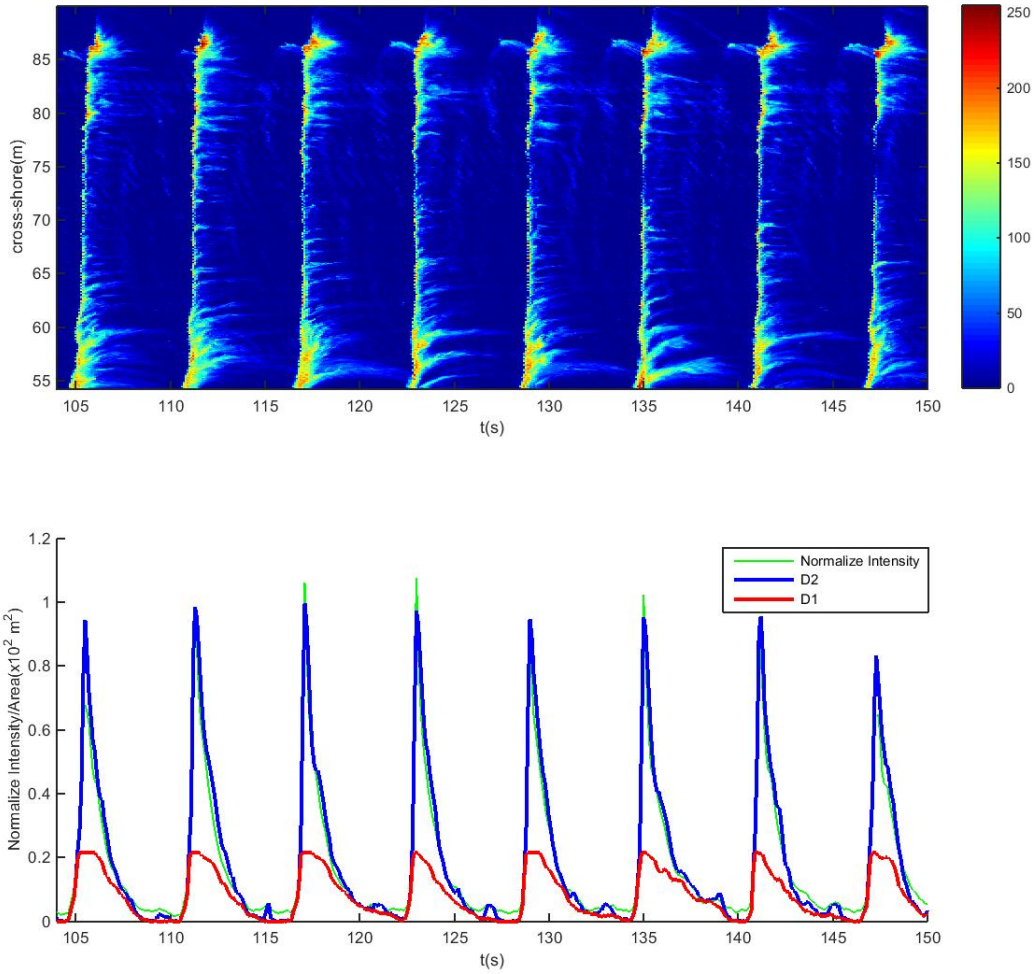

FIGURE 1.5: Define bubble area by using binary image for RUN38: D1 is surface foam area calculating from bar crest to bar trough (G3:G46), D2 is surface foam area starting from breaking point to shoreline (G2:G6)

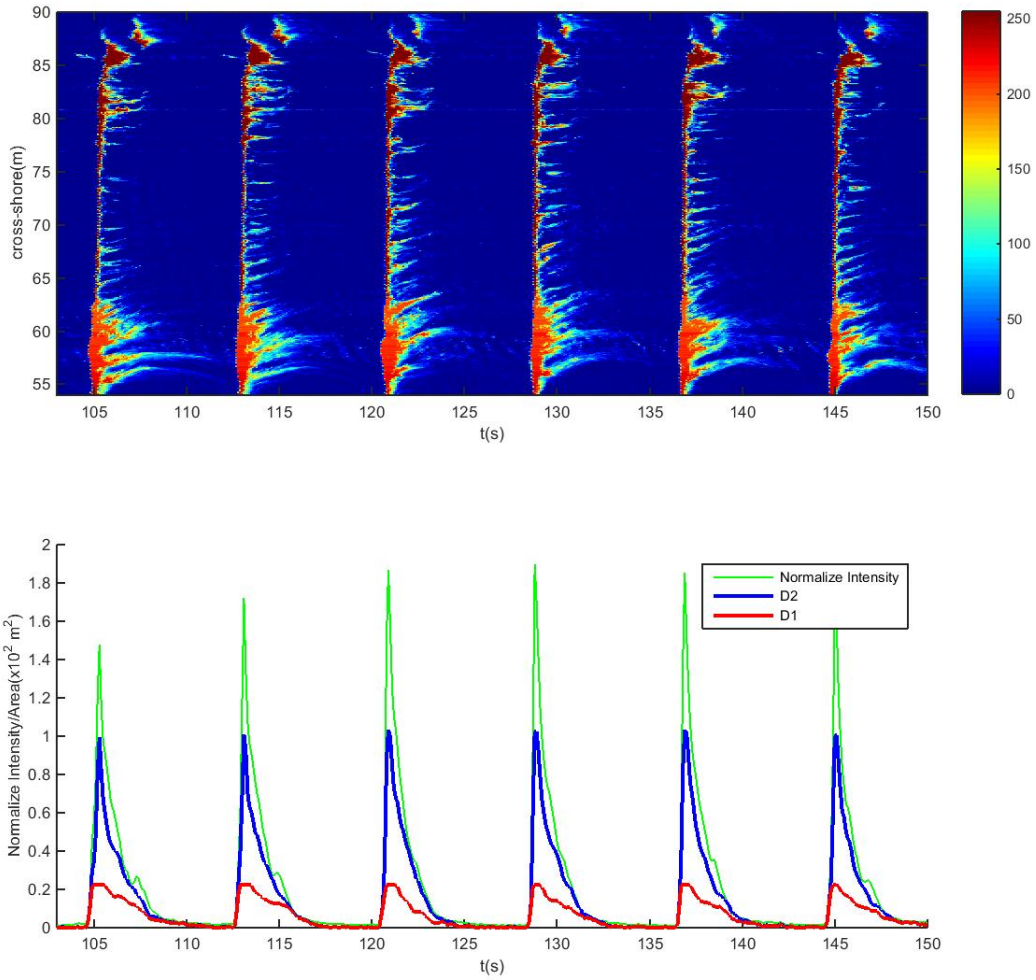

FIGURE 1.6: Define bubble area by using binary image for RUN33: D1 surface foam area calculating from bar crest to bar trough (G3:G46), D2 is surface foam area starting from breaking point to shoreline (G2:G6)

B Analysis of surface foam length scales

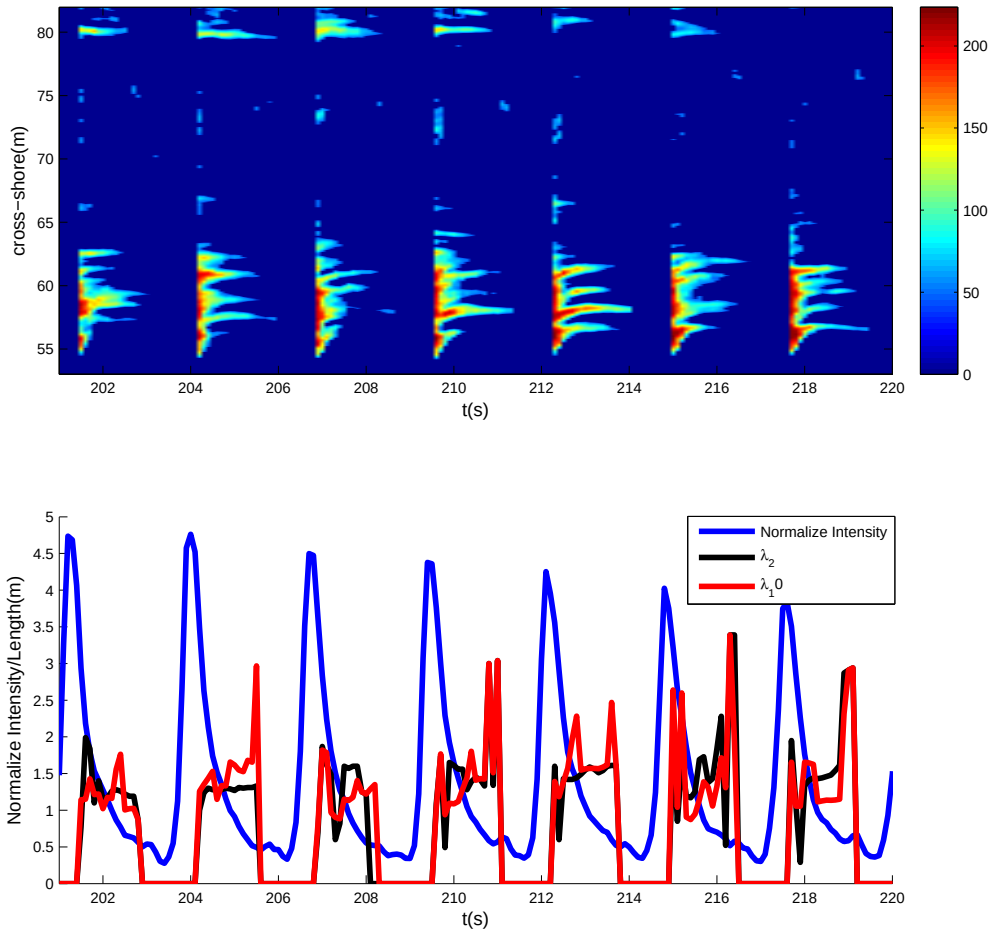

FIGURE 2.1: Time variation of surface foam length scales RUN35

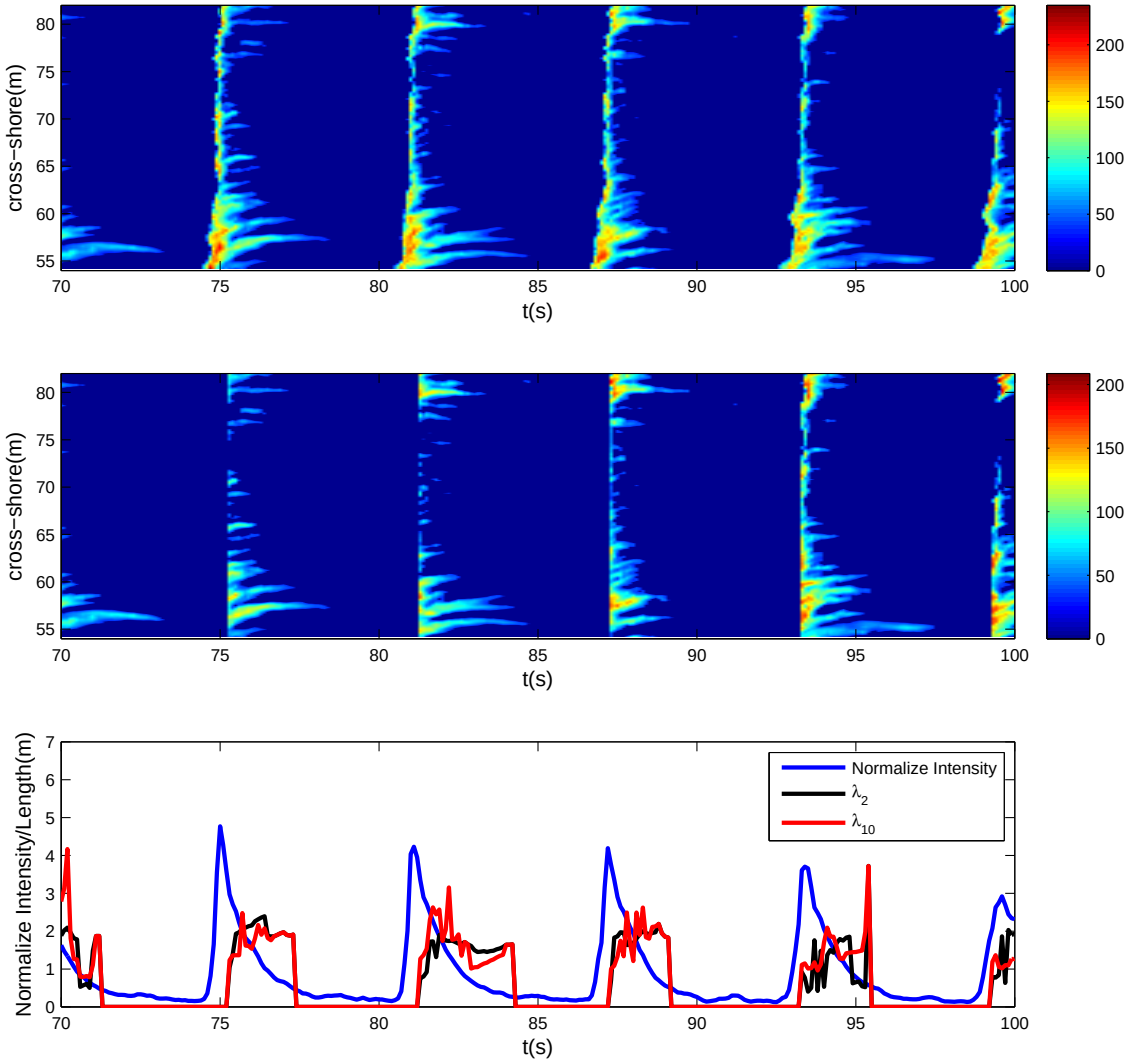

FIGURE 2.2: Time variation of surface foam length scales RUN40

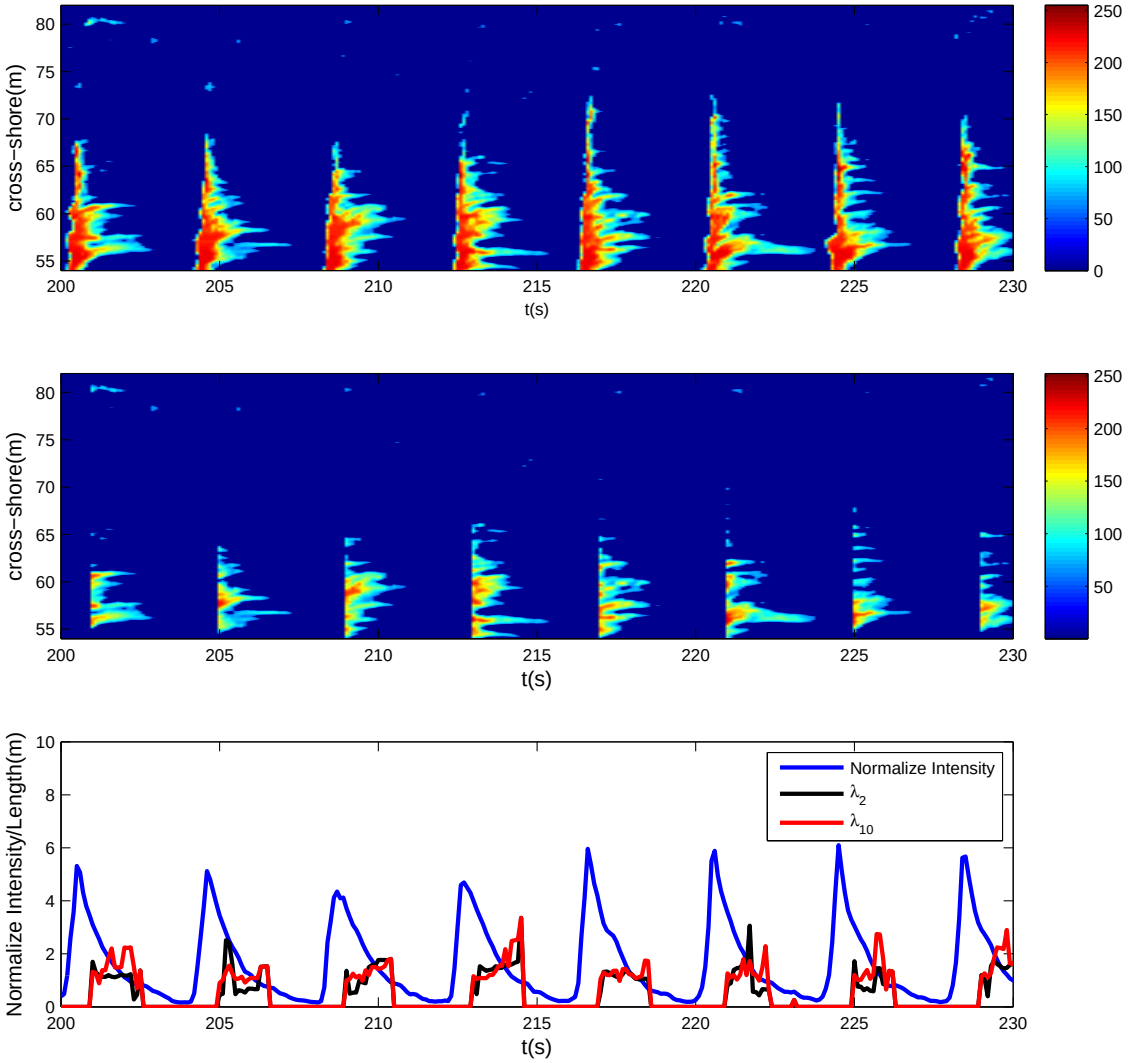

FIGURE 2.3: Time variation of surface foam length scales RUN36

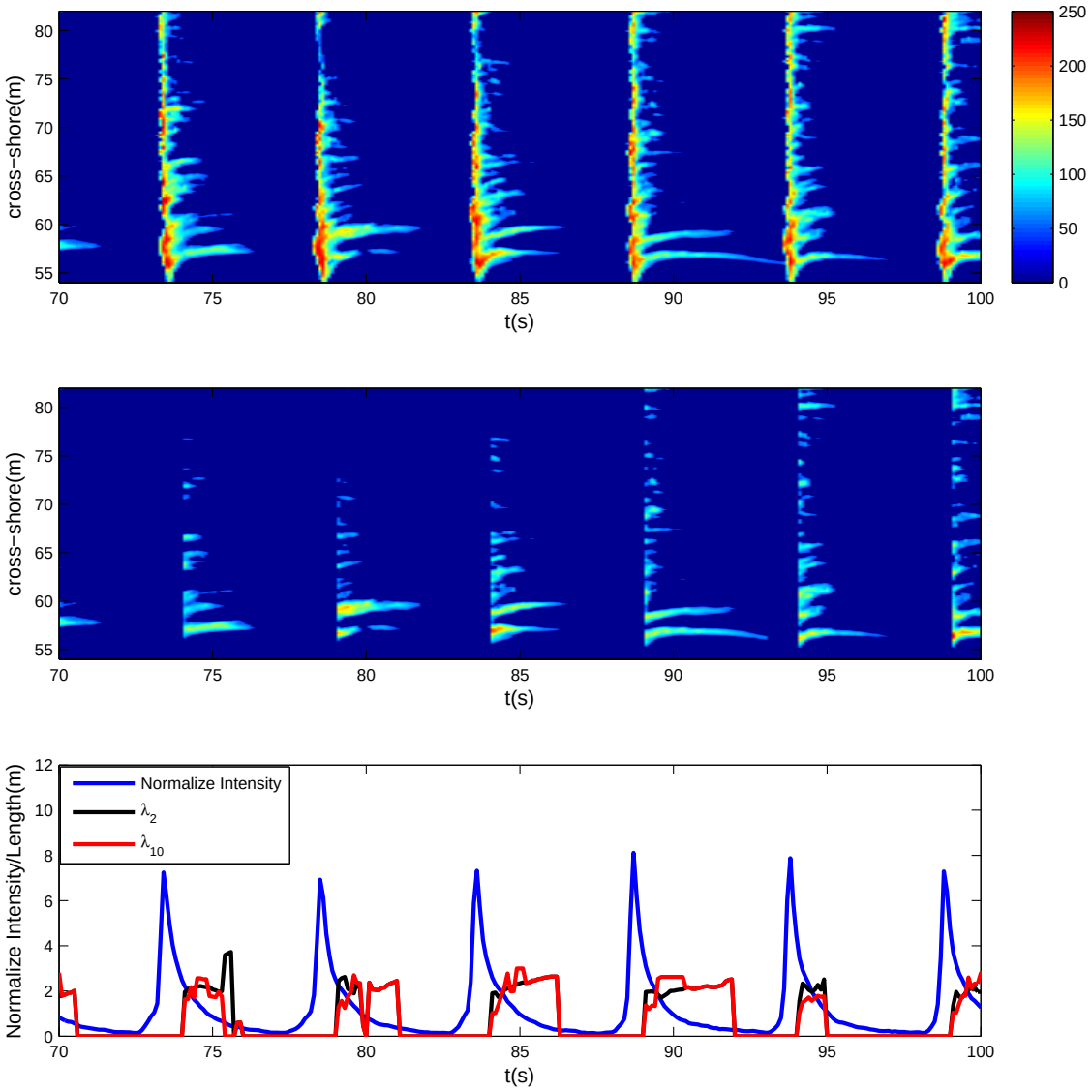

FIGURE 2.4: Time variation of surface foam length scales RUN37

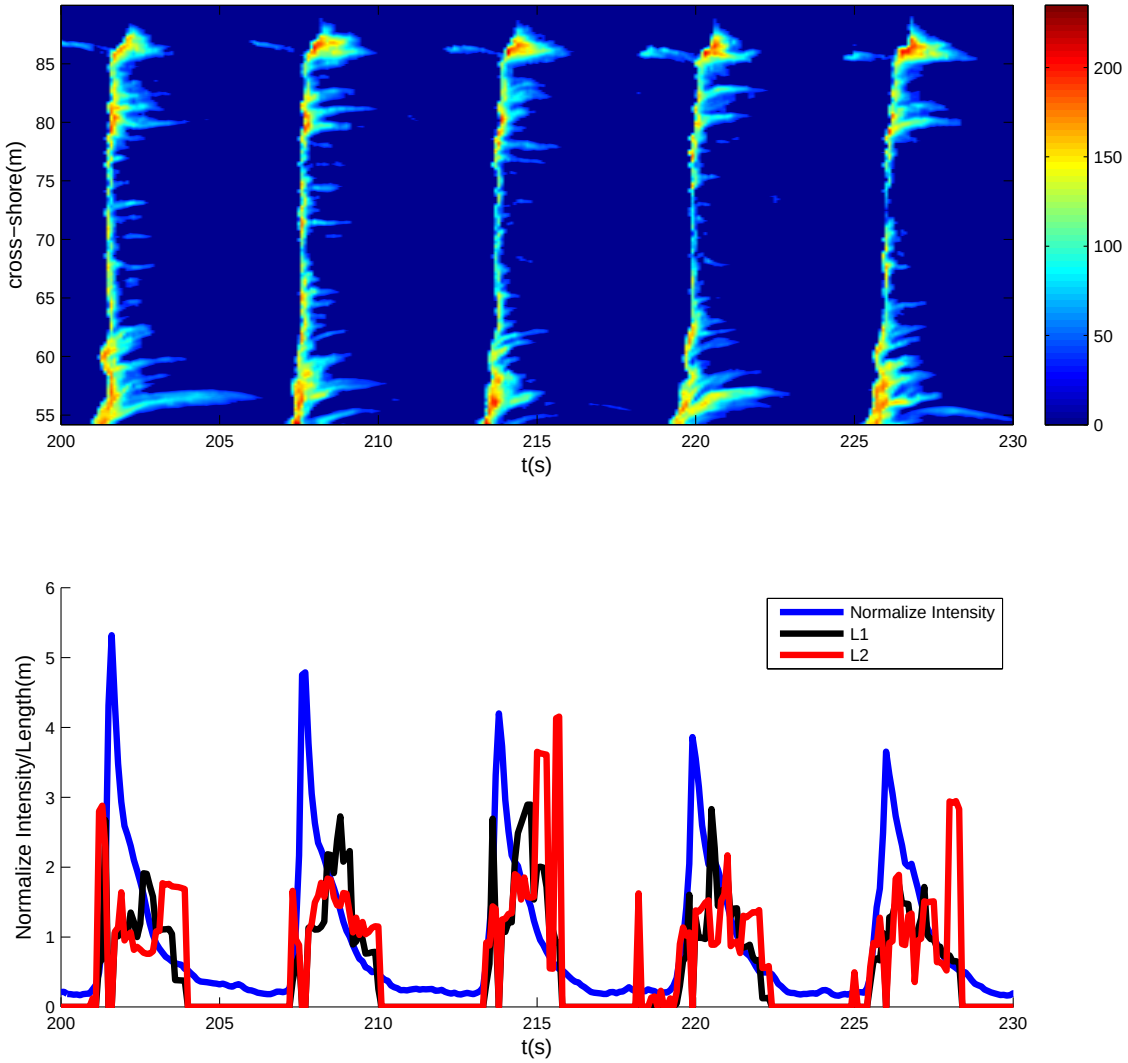

FIGURE 2.5: Time variation of surface foam length scales RUN38

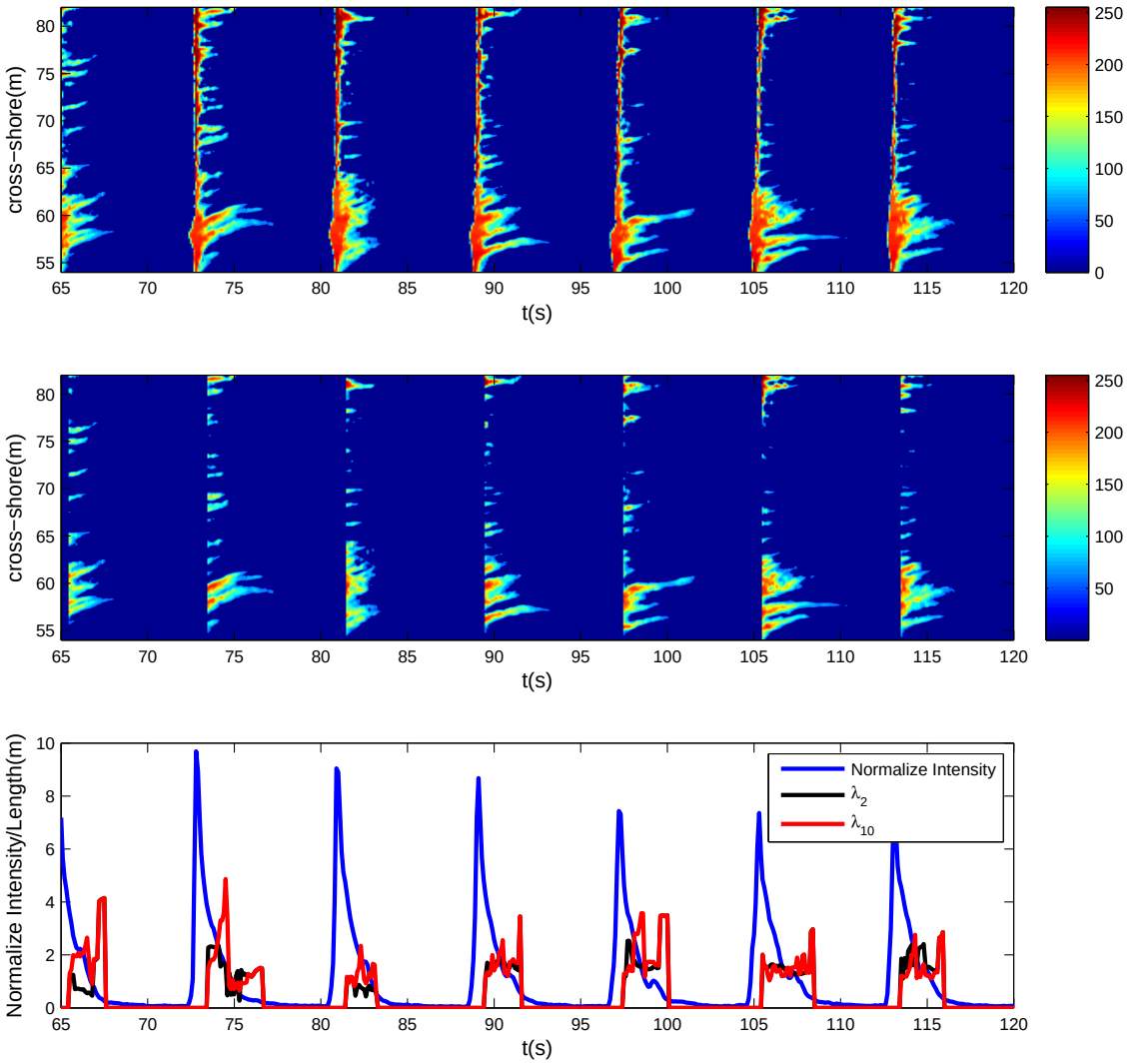

FIGURE 2.6: Time variation of surface foam length scales RUN33

C Wave energy equation

The wave energy equation is described as follow,

$$\frac{\partial E}{\partial t} + \nabla cE + \frac{1}{2} S_{ij}\Big[\frac{\partial u}{\partial x_i} + \frac{\partial u}{\partial x_j}\Big] = D$$
$$\frac{\partial}{\partial t}\Big[\frac{E}{\sigma_r}\Big] + \nabla\Big[\frac{E}{\sigma_r}\Big] = \Big[\frac{D}{\sigma_r}\Big] \tag{C.1}$$

$$\frac{\partial}{\partial t}\Big[\frac{E}{\sigma_r}\Big] + \nabla\Big[\frac{E}{\sigma_r}\Big] = \Big[\frac{D}{\sigma_r}\Big] \tag{C.2}$$

$$\frac{\partial}{\partial t}\Big[\frac{E}{\sigma_r}\Big] = \frac{\sigma_r}{\sigma_r^2}\frac{\partial E}{\partial t} - \frac{E}{\sigma_r^2}\frac{\partial \sigma_r}{\partial t}$$
$$\frac{\partial E}{\partial t} = \sigma_r\Big(\frac{\partial}{\partial t}\Big[\frac{E}{\sigma_r}\Big] + \frac{E}{\sigma_r^2}\frac{\partial \sigma_r}{\partial t}\Big) \tag{C.3}$$

$$\frac{\partial}{\partial x}(U + C_g)\frac{E}{\sigma_r} = (U + C_g)\frac{\partial}{\partial x}\frac{E}{\sigma_r} + \frac{E}{\sigma_r}\frac{\partial}{\partial x}(U + C_g) \tag{C.4}$$

The second term on the RHS is equal to zero;

$$\frac{\partial}{\partial x}(U + C_g)\frac{E}{\sigma_r} = (U + C_g)\Big[\frac{\sigma_r}{\sigma_r^2}\frac{\partial E}{\partial x} - \frac{E}{\sigma_r^2}\frac{\partial \sigma_r}{\partial x}\Big]$$
$$\frac{\partial}{\partial x}(U + C_g)\frac{E}{\sigma_r} = \frac{1}{\sigma_r}\frac{\partial}{\partial x}(U + C_g)E - \frac{E(U + C_g)}{\sigma_r^2}\frac{\partial \sigma_r}{\partial x} \tag{C.5}$$
$$\frac{\partial}{\partial x}(U + C_g)E = \sigma_r\Big[\frac{\partial}{\partial x}(U + C_g)\frac{E}{\sigma_r} + \frac{E(U + C_g)}{\sigma_r^2}\frac{\partial \sigma_r}{\partial x}\Big]$$

Next, substituting **eq.(C.3)** and **eq.(C.9)** into **eq.(C.1)**;

$$\sigma_r\Big[\frac{\partial}{\partial t}\Big[\frac{E}{\sigma_r}\Big] + \frac{E}{\sigma_r^2}\frac{\partial \sigma_r}{\partial t}\Big] + \sigma_r\Big[\frac{\partial}{\partial x}(U + C_g)\frac{E}{\sigma_r} + \frac{E(U + C_g)}{\sigma_r^2}\frac{\partial \sigma_r}{\partial x}\Big] + \frac{1}{2}S_{ij}\Big[\frac{\partial u}{\partial x_i} + \frac{\partial u}{\partial x_j}\Big] = -D$$
$$\frac{\partial}{\partial t}\Big[\frac{E}{\sigma_r}\Big] + \frac{\partial}{\partial x}(U + C_g)\Big[\frac{E}{\sigma_r}\Big] + \frac{1}{\sigma_r}S_{ij}\frac{\partial}{\partial x}U + \frac{E}{\sigma_r^2}\Big[\frac{\partial}{\partial t}\sigma_r + (U + C_g)\frac{\partial}{\partial x}\sigma_r\Big] = \frac{-D}{\sigma_r} \tag{C.6}$$

The third term on LHS is equal to zero as described below and the dispersion relation is described as the following term,

$$\sigma_r^2 = (\omega - ku)^2 \qquad = gktanhkh$$
$$\frac{\partial \sigma_r}{\partial t} = 2(\omega - kU)\Big[\frac{\partial \omega}{\partial t} - k\frac{\partial U}{\partial t} - U\frac{\partial k}{\partial t}\Big] \tag{C.7}$$
$$\frac{\partial \sigma_r}{\partial x} = 2(\omega - kU)\Big[\frac{\partial \omega}{\partial x} - k\frac{\partial U}{\partial x} - U\frac{\partial k}{\partial x}\Big]$$

From the dispersion relation, we can find the time rate of change of the absolute frequency by differentiating **eq.(C.7)** with time and employing the conservation of wave crest principle

$$\begin{aligned}\frac{\partial\omega}{\partial t}+(U+C_g)\frac{\partial\omega}{\partial x}&=k\frac{\partial U}{\partial t}+\frac{\partial\sigma}{\partial h}\frac{\partial h}{\partial t}\\ \frac{\partial k}{\partial t}+(U+C_g)\frac{\partial k}{\partial x}&=-k\frac{\partial U}{\partial x}-\frac{\partial\sigma}{\partial h}\frac{\partial h}{\partial x}\end{aligned} \tag{C.8}$$

$$\begin{aligned}&\frac{\partial}{\partial t}\Big[\frac{E}{\sigma_r}\Big]+\frac{\partial}{\partial x}(U+C_g)\Big[\frac{E}{\sigma_r}\Big]+\frac{1}{\sigma_r}S_{ij}\frac{\partial}{\partial x}U\\ &+\frac{E}{\sigma_r^2}\Big(2(\omega-kU)\Big[\frac{\partial\omega}{\partial t}-k\frac{\partial U}{\partial t}-U\frac{\partial k}{\partial t}\Big]+2(U+C_g)(\omega-kU)\Big[\frac{\partial\omega}{\partial x}-k\frac{\partial U}{\partial x}-U\frac{\partial k}{\partial x}\Big]\Big)=\frac{-D}{\sigma_r}\end{aligned} \tag{C.9}$$

Considering the forth term $\big(\big)$ of LHS and substitute **eq.(C.8)** into the the bracket ;

$$\begin{aligned}\big(\big)&=\Big(\Big[\frac{\partial\omega}{\partial t}-k\frac{\partial U}{\partial t}-U\Big[-(U+C_g)\frac{\partial k}{\partial x}-k\frac{\partial U}{\partial x}-\frac{\partial\sigma}{\partial h}\frac{\partial h}{\partial x}\Big]+(U+C_g)\Big[\frac{\partial\omega}{\partial x}-k\frac{\partial U}{\partial x}-U\frac{\partial k}{\partial x}\Big]\\ &=\frac{\partial\omega}{\partial t}+(U+C_g)\frac{\partial\omega}{\partial x}-k\frac{\partial U}{\partial t}-U\Big[-(U+C_g)\frac{\partial k}{\partial x}-k\frac{\partial U}{\partial x}-\frac{\partial\sigma}{\partial h}\frac{\partial h}{\partial x}\Big]+(U+C_g)\Big[-k\frac{\partial U}{\partial x}-U\frac{\partial k}{\partial x}\Big]\\ &=k\frac{\partial U}{\partial t}+\frac{\partial\sigma}{\partial h}\frac{\partial h}{\partial t}-k\frac{\partial U}{\partial t}-U\Big[-(U+C_g)\frac{\partial k}{\partial x}-k\frac{\partial U}{\partial x}-\frac{\partial\sigma}{\partial h}\frac{\partial h}{\partial x}\Big]+(U+C_g)\Big[-k\frac{\partial U}{\partial x}-U\frac{\partial k}{\partial x}\Big]\Big)\\ &=\frac{\partial\sigma}{\partial h}\frac{\partial h}{\partial t}-kC_g\frac{\partial U}{\partial x}+U\frac{\partial\sigma}{\partial h}\frac{\partial h}{\partial x}\end{aligned}$$

Considering the total water depth $\overline{h}=h+\eta$, and continuity equation

$$\frac{\partial(h+\eta)}{\partial t}+u\frac{\partial(h+\eta)}{\partial x}=0 \tag{C.10}$$

Substituting this term back to **eq.(C.9)**,

$$\frac{\partial}{\partial t}\Big[\frac{E}{\sigma_r}\Big]+\frac{\partial}{\partial x}(U+C_g)\Big[\frac{E}{\sigma_r}\Big]+\frac{1}{\sigma_r}S_{ij}\frac{\partial}{\partial x}U-\frac{2E}{\sigma_r^2}\Big(n\sigma_r\frac{\partial U}{\partial x}\Big)=\frac{-D}{\sigma_r} \tag{C.11}$$

The radiation stress is defined as $S_xx=(2n-0.5)E$,

$$\frac{\partial}{\partial t}\Big[\frac{E}{\sigma_r}\Big]+\frac{\partial}{\partial x}(U+C_g)\Big[\frac{E}{\sigma_r}\Big]+\frac{1}{\sigma_r}(2n-0.5)E\frac{\partial}{\partial x}U-\frac{2E}{\sigma_r}\Big(n\frac{\partial U}{\partial x}\Big)=\frac{-D}{\sigma_r} \tag{C.12}$$

For shallow water ($n = 1/2$),

$$\frac{\partial}{\partial t}\Big[\frac{E}{\sigma_r}\Big] + \frac{\partial}{\partial x}(U + C_g)\Big[\frac{E}{\sigma_r}\Big] = \frac{-D}{\sigma_r} \tag{C.13}$$

D Separation of longwaves over the horizontal bottom

Assuming that the normal incidence of shallow water wave is a linear superposition of incoming (shoreward direction) and outgoing waves (seaward direction). Utilizing the linear wave theory and the velocity potential (ϕ) of normal incidence of shallow water wave, the shallow water wave can be expressed as below,

$$\phi = \frac{g}{\sigma}\Big[Asin(kx - \sigma t + \phi_i) + Bsin(kx + \sigma t + \phi_o)\Big] \tag{D.1}$$

where A and B are the amplitude of the incoming and outgoing wave respectively, ϕ_i and ϕ_o are the relative phases of the incoming and outgoing wave respectively.

$$u = \nabla\phi \tag{D.2}$$

$$\eta = \frac{-1}{g}\frac{\partial\phi}{\partial t} \tag{D.3}$$

where ϕ is the potential velocity, u is current and η is water elevation

Beginning with **eq.(D.2)**;

$$\begin{aligned} u &= \frac{g}{\sigma}\Big[kAsin(kx - \sigma t + \phi_i) + kBsin(kx + \sigma t + \phi_o)\Big] \\ &= \frac{gk}{\sigma}\Big[Asin(kx - \sigma t + \phi_i) + Bsin(kx + \sigma t + \phi_o)\Big] \end{aligned}$$

Let assume $\eta^+ = Asin(kx - \sigma t + \phi_i)$ and $\eta^- = Bsin(kx + \sigma t + \phi_o)$.

Therefore;

$$\begin{aligned} u &= \frac{g}{c}\Big[\eta^+ + \eta^-\Big] \\ \frac{c}{g}u &= \eta^+ + \eta^- \end{aligned} \tag{D.4}$$

Then from **eq.(D.3)**;

$$\begin{aligned} \eta &= \frac{-1}{g}\frac{g}{\sigma}\Big[-A\sigma sin(kx - \sigma t + \phi_i) + B\sigma sin(kx + \sigma t + \phi_o)\Big] \\ &= \Big[Asin(kx - \sigma t + \phi_i) - Bsin(kx + \sigma t + \phi_o)\Big] \\ &= \eta^+ - \eta^- \end{aligned} \tag{D.5}$$

Then, **eq.(D.4)+eq.(D.5)**, so

$$\eta + \frac{c}{g}u = 2\eta^{+}$$
$$\eta^{+} = \frac{\left[\eta + \frac{c}{g}u\right]}{2}$$

Then, **eq.(D.4)-eq.(D.5)**, so

$$\eta - \frac{c}{g}u = 2\eta^{-}$$
$$\eta^{-} = \frac{\left[\eta - \frac{c}{g}u\right]}{2}$$

Therefore, the elevation data is separated into incoming and outgoing component as described below,

$$\eta^{\pm} = \frac{\left[\eta \pm \frac{c}{g}u\right]}{2}$$
$$u^{\pm} = \frac{c\eta^{\pm}}{h}$$